

Fracture and Friction Characterization of Polymer Interfaces

Ivan Quan Vu

Thesis submitted to the faculty of the Virginia Polytechnic Institute and State University
in partial fulfillment of the requirements for the degree of

Master of Science
In
Engineering Mechanics

David A. Dillard, Chair
Christopher B. Williams
Norman E. Dowling

September 14, 2015

Blacksburg, VA

Keywords: Additive manufacturing, PolyJet, print orientation, double cantilever beam,
fracture energy, interface, textile fabric, prepreg, rheometer, tool-ply friction

Fracture and Friction Characterization of Polymer Interfaces

Ivan Quan Vu

ABSTRACT

Understanding the interactions of polymer interfaces is essential to improve polymer-based designs, as the properties of the interface are often different than those of the bulk material. This thesis explores the interfacial interactions of polymer interfaces for two classes of materials, additive manufacturing materials and fiber-reinforced composites.

Additive manufacturing (AM) refers to a number of processes which rely on data generated from computer-aided design (CAD) programs to construct components by adding material in a layer-by-layer fashion. AM continues to generate a substantial amount of interest to produce fully functional products while reducing tooling costs associated with traditional manufacturing techniques such as casting and welding. Recent advancements in the field have led to the production of multi-material printing that has the potential to create products with enhanced mechanical properties and additional functionality. This thesis attempts to characterize the fracture resistance of AM materials produced by the PolyJet process. Test standards established for mode I fracture testing of adhesive joints are adapted to evaluate the fracture resistance and interface between two printed acrylic-based photopolymers. Significant differences in fracture energy and loci of failure between the selected test configurations were observed depending on the print orientation. Failures were nominally seen to occur at the interface, alternating from one adherend interface to another in a random fashion. Results demonstrated a decreasing

trend in fracture energy at slower crack propagation rates, indicating that such dependency is associated with the fracture resistance of the interface. T-peel tests conducted on specimens prepared with both constant and graded interlayers revealed enhanced peel resistance with gradient interlayers, suggesting design opportunities of enhanced fracture toughness by implementing intricate material patterns at the interface of the two photopolymers.

Fiber reinforced composite (FRCs) materials have become increasingly desirable in a number of industrial applications where weight reduction is critical for increased payloads and higher performance. When manufacturing structures from these materials, the presence of friction in the composite forming process is seen to have a major effect on the finished quality. Friction between the plies, or between the composite laminate and forming tool, can be undesirable as shape distortions such as wrinkles can appear and compromise the structural integrity of the finished product. To evaluate these frictional processes, a standard rheometer is used to evaluate tool-ply friction on dry textile fabrics and graphite/epoxy prepregs over a range of temperatures, pressures, and sliding velocities. The results provide some general insights into the frictional response of composite prepregs as a function of the manufacturing environment. The materials tested are shown to have different mechanisms that govern the frictional processes. In particular, the results of friction testing on the prepreg indicate that friction comes from a contribution of both Coulomb and viscous-related mechanisms, the latter which become especially at higher temperatures.

Acknowledgements

I would like to thank my advisor, Dr. David Dillard, for his continued support and guidance throughout my time at Virginia Tech. While he has challenged me to become a better researcher and engineer, he has also presented me opportunities to attend multiple technical conferences and develop connections to expand my network. His financial support during this past year is highly appreciated as it helped alleviate the cost of out-of-state tuition. I appreciate the time and effort he has dedicated in developing my scientific competencies.

I would also like to thank my committee members, Dr. Christopher Williams and Dr. Norman Dowling, for their support throughout the duration of my research projects. I would also like to thank members of the DREAMS Lab, particularly Lindsey Bass, Nicholas Meisel, and Logan Strum. Lindsey has been a great colleague who worked tirelessly to print test specimens for my experiments. Nicholas and Logan were also wonderful assets and teachers who helped broaden my understanding of additive manufacturing. I truly appreciate the collaborative efforts of all the members of the DREAMS Lab.

I want to thank the Department of Biomedical Engineering and Mechanics, the Macromolecules and Interfaces Institute, and the Institute of Critical Technology and Applied Science for providing the facilities and opportunities to perform research at Virginia Tech.

I would like to thank Tammy Jo Hiner, Melissa Nipper, and Lisa Smith for their assistance with administrative and graduate school procedures. I would also like to thank

David Simmons and Darrell Link for their assistance with machine shop orders, and Mac McCord for providing technical advice for my experiments.

I would also like to thank Dr. Jack Lesko and Dr. Nicole Sanderlin for giving me the opportunity to study abroad this past summer at the University of Nottingham. While I was hesitant at first, I can easily say it was one of the best experiences of my life. I want to thank Dr. Davide De Focatiis and his research group at the University of Nottingham for their support and guidance during the duration of my summer research project.

I want to express my gratitude toward my parents, Thu and Trang Vu, as well as my younger brother Jeffrey, whose love and support from Arizona has kept me strong and motivated these past two years. I would like to thank my brother Lucas for being a great roommate and support system during my time here in Virginia.

I would like to thank my fellow lab mates at the Adhesion Mechanics lab: Ahmad Rezaei Mojdehi, Bikramjit Mukharjee, Qian Li, and Shahriar Khandaker, as well as past graduates from our lab, Youliang Guan and Shantanu Ranade. Their friendship and cooperation have been truly valuable to me.

Table of Contents

Acknowledgements	iv
Chapter 1: Introduction	1
Background Information	1
Motivation and Goals	2
Thesis Organization.....	3
Chapter 2: Literature Review	5
Introduction	5
Mode I Fracture	5
Additive Manufacturing	10
Composite Forming Processes	17
Time-Temperature Superposition Principle	24
Conclusions	26
Chapter 3: Fracture and Peel Performance of Additive Manufactured Multi-Material Interfaces	27
Abstract	27
Key Words.....	28
Introduction	28
Experimental Methods.....	31
Materials	31
Specimen Fabrication	32
Build Orientation.....	36
Test Procedure	38
Results and Discussion.....	41
Specimen Comparison.....	41
Print Orientation	45
Rate Dependency.....	53
DCB and TDCB summary.....	57
T-peel specimens and Gradient Architecture	64
Conclusions	66
Acknowledgments	68
Chapter 4: Tool-ply friction of composite prepregs using the rheometer	70
Abstract	70
Keywords.....	70

Introduction	70
Experimental Methods.....	74
Frictional Measurements	74
Specimen Preparation and Materials	76
Results	78
Preliminary Tests – Textile Fabrics.....	78
Prepreg friction.....	85
Discussion	92
Literature Overview	92
Statistical Modeling.....	96
Conclusions	102
Chapter 5: Summary and Conclusions	104
Observations.....	104
Areas of Improvement and Future Work.....	106
Appendix A: Corrected Beam Theory vs. Experimental Compliance Method	108
Appendix B: AM Interface Architecture (Checkered)	110
Appendix C: Rheometer friction results for PTFE.....	113
References	116

Table of Figures

Figure 2.1. DCB test configurations a) with load blocks and b) without load blocks.	7
Figure 2.2. Schematic of TDCB configuration.	9
Figure 2.3. Schematic of stereolithography	13
Figure 2.4. Diagram of matched-die forming	18
Figure 2.5. Diagram of hydroforming.....	20
Figure 2.6. Generalized Stribeck curve with the three regions of lubrication: boundary lubrication (BL), mixed lubrication (ML), and hydrodynamic lubrication (HL).	21
Figure 2.7. Visual representation of a) boundary lubrication (BL), b) mixed lubrication (ML), and c) hydrodynamic lubrication (HL).....	21
Figure 2.8. Generic master curve of relaxation vs. time for polymers	25
Figure 3.1. Illustrations of test configurations and photos of representative specimens during testing: a) aluminum-supported (AL-DCB), b) fully-printed (FP-DCB), c) steel-backed DCB (St-DCB), d) TDCB, and e) T-peel geometries.....	34
Figure 3.2. Illustration of various print orientations used to fabricate specimens. Left: $\bar{x}zy$ orientation for A) AM sandwich strips, B) and C) FP-DCB, and D) TDCB specimens. Middle: fully-printed DCB specimens oriented A) $\bar{x}yz$, B) $\bar{x}zy$, and C) $\bar{y}xz$. Right: Al-DCB specimens oriented A) $\bar{x}yz$, B) $\bar{x}zy$, C) $\bar{y}xz$. Note: $\bar{y}zx$ orientation is not pictured.	38
Figure 3.3. Comparison of a) single and b) gang-printed AM strips.....	38
Figure 3.4. $(C/N)^{1/3}$ vs. crack length a for Al-DCB at 1 mm/min	40
Figure 3.5. G_{Ic} vs. crack length for all DCB configurations in the $\bar{x}zy$ -orientation: blue diamonds (Al-DCB), red squares (FP-DCB), green triangles (St-DCB), and purple circles (TDCB). Note: data points of the Al-DCB are shown for both single and gang-printed specimens as seen in Figure 3.3.....	42
Figure 3.6. Failure surfaces of specimens with corresponding SEM images. Plane of the interlayer is oriented on the xz -plane, with the direction of crack propagation aligned along the x -axis.	43
Figure 3.7. G_{Ic} vs. crack length for the fully-printed DCB configurations based on orientation: red diamonds ($\bar{x}yz$), purple triangles ($\bar{x}zy$), blue circles ($\bar{y}xz$), and green squares ($\bar{y}zx$).	46
Figure 3.8. Failure surfaces and SEM images of fully-printed DCBs printed in the a) $\bar{x}yz$, b) $\bar{x}zy$, c) $\bar{y}xz$, and d) $\bar{y}zx$ orientation.....	49
Figure 3.9. G_{Ic} vs. crack length for the Al-DCB configurations based on orientation: red diamonds ($\bar{x}yz$), purple triangles ($\bar{x}zy$), blue circles ($\bar{y}xz$), and green squares ($\bar{y}zx$). Note: data points in the $\bar{x}zy$ orientation represent “gang-printed” specimens.....	50

Figure 3.10. Failure surfaces of Al-DCBs printed in the a) $\bar{x}yz$, b) $\bar{x}zy$, c) $\bar{y}xz$, d) $\bar{y}zx$ orientation.	52
Figure 3.11. Fracture results for AM sandwich printed in the $\bar{x}yz$ orientation and tested at three crosshead displacement rates: a) G_{Ic} vs. crack length and b) G_{Ic} vs. crack velocity showing clear crack velocity dependence.....	54
Figure 3.12. Fracture surface of Al-DCB printed in the $\bar{x}yz$ orientation at the displacement rate of a) 0.01 mm/min, b) 0.1 mm/min, and c) 1 mm/min	56
Figure 3.13. Summary of average G_{Ic} for DCB specimens according to print orientation.	58
Figure 3.14. Log-log plot of 7-point moving average crack velocity vs. test time for two replicates of specimens printed in the $\bar{x}zy$ orientation.....	60
Figure 3.15. Log-log plot of G_{Ic} vs. crack velocity for all $\bar{x}zy$ orientation specimens tested.	61
Figure 3.16. Log-log plot of crack velocity vs. time for the Al-DCB and FP-DCB specimens printed in four orientations.....	63
Figure 3.17. Log-log plot of G_{Ic} vs. crack velocity for the Al-DCB and FP-DCB specimens printed in four orientations.....	64
Figure 3.18. Load vs. extension curves from T-peel tests.	65
Figure 3.19. Failure surface of T-peel specimens. a) TangoBlack and b) gradient.....	66
Figure 4.1. Anton Parr MCR 302 rheometer.....	74
Figure 4.2. Three annulus geometries. a) 1 mm, b) 2 mm, and c) 4 mm.....	75
Figure 4.3. Dry fabric materials. a) Carr Reinforcement DW0164 plain weave carbon fiber and b) PD-Interglas 92125 UD twill weave glass fiber.....	76
Figure 4.4. Calculated coefficient of friction (μ) against angle of rotation for carbon fiber fabric at a) 1 mm, b) 2 mm, and c) 4 mm annulus (rotational sliding velocity – 100 mrad/sec).....	80
Figure 4.5. Calculated coefficient of friction (μ) against angle of rotation for glass fiber fabric at a) 1 mm, b) 2 mm, and c) 4 mm annulus (rotational sliding velocity – 100 mrad/sec).....	81
Figure 4.6. Calculated coefficient of friction (μ) against contact pressure for carbon fiber fabric at a rotational sliding velocity of 100 mrad/sec. (open symbols – 4 mm annulus, lightly filled symbols – 2 mm annulus, and filled symbols – 1 mm annulus).	82
Figure 4.7. Calculated a) static and b) kinetic COF vs. rotational sliding velocity of carbon fiber with means and standard deviations.	83
Figure 4.8. Calculated coefficient of friction (μ) against contact pressure for glass fiber fabric at a rotational sliding velocity of 100 mrad/sec. (open symbols – 4 mm annulus, lightly filled symbols – 2 mm annulus, and filled symbols – 1 mm annulus).	84
Figure 4.9. Calculated a) static and b) kinetic COF vs. rotational sliding velocity of glass fiber fabric with means and standard deviations.....	85

Figure 4.10. Torque vs. angle of rotation for repeated tests performed at 10 N normal force, 10 mrad/sec, and 20°C.....	86
Figure 4.11. Torque vs. angle of rotation at four different temperatures (angular velocity: 10 mrad/sec, normal compressive force: 5 N.....	87
Figure 4.12. Images of prepreg after completing friction tests at a) 20°C and b) 50°C ...	88
Figure 4.13. Gap size vs. angle of rotation for tests conducted at four different temperatures.....	89
Figure 4.14. Calculated COF (μ) vs. angle of rotation for friction tests conducted at 20° C and 5 N normal compressive force.	90
Figure 4.15. Calculated COF (μ) vs. angle of rotation for friction tests conducted at 50° C and 15 N normal force.....	91
Figure 4.16. a) Torque and b) COF (μ) vs. angle of rotation for friction tests conducted at 50° C and 15 mrad/sec.	92
Figure 4.17. Generalized Stribeck curve divided into three regions. a) boundary lubrication (BL), b) mixed lubrication (ML), and c) hydrodynamic lubrication (HL).....	93
Figure 4.18. Depiction of parallel coupling of Coulomb (C) and viscous (V) friction. ..	95
Figure 4.19. Statistics of first order model of COF as a function of T_K (temperature in Kelvin), V (rotational sliding velocity in mrad/sec), and normal pressure P (in kPa).....	98
Figure 4.20. Statistics of second order model of COF as a function of T_K (temperature in Kelvin), V (rotational sliding velocity in mrad/sec), and normal pressure P (in kPa).....	99
Figure 4.21. Parallel + series model for friction.....	100
Figure 4.22. JMP model and statistics of equation 4.15. Data points are plotted for 20°C (blue), 30°C (green), 40°C (purple), and 50°C (red)	102
Figure A.1. Plot of logarithm of normalized compliance C/N vs. logarithm of crack length a , with slope n	108
Figure A.2. Comparison of fracture energy calculated by CBT and ECM.....	109
Figure B.1. AM test strip with a very course "checkered" patterns of TangoBlack (TB) and TangoBlackShore60 (TB60) printed in the $\bar{x}yz$ orientation. a) side view and b) top view of the strip. Note: figure is not to scale.....	110
Figure B.2. Load vs. extension curves from T-peel tests with addition of checkered pattern.	111
Figure B.3. G_{Ic} vs. crack length of different pattern architectures for the TDCB printed in the $\bar{x}zy$ direction.	112
Figure C.1. Coefficient of friction (COF or μ) against angle of rotation for PTFE using the a) 1 mm, b) 2 mm, and c) 4 mm annulus (sliding velocity – 100 mrad/sec).....	114
Figure C.2. Calculated coefficient of friction (μ) against contact pressure for PTFE at a rotational sliding velocity of 100 mrad/sec. (open symbols – 4 mm annulus, lightly filled symbols – 2 mm annulus, and filled symbols – 1 mm annulus).....	115

List of tables

Table 3.1. Table of material properties for TangoBlackPlus and VeroWhitePlus	32
Table 3.2. Power law coefficients for Al-DCB, FP-DCB, and St-DCB printed in the $\vec{x}zy$ orientation, yielding $G_{Ic} = k \cdot \dot{a}^n$ in J/m^2	62
Table 3.3. Power law constants for the Al-DCB and FP-DCB for four print orientations, yielding $G_{Ic} = k \cdot \dot{a}^n$ in J/m^2	64
Table 3.4. T-peel results	65
Table 4.1. Test parameters for friction testing of textile fabric (for carbon and glass fiber)	77
Table 4.2. Test parameters for friction testing of Cytac MTM49/CF5700	78

Chapter 1: Introduction

Background Information

The characterization of polymer surfaces and interfaces is critical for understanding and improving the performance of polymers in a number of engineering applications including adhesives and thin film coatings. Polymeric materials provide a varied class of interfacial systems consisting of interfaces with air or solids, as well as internal interfaces within the material itself (e.g. the interface between two incompatible homopolymers). Researchers have reported that the structure and physical properties of polymers at interfaces are not the same as those in the corresponding bulk material [1]. In light of this evidence, it becomes clear that much of the mechanical properties of multi-material systems are affected by the interactions at the interfaces, and understanding these interactions may be essential in engineering polymer-based designs. Instruments such as the goniometer, x-ray photoelectron spectroscopy (XPS), and scanning electron microscope (SEM) have often been used in describing the surface energetics and topography of the interface. In terms of mechanical characterization, peel tests, blister tests, and blade cutting tests can be used to characterize the adhesion and shear forces. Despite the tremendous success made in the field of interfacial science, there is still a strong need to control the properties of multi-component polymer systems while expanding the availability of sophisticated methods for studying polymer surfaces and interphases. This thesis presents a study of interface characterization for two types of polymer materials: additive manufacturing (AM) materials and fiber-reinforced composites.

Motivation and Goals

This purpose of this thesis is to broaden the understanding of polymer interfaces by accomplishing two specific goals:

1. Develop test methods to characterize the fracture resistance of 3D printed multi-material interfaces.
2. Characterize tool-ply frictional effects associated with composite forming process.

The first goal of the thesis attempts to characterize the interfacial fracture resistance of two photopolymers printed by AM. In order to study the interactions of the multi-material interface, test standards established for mode I fracture testing of adhesive bonds are adapted to fabricate the materials into known test configurations. Mode I fracture testing was performed to analyze the interfacial fracture resistance of the two photopolymers based on the calculated fracture energies and corresponding loci of failure.

The second goal of the thesis is to characterize tool-ply friction of the composite forming process. Previous research confirms that friction is a major factor that influences the quality of composite structures [2-5]. When sufficient friction is available between the forming tool and prepreg, the composite structure has the tendency to produce shape distortions such as wrinkles or other similar defects which may compromise structural integrity [4, 5]. A chapter in this thesis outlines the use of a rheometer to characterize tool-ply friction at a wider range of sliding speeds that are not available in traditional tribological devices [6]. The frictional mechanisms associated with composite forming are predicted display a wide range of surface contact that varies from Coulomb-

dominated friction to hydrodynamic lubrication, behavior which is typically represented by the Stribeck curve [7].

Thesis Organization

This thesis is divided into five chapters which will be briefly described as follows:

Chapter 1 outlines background information related to this research, as well as provide objectives, goals, and motivation for this study.

Chapter 2 presents an in-depth review of relevant literature concerning key topics which include test methods for mode I, applications of rapid prototyping, composite forming, and TTSP.

Chapter 3 is entitled “Fracture and Peel Performance of 3D Printed Multi-Material Interfaces”. This chapter attempts to characterize the mode I fracture resistance of AM materials printed on the Objet Connex 350 to produce configurations consisting of a soft acrylic layers (TangoBlack) sandwiched between two stiffer acrylic strips (VeroWhite). Several test configurations based on the double cantilever beam (DCB) are developed to evaluate which configuration will accurately determine the fracture resistance of these materials. The results indicate that the interfacial fracture resistance between the two materials is significantly different for each test configuration considered, though all display a degree of rate dependency. While print orientation and interface architecture are shown to also have significant effects on the fracture energies calculated from the test results, loci of failure for all test specimens are shown to have nominally occurred along

the interface. This chapter is written as a journal paper and could be submitted as a publication in the *Rapid Prototyping Journal*.

Chapter 4 is entitled “Measuring tool-ply friction of composite prepregs using a rheometer”. This study aims to use a standard torsional rheometer to characterize tool-ply friction of composites under typical forming process parameters. Textile fabrics and a composite prepreg are tested under a variety of temperature, pressure, and sliding velocities. Under the selected test conditions, the results show that the frictional mechanisms of the prepreg display a combination of Coulomb and hydrodynamic friction, consistent with behavior seen in the mixed lubrication regime of the Stribeck curve.

Chapter 5 provides a summary of results and findings of this research while highlighting potential areas of improvement. This chapter will also suggest future work that may provide further insight into the materials tested.

Finally, the appendix will present some exploratory findings from the fracture and friction tests conducted during an early phase of this research.

Chapter 2: Literature Review

Introduction

Understanding the interaction of polymer interfaces is critical in controlling the performance of the polymer-based designs. In regards to AM, printing multiple materials opens new design possibilities for creating components with tunable locus of failure and resistance to fracture. Several standardized methods have been developed to characterize fracture resistance of adhesive bonds in opening (mode I), in-plane shear (mode II), and out-of-plane shear (mode III) modes, as well as combinations of the aforementioned fracture modes. This thesis explores the idea that the known methods developed for mode I fracture can be applicable to AM materials.

During the manufacturing of fiber reinforced composites, interply friction and friction between the laminate and forming tool are major contributors to laminate deformations during the forming process [8]. Previous research indicates that friction is a dominant factor in forming composites that have significant curvature, where out-of-plane deformations such as wrinkling may occur [9, 10]. To avoid such undesirable geometric changes, it is important to evaluate the effects of friction during composite forming under a variety of temperature, sliding rate, and pressure conditions.

Mode I Fracture

When considering the fracture of monolithic materials, cracks will turn or kink to propagate in a mode I fashion [11, 12]. The criteria describing this phenomenon suggest that fracture proceeds in the direction where the tangential stresses are maximum [13] and grows in the direction that maximizes the energy release rate [14]. Fracture also proceeds in such a way that the mode II stress intensity factor is zero [11, 15]. Due to this

phenomenon, fracture testing of such materials are typically focused on mode I loading. The double cantilever beam (DCB) and the tapered double cantilever beam (TDCB) are two of the most common test configurations used for mode I loading scenarios of adhesive joints [16]. Data obtained from these tests usually consist of force-displacement curves along with crack length observations; these are then used to calculate the critical strain energy release rate (SERR) or fracture energy of the adhesive joint and develop their resistance curves or R-curves. For geometries that exhibit a linear load versus displacement relationship, the strain energy release rate G_I is expressed by the Irwin-Kies relationship [17, 18]:

$$G_I = \frac{P^2}{2B} \cdot \frac{dC}{da} \quad (2.1)$$

where P is the applied load, B is the bond width, C is the compliance and a is the crack length. The compliance C can be determined from the linear relationship between the load and displacement, which may be obtained experimentally from measured data or from various analytical and numerical expressions. Using simple beam theory and assuming identical adherends of constant thickness, as shown in Figure 2.1, the compliance C can be expressed as [17]:

$$C = \frac{\delta}{P} = \frac{2a^3}{3EI} \quad (2.2)$$

where δ is the extension, E is the modulus of the adherends, I is the second moment of area of the adherend cross section, and a is the crack length. By combining equations 2.1 and 2.2, G_I can be expressed as:

$$G_I = \frac{12P^2 a^2}{B^2 E h^3} \quad (2.3)$$

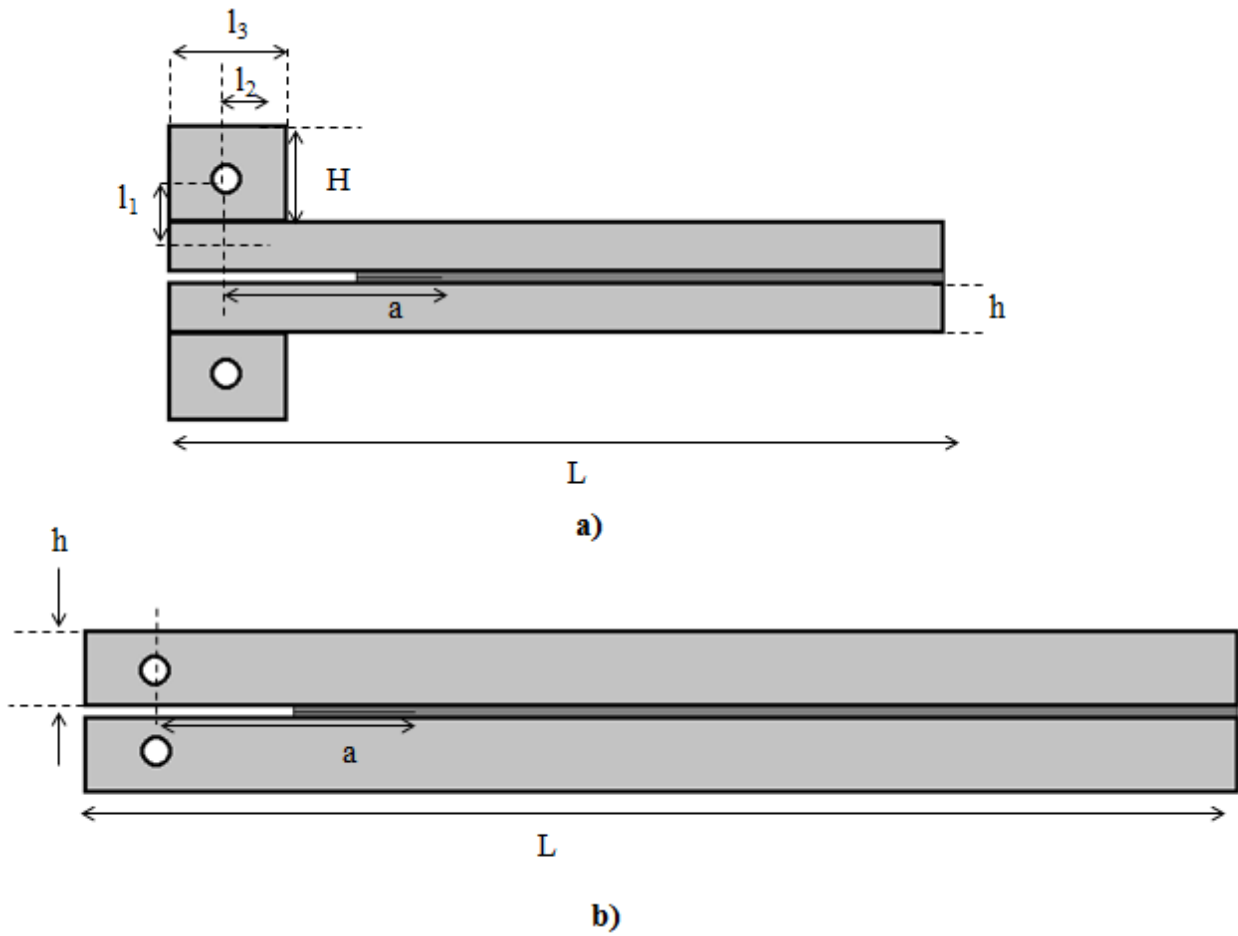


Figure 2.1. DCB test configurations a) with load blocks and b) without load blocks.

Aside from simple beam theory (SBT), corrected beam theory (CBT), advocated by Blackman et al. [19, 20], is an alternate analysis method that accounts for beam root rotation and displacement, system compliance, and differences in crack growth measurement that may vary from one observer to another. In this case, the mode I fracture energy G_I can be calculated by:

$$G_I = \frac{3P\delta}{2B(a + \hat{a}_I)} \cdot \frac{F}{N} \quad (2.4)$$

The length correction factor \hat{a}_l is added to the crack length to account for root rotation and crack tip deflection. The factor \hat{a}_l can be found as the negative intercept of the plot of the compliance $C^{1/3}$ against the crack length a . A load block correction factor N is applied if load blocks are used such as those of Figure 2.1a to account for moments applied at the specimen arms and tilting of the load blocks. Otherwise $N=1$ if load holes drilled directly into the midplane of the substrate are used, such shown in Figure 2.1b. The factor F becomes important to account for large displacements of the substrate beams. These factors can be calculated by:

$$F = 1 - \frac{3}{10} \left(\frac{\delta}{a} \right)^2 - \frac{3}{2} \left(\frac{\delta l_1}{a^2} \right) \quad (2.5)$$

$$N = 1 - \left(\frac{l_2}{a} \right)^3 - \frac{9}{8} \left[1 - \left(\frac{l_2}{a} \right)^2 \right] \frac{\delta l_1}{a^2} - \frac{9}{35} \left(\frac{\delta}{a} \right)^2 \quad (2.6)$$

where l_1 is the distance from the center of the loading pin to the mid-plane of the substrate beam and l_2 is the distance from the loading pin center to the edge of the block [20]. The experimental compliance method (ECM), or Berry's method, is another approach that uses a plot of the logarithm of the normalized compliance C/N against the logarithm of the crack length a . The slope of the plot, n , is used to calculate G_I .

$$G_I = \frac{nP\delta}{2Ba} \cdot \frac{F}{N} \quad (2.7)$$

Tapered double cantilever beam (TDCB) specimens, as their name suggests, are similar to DCB specimens with the exception that the height of the substrates are tapered

over a specified length. An advantage of this type of specimen is their approximately flat load trace which provides ease of analysis [18]. Under a constant displacement rate, the rate of change of compliance with crack length are independent of the value of crack length, resulting in an approximately constant G_I [20]. TDCBs are, however, more expensive to manufacture since more material is required for fabrication and machining costs have traditionally been quite substantial.

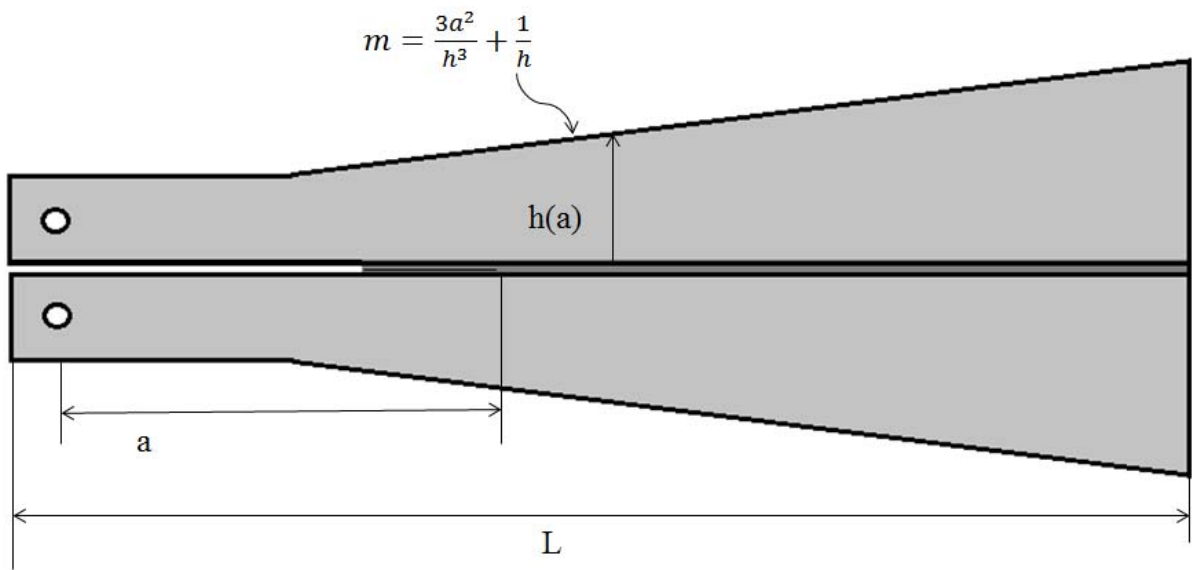


Figure 2.2. Schematic of TDCB configuration.

Similar to DCB analysis methods, equivalent analogs of CBT and ECM [19, 20] can also be applied to the TDCB test configuration. For CBT, corrections are applied to G_I to account for the same factors as DCBs that are not perfectly built-in and are calculated by:

$$G_I = \frac{4P^2}{E_s B^2} \cdot m \cdot \left[1 + 0.43 \left(\frac{3}{m} \right)^{\frac{1}{3}} \cdot a^{\frac{-1}{3}} \right] \quad (2.8)$$

The height of the specimen h is varied by contouring the substrate beam so that the specimen geometry factor m is constant. The calculation of G_I using ECM is performed using the Irwin-Kies relationship as shown in equation 2.1. The value of dC/da is given by the slope of the linear fit of the compliance vs. the crack length.

The standard established by Blackman and co-authors [19, 20] suggest a constant crosshead displacement rate be applied during testing. Other test standards, such as ASTM D-3433 [21], have been used to evaluate the mode I fracture energies. This method involves displacing the specimen up to the point of crack propagation, and stopping the displacement until the load plateaus. This process is repeated to obtain multiple values of G_{Ic} . Tests performed in this fashion offer insights into both crack initiation and arrest properties for an adhesive system [21]. A similar procedure suggested by Blackman and co-authors suggest unloading after reaching the load plateau, which would allow one to observe effects of plasticity and yielding of the adherends [22].

Additive Manufacturing

Additive manufacturing (AM) has become a focal point of research for improving the efficiency of product development and manufacturing. The American automotive industry is credited as being the primary driver for the development of processes that could produce physical components efficiently without the need for tooling [23]. Such demand was difficult to achieve primarily due to the lack of computational capabilities in the early 1980s. The emergence of 3D computer aided design (CAD) programs eventually lead to the development of AM. The first commercial systems appeared in the US in the late 1980s and though other countries such as Japan, Germany, Russia, and

China began their own developments, it is the American suppliers who first established the market for AM [23]. Traditional manufacturing processes, such as milling, sanding, and grinding, are characterized as subtractive methods used to cut material away to produce the final product. In contrast, AM processes are additive in that components are built-up in layers until a final desired geometry is obtained. A variety of materials such as polymers, waxes, and powders have been used for the development of products through AM, though metals such as titanium, sterling silver and stainless steel have also been used for products [24]. Processing polymeric materials for AM is often challenging as it requires the delicate selection of a polymeric powder and binder combination to provide optimal rheological properties during printing [25]. While the materials and layer build can vary significantly between different AM processes, the initial design development is the same. The starting point of every AM process is generating a 3D CAD model or geometry that meets the design requirements for a particular application. The geometry is converted into a stereolithography (STL) file where the model is sliced into a compilation of thin cross-sections. The STL file is used to physically construct the 3D model into a final prototype through the layer-by-layer deposition process as discussed earlier. The mechanical properties of the finished prototype are ultimately determined by the materials and process used for fabrication. The most popular AM processes are stereolithography, selective laser sintering, fused deposition modeling, 3D printing, and polymer jetting.

Stereolithography is one of the oldest methods used for AM, beginning in the 1980s, and still remains a standard technique. A vat of liquid photopolymer contains a platform where the part is built. The platform is adjusted to a level just below the surface

of the liquid polymer. A layer or cross-section of the part is created when the polymer is cured and traced out by a laser [23, 26]. The platform falls by a user-defined distance to recoat the layer with liquid polymer and rises back up such that the top of the solidified layer is leveled with the surface. A wiper blade spreads the liquid polymer over the part in preparation of building the next layer. The platform is lowered to a distance of one layer and the process is repeated until layers are fully assembled. Once the part is completed, it is removed from the vat and placed in a UV oven to be postcured [23, 27]. Prototypes with complex geometries can accurately be created using this process. However, the parts can warp and deform easily under high stresses, especially if acrylate resins are used [23, 26]. Selective laser sintering is similar to stereolithography except a layer of powdered material, such as nylon, wax, metals, sand, and polycarbonate, is deposited onto the platform and the laser fuses (or sinters) the powder material together after exposure. New layers are created by depositing more powder and repeating the same process. Prototypes developed by this process have poor surface finishes and are often porous [23].

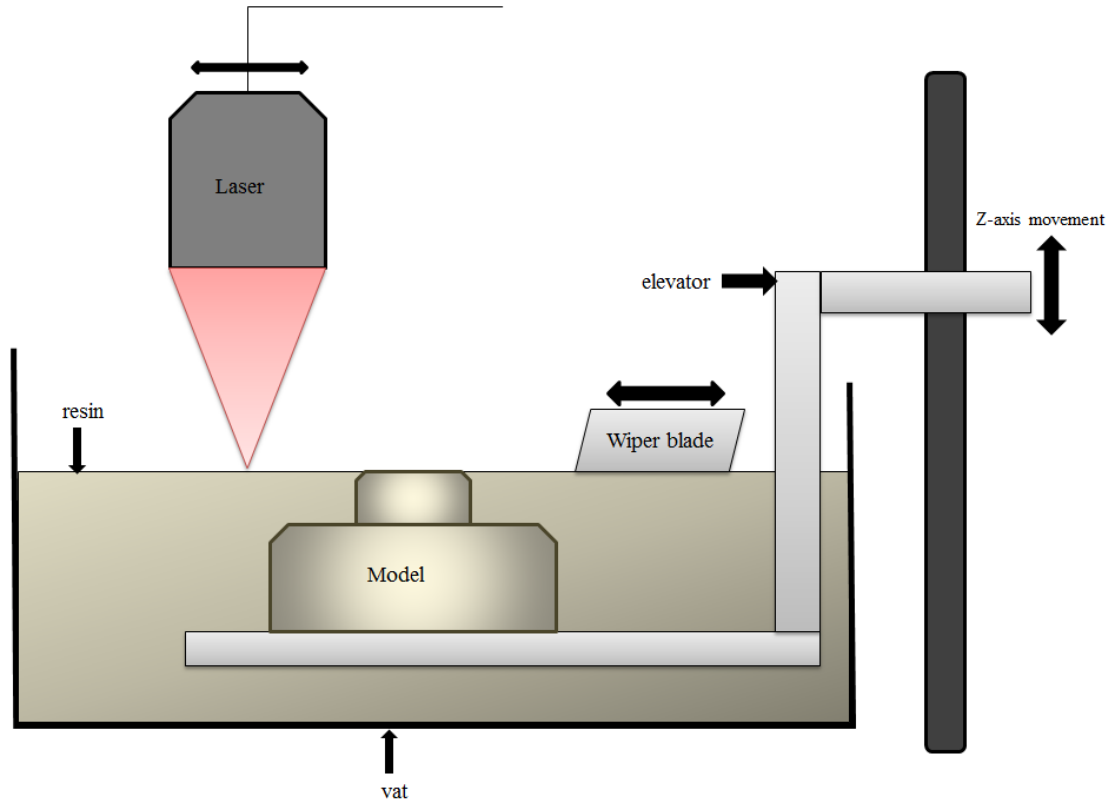


Figure 2.3. Schematic of stereolithography

Fused deposition modeling was another method that was often used for concept modelling, as parts produced by this method were considered non-functional due to their poor strength and surface finishes [23]. Fabrication starts when a spool of thermoplastic filament feeds into a heated extrusion head to be melted into a liquid state up to 0.5°C above the melting point [26, 27]. This allows the filament to solidify about 0.1 seconds after extrusion and cold weld onto previously build layers [27]. The liquid filament is sent to a nozzle that deposits the threaded filament onto a platform, moving across the x-y plane. Parts can be made from a variety of materials such as investment casting wax, acrylonitrile butadiene styrene (ABS), and elastomers, but poor tensile strength becomes apparent when the finished parts are loaded in the direction of the layer build due to the weak adhesion of layers caused by defects [27, 28]. Perez et. al confirmed this result

with ABS-based materials fabricated by fused deposition modeling after tensile testing, and indicated that failure occurred at the inter-layer boundaries between printed layers [29]. Ahn et al. observed the effect of both air gap and raster orientation on the tensile strength of ABS materials created by fused deposition modeling. The air gap is defined as the space between threads of FDM material and the raster angle is the direction of the fibers relative to the loading of the part [30]. It was confirmed that a negative air gap (when threads are touching and fused together) leads to an increase in both stiffness and strength [30]. Axial loading along the fibers yields the highest tensile strength values [28, 30].

3-D printing (3DP) is one of the latest modelling techniques first developed by the Massachusetts Institute of Technology [23]. Products developed by this process are also used for proof of concept modelling, but if properly impregnated, products can also be used as sacrificial master patterns in investment casting processes [23]. The materials employed by 3-D printing are typically metal or ceramic powders, or metal–ceramic composites with colloidal silica or polymeric binders [27]. A typical set-up of 3-D printing consists of a feed chamber that contains a powder on top of a feed piston that is free to move up or down. The powder is spread onto an adjoining piston and build chamber by a roller. Inkjet printing heads apply binder material to sinter the powder spread to create a cross section of the desired model [23, 26]. Once a layer is completed, the build chamber piston lowers at a user-defined distance and repeats the process for a new layer until the CAD model is fully created. The completed part is subjected to a final firing at 900°C for 2 hours in order to set and sinter the binder powder combination [27]. Additional strength can be gained by immersing the completed part in the binder and

refiring under the same conditions described above [27]. While this process requires shorter build times and inexpensive materials, models are also fragile and require infiltration after printing [23]. 3-D printed prototypes have higher surface roughness due to their initial powdery state.

Polymer jetting technology (PolyJet) is another AM method similar to stereolithography and selective laser sintering. Liquid photopolymer is applied in a layer-by-layer process via inkjet printing onto an internal tray. UV bulbs attached to the printhead emits UV light to cure the layer while printing [31]. The internal tray or print cartridge moves vertically in precise steps to continue adding layers and repeat the process until the final product is made. Kim et al. conducted a benchmark study comparing the mechanical properties of materials in several AM processes. With the exception of stereolithography, all processes, including PolyJet, were shown to demonstrate lower tensile strength when tensile load was applied in the build direction [32]. Specifically, the tensile strength of PolyJet materials was 53% lower when the load is applied in the build direction compared to load being applied orthogonal to the build direction [32]. When conducting tensile tests over a range of temperatures, PolyJet materials from the Objet's Eden500V were shown to be the most temperature sensitive, resulting in a large decline of tensile strength when the temperature increased from -10°C to 60°C [32]. Keszy et. al. characterized the tensile properties of these materials using tensile test bars made of Objet's FullCure720 resin material, printed in three orientations using the Objet Eden 260 printer [31]. They demonstrated that the differing strength originates from an uneven distribution of UV exposure between the different orientations [31]. The edges of created layers reportedly absorb more light than the layer surface,

which may cause these regions to become denser and harder [31]. This results in the edges acting as additional reinforcement that increase the tensile strength of the bars depending on the direction of the applied load. Cazon et al. also observed the tensile properties of Objet's FullCure 720 printed from the Objet Eden 330 printer at six different orientations. They reported that while specimens loaded in the print direction had the lowest fracture stress and elongation at break, the elastic modulus and ultimate tensile strength were seen to be higher compared to other orientations [33]. Pilipovic et al. performed experimental analysis on specimens made by 3DP and by the PolyJet procedure. They reported that the 3DP materials often exceed tolerance limits for production due to their high surface roughness, whereas the PolyJet materials maintain low surface roughness. Higher tensile and flexural properties of PolyJet materials were observed when compared to 3D printed materials [34]. Barclift et al. performed a design of experiment (DOE) on Objet's Fullcure 830 VeroWhite photopolymer materials printed from the Objet Connex 350, where the part orientation and spacing between multiple printed parts across the printing path were observed to affect the tensile properties [35]. While part orientation showed mechanical properties were not statistically different, the highest values of tensile strength and modulus were seen when parts were printed closer together. When printing multiple parts that span multiple print paths, the UV irradiation over-cures localized areas that are adjacent to the current printing path, which imparts higher tensile properties [35]. Moore performed fatigue characterization on the Objet's VeroWhite and TangoBlack, also printed from the Objet Connex 350. His work demonstrated that the multi-material interface between the VeroWhite and TangoBlack provided higher number of cycles to failure compared to their pure counterparts. Surface

finishes were seen to increase the cycles to failures as well [36]. The TangoBlack material is seen to produce voids as a consequence of the printing process, where the voids were found at the boundary between layers.

Composite Forming Processes

The manufacturing of laminated fiber reinforced composites requires a combination of manual and automated processes to form the material into the desired geometry. As composite structures become increasingly large and complex, the processes involved in forming these structures becomes complicated and time-consuming and the forming quality becomes less repeatable [2]. A variety of composite forming processes have been available for manufacturing composites structures and each forming method is unique in terms of cost and quality of the finished structure. The major processing methods currently being used in forming are matched-die press forming, diaphragm forming, hydroforming, autoclave/ vacuum forming, and rubber pad press forming [37].

Matched-die forming is among the most widely used forming system known for its quick processing time. The dies used are generally made of metal and can be internally heated or cooled. The preform sheet or workpiece is placed in the press between two matching dies to form the part as shown in Figure 2.4 [37, 38]. A significant disadvantage is that structures made by this process experience local thickness changes due to thickness mismatch between the part and die cavity. This mismatch arises from the fact that continuous fiber reinforced composites are effectively inextensible in the direction of the reinforcement, which limits the range of in-plane deformation that the material can experience [38]. Die conformity can be achieved by flow processes such as intra- and interply slip, but this leads to not only local changes in fiber orientation

between adjacent plies, but also causes thickness variations within the laminate [38]. The tooling cost associated with matched-die press forming is high because of the requirement of close dimensional tolerance between the two die halves [37].

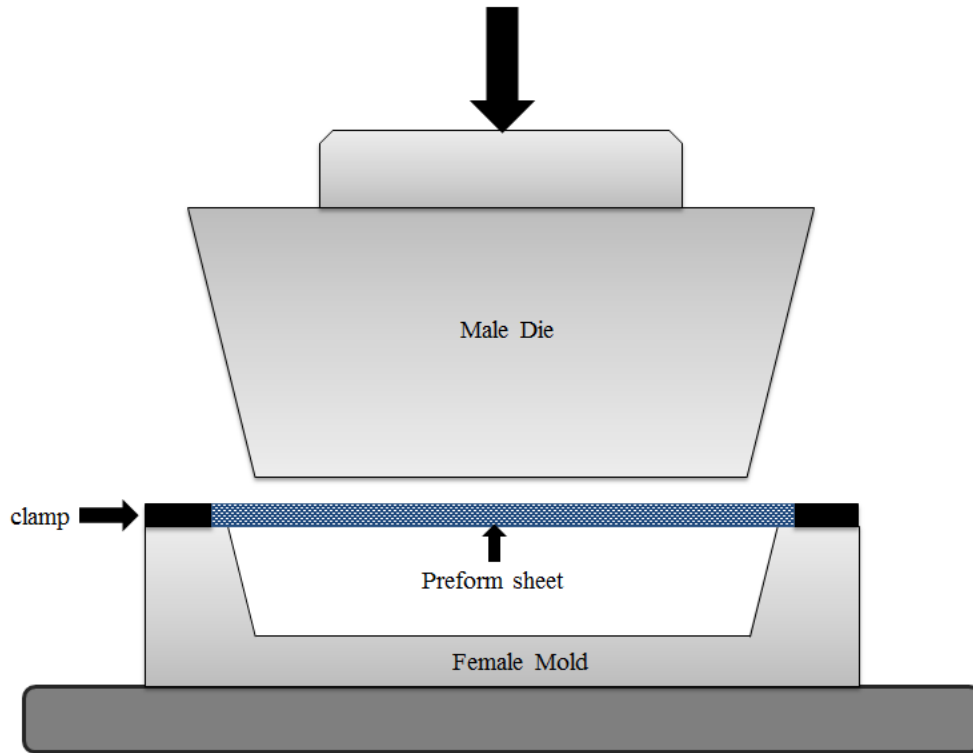


Figure 2.4. Diagram of matched-die forming

Diaphragm forming is a promising alternative to matched-die press as this method involves forming the sheet or workpiece with disposable plastically deformable diaphragms. These diaphragms are clamped onto the tool halves and heated with the sheet, being deformed by vacuum pressure [37, 39]. The sheet itself is not clamped and is free to slide within the diaphragms. The sliding action creates tensile stresses from interfacial shear stresses that reduce wrinkling [37]. A major limitation of this process is that the diaphragm itself may deform at a finite temperature range which restricts the processing temperature of the sheets. It is also documented that cycle times are long due to heating and cooling of the pressure chambers [37, 39].

Hydroforming is similar to diaphragm forming in that a fluid medium, placed behind the diaphragm, is used to deform the sheet. This process has been used extensively for forming sheet metal, capable of applying pressure up to 68.9 MPa [37]. This process involves the sheet being clamped onto the female mold and the fluid chamber with a deformable diaphragm is located on the top of the sheet. When the fluid is pressurized, the diaphragm exerts the force necessary to deform the sheet onto the mold to create the desired geometry [37, 40]. The high pressure associated with this process allows undercuts to be formed onto the sheet, allowing more conformity to the mold. Since the rubber used in these systems are only suitable in lower temperatures, multiple rubber sheets are placed over the workpiece to prevent diaphragm rupture due to high temperatures or sharp points on tools [37]. This also slows the rate of wear of the mold in comparison to other methods. Structures created by autoclaves are similar to hydroforming and diaphragm forming and are created in a chamber of pressurized gas. The composite structure is formed from a pressure differential between the mold cavity and the autoclave chamber. Vacuum forming is performed when the pressure in the autoclave is atmospheric and the evacuated mold is under vacuum [37]. However, cycle times for processing are also large due to large thermal inertia related with heating and cooling the chamber [37]. The pressure levels used in autoclave forming are known to be low and are thus impractical as more pressure is needed for deformation and consolidation at reasonable time scales [37].

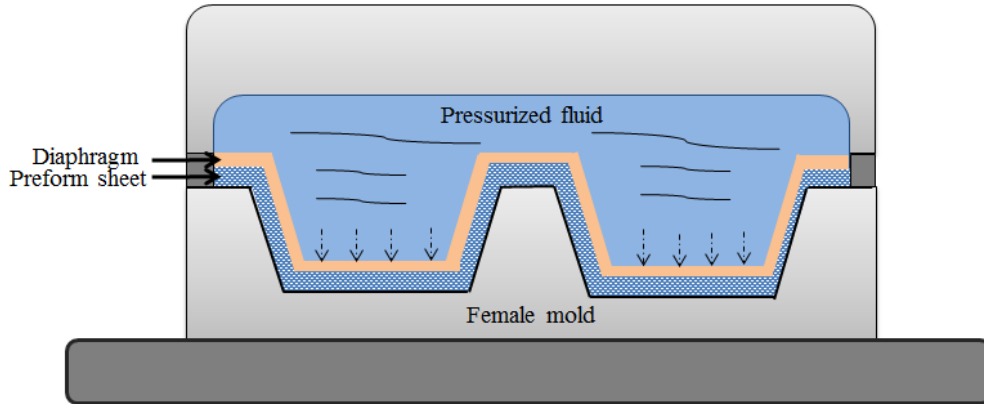


Figure 2.5. Diagram of hydroforming

Rubber pad press forming consists of two dies, where the press punch consist of a rubber pad and the die or mold is made of metal. As the punch advances, the rubber acts like a hydraulic fluid that exerts nearly equal pressure on the sheet surface as it is consolidated onto the mold, reducing any thickness variations within the formed structure [39, 41]. This process is attractive in that both the punch and dies can be interchanged without alignment or mismatch. The surface of the metal is also protected from scratches and wear when in contact from the rubber press [41]. A major disadvantage is the restricted temperature range at which this process can be performed. The compliant material used for the rubber pad, such as silicone, are often limited to 230-290°C in air [37].

In light of the review of forming methods, a common phenomenon that influences the quality of the finished part is the friction between tool and laminate, or interply friction between adjacent plies. Friction during the forming process is often undesirable as it causes residual stresses and shape distortions such as wrinkling and cracking of the laminate [4, 37, 42]. Similar to the design of journal bearings, friction and lubrication theory is utilized to study the effects of friction in composite forming, as the resin matrix,

at certain temperatures and strain rates, can act like a lubricant between the relative motion between plies. The Stribeck curve provides an overall view of friction variation in the entire range of lubrication and is illustrated schematically in Figure 2.6.

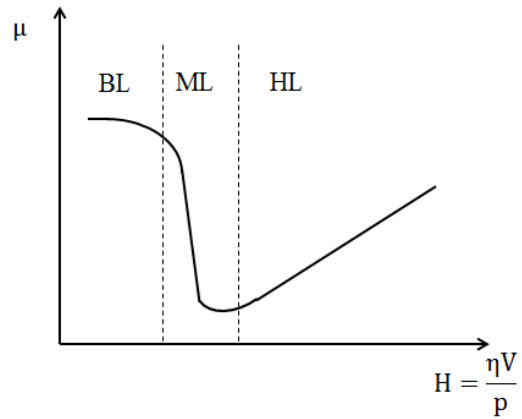


Figure 2.6. Generalized Stribeck curve with the three regions of lubrication: boundary lubrication (BL), mixed lubrication (ML), and hydrodynamic lubrication (HL).

The Stribeck Curve provides a graphical representation of the friction coefficient μ as a function of the Hersey number H , a nondimensional quantity that is dependent on the dynamic viscosity of the fluid η , velocity V , and the pressure p . The curve is categorized into three regions based on the level of contact between the plies or surfaces of interest.

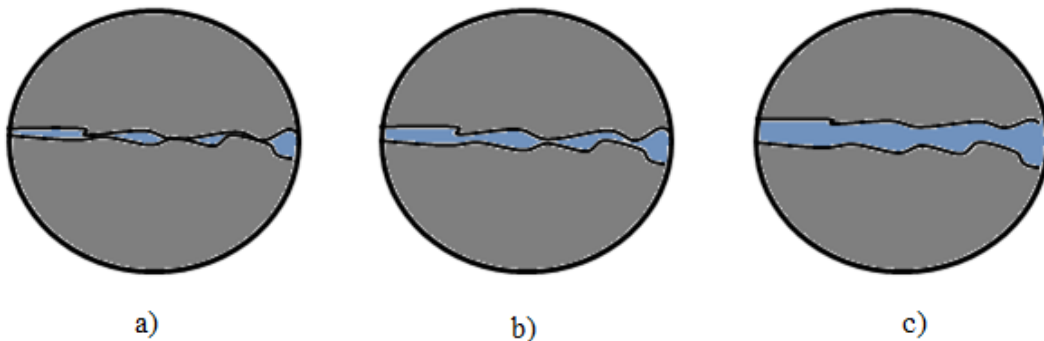


Figure 2.7. Visual representation of a) boundary lubrication (BL), b) mixed lubrication (ML), and c) hydrodynamic lubrication (HL)

Boundary lubrication (BL) is primarily governed by Coulomb friction, which is initiated by contact between surface asperities [4, 7]. The fluid film or lubrication layer thickness in these contact regions is negligible and has an insignificant effect on friction. As the film thickness increases, the mixed lubrication (ML) region is reached, where the coefficient of friction will eventually reach a minimum and the contacting surfaces are partially separated by the fluid film. As the fluid becomes thicker and more viscous, the coefficient of friction will eventually increase, primarily due to viscous shear and drag that occurs between the contacting surface [7]. At the hydrodynamic lubrication (HL) region, the fluid film has sufficient thickness and viscosity to support the loads between the contacting interface at high velocities by hydrodynamic pressure [4, 7, 43].

Friction during composite manufacturing has been well-documented, though remains a topic in need of considerable research. A number of test configurations have been developed by a number of researchers to characterize both tool-ply and interply friction. Martin et al. developed an apparatus that consists of two internally heated steel platens held together by screw-spring pins and pressurized using a pneumatic cylinder [44]. A prepreg sample would be loaded in a pull-plate in between the fixture and pulled at a constant displacement rate to mimic tool-ply friction. In addition to tool-ply friction, interply friction was also simulated by using an additional prepreg that is looped around the spar attached to the lower screw pins. This configuration allowed the manipulation of temperature, pressure, and sliding rate to determine their effects on friction. Interply friction was demonstrated to be dependent on both resin viscosity and distribution, as systems with less resin showed higher frictional resistance due to mechanical interlocking of the fibers as the resin softened at higher temperatures [44]. Ersoy et al. [45] and Sun et

al. [2] would later adopt this configuration on their studies of interply friction. While Ersoy et al. [45] showed similar results to Martin et al. [44] in their studies on unidirectional (UD) carbon/epoxy prepregs, they also demonstrated an increase of friction at higher temperatures up to the vitrification point, where the resin begins to gel and become sufficiently stiff to bear the applied forces [45, 46]. Sun et al. would use this instrument on UD carbon fiber/epoxy prepreg systems formed by hot diaphragm forming, observing that decreasing the temperature and increasing the pulling rate led to Coulomb friction -dominant behavior, resulting in subsequent wrinkling in the laminate at higher coefficients of friction [2]. Larberg et al. observed higher frictional resistance in UD carbon fiber/epoxy prepregs when they were additionally toughened with thermoplastic particles [4].

In regards to tool-ply friction, Ersoy et al. noted that the lay-up of the laminate had a significant effect on friction, indicating that the presence of 90° plies increased the interfacial shear stress and reduced stress relaxation due to increased mechanical interlocking of the fibers [45]. Thijs et al. extensively studied tool-ply friction in thermoplastic composite forming, where they developed a mesoscopic model based on the Reynolds' equation [5, 8]. Their model utilizes the rheological properties of the matrix material and the geometry of the fabric weave as input parameters, but they noted that the model was only valid within the HL regime [5, 8]. The model demonstrated the effects of tool-ply friction of a woven glass fiber/polypropylene composite, noting that the coefficient of friction increases when the velocity increases, but decreases when the temperature and normal pressure increase [5, 8].

Time-Temperature Superposition Principle

When characterizing the behavior of polymers, the time temperature superposition principle (TTSP) is a very useful concept that can be utilized to describe polymer viscoelasticity over a wide range of temperatures and time scales. This technique demonstrates that a number of mechanical tests of short duration can be performed at multiple temperatures to predict a mechanical property of interest as a function of time and can span over many decades in time [47]. TTSP is based on the fact that time and temperature variation of the viscoelastic properties (e.g. moduli, compliances, or viscosities) of a polymer are related and with regards with the relaxation modulus, this equivalency can be expressed as [47]:

$$E(t', T_0) = E(t = a_T t', T) \quad (2.9)$$

As shown above, the relaxation modulus $E(t, T)$ measured at a time t and temperature T can be horizontally shifted onto a reference temperature T_0 after modifying the timescale by a multiplicative shift factor, a_T [47]. It should be noted that equation 2.9 ignores vertical shifting onto the reference temperature, T_0 . The shift factor is the ratio of the new relaxation time to the reference relaxation time, or $a_T = \frac{\tau}{\tau_0}$. The relaxation modulus is collected over time t at various temperatures, where the individual data sets can be shifted onto a reference temperature to cover time scales that are much broader than the range tested [47]. Shifting of the data sets results in a master curve of the relaxation modulus as a function of reduced time (t). A general schematic of relaxation modulus master curve as a function of time is shown in Figure 2.8, where the polymer displays the full spectrum of viscoelastic behavior that range from glassy to rubbery to liquid flow.

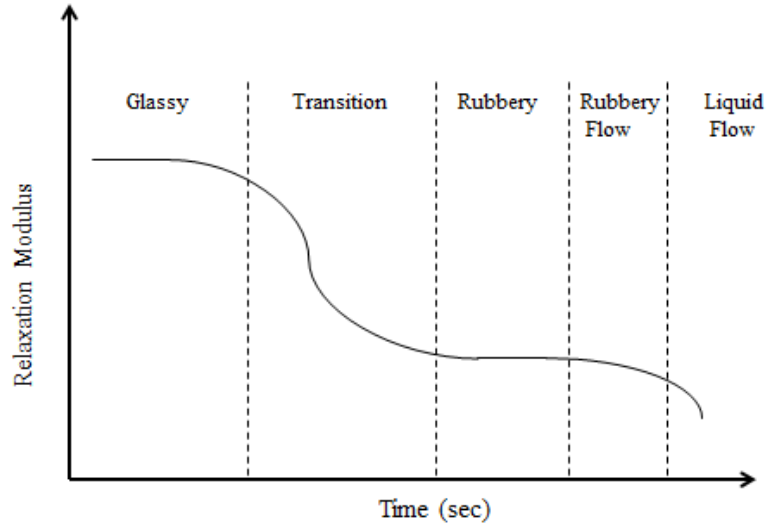


Figure 2.8. Generic master curve of relaxation vs. time for polymers

The shift factors of TTSP may be found experimentally or, by using accepted expressions, such as the Williams-Landel-Ferry (WLF) equation within the range of $T_g \leq T \leq (T_g + 100^\circ\text{C})$, where T_g is the glass transition temperature:

$$\log_{10} a_T = \frac{-C_1(T - T_0)}{C_2 + (T - T_0)} \quad (2.10)$$

The constants C_1 and C_2 are dependent on the material and the selected reference temperature T_0 [47]. A number of methods are available to form mathematical expressions approximating the resulting master curve such as the generalized Maxwell model or Prony series representation, but these fits are typically only valid within the bounds of the known experimental data [47]. While the TTSP is shown to be valid for a variety of viscoelastic constitutive properties such as relaxation spectra, creep compliance spectra, storage modulus and loss modulus, it has also been used to successfully characterize other mechanical properties such as the peel strength of composite prepregs [48] and the fracture energy of adhesive joints [49, 50].

Conclusions

The overview of AM demonstrates that many processes can be used to create a desired product with customizable mechanical properties and functionality for a particular application. While previous literature has established the mechanical properties of AM materials in tension, the fracture characteristics of such materials in mode I remains largely unknown. The research outlined in the next chapter attempts to address this issue by replicating test geometries based on the DCB, a fracture test used to characterize the fracture behavior of adhesive joints. It is important to provide a summary of related test methods and provide insight to optimize the fracture toughness of AM materials. The DCB and TDCB have achieved international standardization for mode I fracture. It is seen that much of the relevant literature has utilized these techniques to develop an understanding of fracture behavior for metallic, composite, and wood adhesive joints, but this current research will attempt to adapt these standards in application to AM multi-materials.

Tool-ply and interply friction during composite forming is a major complication that has tendencies to compromise the finish quality and structural integrity of composite structures. While a number of different processes can be used in composite forming, typical process parameters such as temperature, pressure and shear rate are seen to have a complex interaction with friction. In this research, a standard rheometer based on the design from Kavehpour et al. is used to characterize tool-ply friction over a wider range of sliding velocities than is typically possible with traditional tribological devices such as pin-and-disk systems [6]. Dry textile fabrics and composite prepregs are tested, where different frictional mechanisms govern each material during testing.

Chapter 3: Fracture and Peel Performance of Additive Manufactured Multi-Material Interfaces

This chapter is written as a manuscript and could be published in the *Rapid Prototyping Journal* with the title “Characterization of Multi-Material Interfaces in PolyJet Additive Manufacturing”.

Abstract

Relatively few engineering devices and structures are monolithic, as combinations of materials are often needed to obtain the necessary functionality, performance, weight, and cost requirements. Progress in additive manufacturing now allows multiple materials and even blends of materials to be produced in a single manufacturing process, opening new opportunities for expeditiously achieving functional and performance targets. Just as interactions at interfaces have long been of interest in the area of adhesive bonding, similar issues need to be addressed for printed composite materials. In this study, a Stratasys PolyJet system was used to produce fracture specimens consisting of a soft acrylic layers (TangoBlackPlus) sandwiched between two stiffer acrylic strips (VeroWhitePlus). Several test specimen configurations based on the double cantilever beam method, a common experimental approach to characterize the fracture behavior of adhesive bonds, were fabricated and evaluated to measure the fracture resistance of the assembled layers. Failures nominally occurred at the interface between the two types of materials. This study demonstrates that the fracture energies are somewhat dependent on the test configuration used, and all display increased fracture energy at higher crack propagation rates, indicative of the rate dependent nature of the interface and materials involved. Nonetheless, substantial differences in the fracture energy and locus of failure

were observed as a function of the print direction and interface architecture on the resulting fracture energies. These studies suggest the opportunities for designing printed interfaces with improved performance and durability for multi-material additive manufacturing products.

Key Words

Multi-material, PolyJet, print orientation, double cantilever beam (DCB), interface, crack propagation, fracture energy

Introduction

Offering a versatile alternative to traditional manufacturing techniques, additive manufacturing (AM) embraces the concept of reducing product development cycles and shortening the time-to-market of new products [31]. AM has become a popular method to produce not only prototypes and molds, but increasingly AM is being used to fabricate components for engineered products for a range of industrial applications. AM production of multi-material components and devices is of considerable interest as well, allowing for fabrication of elastomeric hinges, integrated grips, and other features where material changes can achieve enhanced functionality [36], reduced part counts, and streamlined assembly. The ability to selectively deposit multiple materials with different mechanical properties also offers design freedom for producing final parts with tunable failure locus and resistance to fracture. Depending on how the materials are printed and dispersed, additional benefits such as enhanced mechanical properties can also be achieved as seen from the work of Sugavaneswaran et al. [51, 52].

Even with rapid advances of AM technologies, there are still a number of concerns that need to be addressed to ensure efficient processing of robust structures and

components. For fabrication with a single material, porosity and anisotropy can be issues due to the associated layer-by-layer printing process, the curing or solidification process, and other factors. Imperfect or weak bonding between layers can lead to delamination and breakage under stress [23, 53]. Surface finishes are often poor and can introduce porosity, making prototypes susceptible to moisture infiltration [23]. Previous research has confirmed print build orientation has a significant effect on the mechanical properties in uniaxial tension of a number of AM systems [28-30, 35], including those printed with multiple polymers [51, 52]. Researchers have primarily employed the common dog-bone tensile test specimen in their studies of modulus, strength, and fatigue resistance [28, 30, 54-58]. In a recent study, Dimas et al. characterized the fracture resistance of composites using the single edge notch specimen printed from a multi-material printer, indicating that specific topological arrangements of soft and stiff phases can be used as a design mechanism to enhance mechanical properties of composites [59].

Recognizing prior studies of strength of monolithic and multi-material AM systems, this study extends characterization by assessing the fracture resistance and locus of failure of additively manufactured materials tested as laminated beam specimens. Specifically, trilayer constructions involving two printed polymers are used – a softer interlayer joining two stiffer portions – resulting in specimens resembling adhesively bonded joints. Several specimen geometries are developed and evaluated, including double cantilever beam (DCB), tapered double cantilever beam (TDCB), and peel configurations, all of which have origins in commonly used fracture tests for adhesive bonded joints and laminated composites. The DCB is a common configuration used for the evaluation of adhesive bonds that is well suited for testing joints consisting of an

adhesive joining adherends that consist of metal, fiber-reinforced composite, or other materials [20]. The TDCB is another configuration used for testing adhesive bonds. The tapered profile of the beam height is designed so that at a constant load, the strain energy release rate is independent of crack length over most of the specimen length; this design often, reduces the maximum stresses reached in the adherends as well [20].

The fracture energy and locus of failure are important characteristics used to evaluate the performance of adhesive bonds, and the authors believe these properties are also important for both homogenous AM materials as well as those containing interfaces between dissimilar components. Of specific interest in this research is whether these interfaces are inherently weaker than the surrounding bulk printed materials, resulting in a weakened region that could lead to product failure under quasi-static, sustained, or cyclic loading conditions experienced in service. This study focuses on measuring the quasi-static behavior of such interfaces by proposing, fabricating, and evaluating specimens that may be appropriate for characterization of a range of AM systems. In addition to being used for design and analysis purposes, properties obtained could be used to optimize multi-material compatibility and improve printing algorithms, perhaps through alternate patterning or architectures of interface, to result in stronger, tougher, and more durable products. Incorporating multi-material printing in AM-fabricated components offers significant design flexibility for altering stiffness, energy dissipation, strength, fracture, and other properties, especially if the multi-material interfaces can be optimized for robust performance.

Experimental Methods

Materials

The materials involved in this study are two photopolymers used in the Stratasys PolyJet material jetting AM process (Stratasys, Eden Prairie, MN). In this process, layers of multiple acrylic-based photopolymers are selectively deposited onto a build tray via inkjet printing. The jetted photopolymers are quickly cured by UV lamps that are mounted on the printing block. Models printed by this process are incased in a sacrificial support material to ensure dimensional stability, though it can be easily removed after printing via water jet cleaning.

The material system of interest includes two photopolymers: TangoBlackPlus (TB) and VeroWhitePlus (VW), and the resulting interface between them. TB is a black photopolymer that exhibits some rubber-like or elastomeric characteristics, albeit with considerable time dependence, while VW is a white, opaque photopolymer that is significantly stiffer in comparison to the TB. Their respective moduli, tensile strengths, and glass transition temperatures (T_g) are conveyed in Table 3.1. Several researchers have studied this particular system in the past. For example, Barclift et al. demonstrated when multiple VW parts are printed on the same tray, the part spacing has a significant effect on the mechanical properties [35]. Moore et al. analyzed fatigue strength of the TB/VW interface, indicating that the TB/VW interface failed prematurely in 25% of the dogbone specimens tested [36]. Sugavaneswaran et al. observed improved strength in a TB tensile specimen by incorporating cylindrical reinforcements of VW throughout [51].

Table 3.1. Table of material properties for TangoBlackPlus and VeroWhitePlus [60, 61]. VeroWhitePlus PolyJet Materials Details | RedEye 3D Printing Services, 2015. Tango Materials | 3D Modeling 3D Printing Materials, Rubber-Like, 2015. Used under fair use, 2015.

	TangoBlackPlus (TB)	VeroWhitePlus (VW)
Young's Modulus (MPa)	0.1 to 0.3	2000 to 3000
Tensile Strength (MPa)	1.8 to 2.4	55 to 65
T_g (°C)	-10	52 to 54

Specimen Fabrication

To evaluate the fracture resistance of trilayer specimens produced with this material system, several double cantilever beam [16, 20] and T-peel test [62] configurations, consisting of layers of TB sandwiched between VW layers, were designed, printed, and tested. In keeping with relevant literature and specimens for testing adhesive bonds, the VW layers will be referred to as adherends and the TB interlayer will be referred to as the adhesive, though these were in fact all printed in a single AM process via a Stratasys Connex 350 system. Each layer deposited is approximately 0.032 mm thick and for all specimens considered, the total thickness of the TB central layer is kept constant at 0.32 mm. All specimens contained a chevron notch printed in the width and thickness directions to facilitate crack initiation within the TB interlayer. The sandwich configuration and TB interlayer thickness were common to all specimens, which were distinguished by the VW adherend thicknesses or method used to reinforce the adherend through bonded auxiliary adherends. These configurations, all of 9.9 mm width, included the following (along with respective layer thickness), each of which is illustrated in Figure 3.1:

- Aluminum-supported DCB (Al-DCB): 1 mm VW – 0.32 mm TB – 1 mm VW sandwiches bonded to 3.8 mm thick auxiliary aluminum adherends machined with endblocks.
- Fully-printed DCB (FP-DCB): 4.95 mm VW – 0.32 mm TB – 4.95 mm VW sandwiches with integral endblocks printed during fabrication.
- Steel-backed DCB (St-DCB): same as the FP-DCB configuration but VW adherends are backed with 0.759 mm thick steel strips to reduce adherend deformation.
- TDCB: entire specimen, with 0.32 mm TB interlayer and varying adherend thickness printed in their entirety.
- T-peel: 0.32 mm VW – 0.32 mm TB – 0.32 mm VW sandwiches tested directly in T-peel configuration.

Expected to minimize printing costs and adherend energy dissipation that can obscure fracture energy measurements, the aluminum-supported (Al-DCB) specimens were made by bonding printed sandwich strips between machined aluminum adherends. Prior to bonding, the 6061-T6 aluminum adherends were abraded with 120 grit sandpaper using a random orbital sander and cleaned in tap water using an ultrasonic cleaner (Fisher Scientific, Waltham, MA) for 3 minutes. The auxiliary adherends were dried in an oven at 110°C for 1 hour. The printed strips were bonded onto auxiliary aluminum adherends using LORD 320/322 epoxy adhesive (LORD Corporation, Cary, NC). A paper spacer was placed in the notch to prevent this adhesive from seeping into the initial debond. The specimens were clamped and left to cure at room temperature for 24 hours. After 4 hours of curing, excess adhesive was removed with a putty knife to improve visibility of the central layers for crack length measurements.

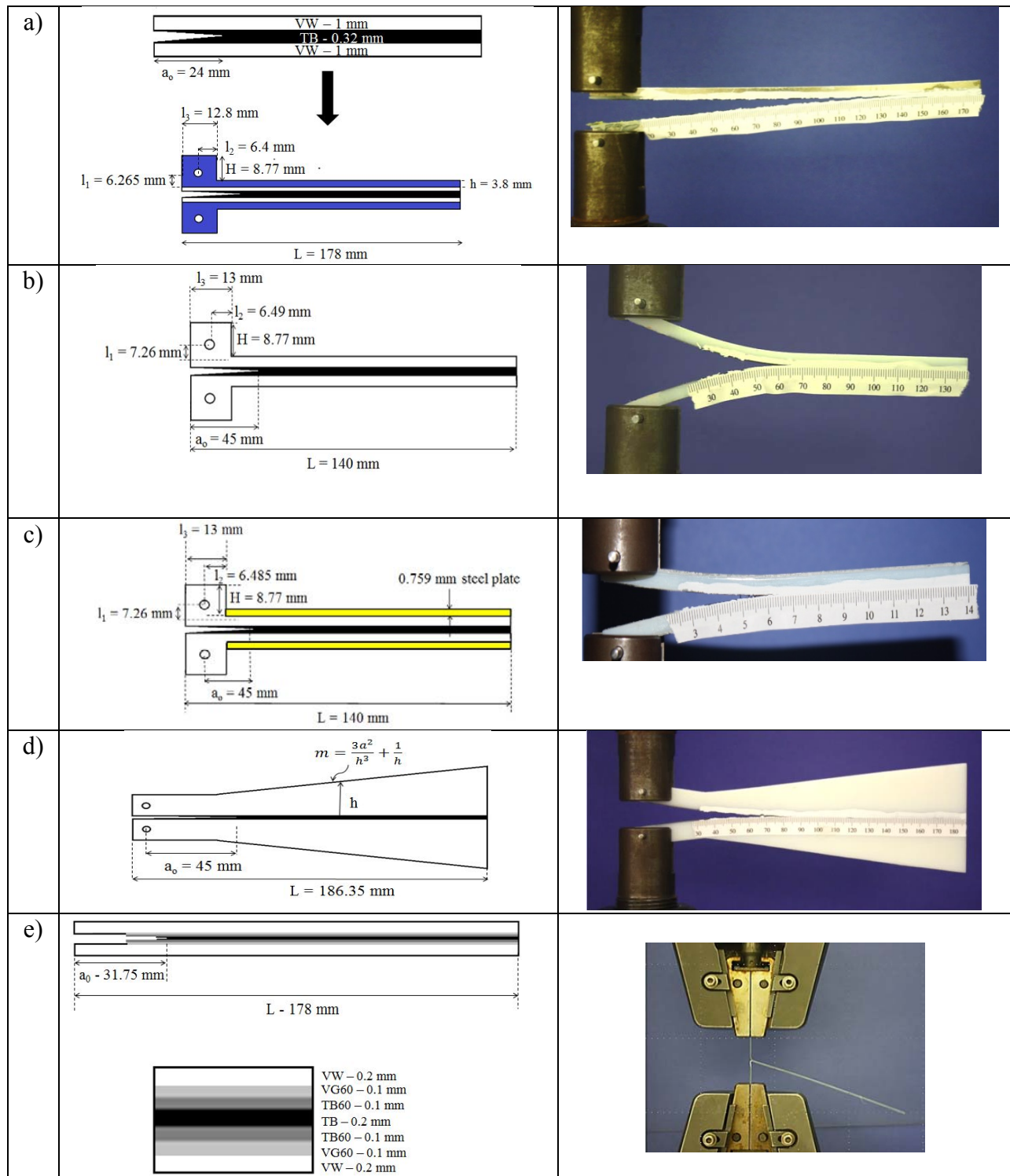


Figure 3.1. Illustrations of test configurations and photos of representative specimens during testing: a) aluminum-supported (AL-DCB), b) fully-printed (FP-DCB), c) steel-backed DCB (St-DCB), d) TDCB, and e) T-peel geometries.

Though using more polymer, the fully-printed (FP-DCB) specimens minimized auxiliary specimen preparation, as they were ready to test without additional bonding procedures following printing. As shown in Figure 3.1b, these specimens exhibited the most deformation during testing. Concerns with viscoelastic and plastic dissipation within the polymeric adherends, and the complications introduced for analysis, led to the addition of 22 gauge (0.759 mm) steel strips, bonded to the back of the specimen arms using the bonding method described above. The steel-backed (St-DCB) specimens resulted in somewhat smaller adherend deformations than the FP-DCB. Fully-printed TDCB specimens were fabricated using the tapered profile generated according to the geometry factor m given by [19, 20]:

$$m = \frac{3a^2}{h^3} + \frac{1}{h} \quad (3.1)$$

While typical adhesive tests have used a value of 2 for m when designing the TDCB [63, 64], a value of 3.5 is chosen for m in an effort to conserve material, while reducing the effects of dissipation and yielding of the adherends during testing. Though using the most printed polymer, these TDCB specimens resulted in reduced adherend deformation; such configurations are often advocated for adhesive testing because of the constant strain energy release rate nature of the specimen, the ease of analysis, and reduced adherend stresses.

In addition to the four DCB configurations, T-peel tests were also conducted to evaluate the peel resistance of the TB/VW interface. The same type of sandwich strips used for the Al-DCB specimens were used in unsupported fashion as T-peel specimens. Variations of this configuration involving interlayer gradients were also tested. The gradient version is illustrated in Figure 3.1e; in addition to VB adherends and a TB

central layer, blended layers of TangoBlackShore60 (TB60), a digital mixture of VW with a majority of TB, and VeroGrey60 (VG60), a digital mixture of TB with a majority of VW, were incorporated in the gradient specimens.

Build Orientation

AM processes allow for components to be printed in different orientations, offering enhanced design and construction flexibility, but also resulting in nominally identical products that may have very different properties. In PolyJet fabrication, printed primitives are jetted in the direction of the travel of the printing block (x-axis); jetted 'lines' (composed of several individual drops) are rastered along the y-axis to complete a layer. Subsequent layers are then built up in the Z-direction. The print resolution of the Objet Connex 350 offers respective resolutions in the x-, y-, and z-directions of 0.043 mm, 0.043 mm (as per manufacturer-stated 600 dpi resolution), and 0.032 mm (when printing multiple materials). Depending on the printing direction used on any given fabricated item, adjacent material may effectively be co-cured, because of near simultaneous deposition, or can result when liquid monomer is deposited at a later time on a previously cured layer. This difference could possibly result in very different molecular blending, interdiffusion, and integrity. Of particular interest in this work is the effect orientation of the interfaces and interlayer resulting from the build direction has on the structural integrity of the fabricated specimens.

For purposes here, a modified form of the orientation nomenclature given by ISO / ASTM 52921 with reference to the TB interlayer [65] is used. The print orientation for each specimen will be designated by the plane of the interlayer and the direction of load application. For example, the DCB and TDCB specimens shown in the left portion of

Figure 3.2 are printed in the $\bar{x}zy$ orientation, where the first letter with an arrow above (\bar{x}) indicates the direction of crack propagation; the second letter (z) is the direction of the specimen and interlayer width; and the last letter (y) is the direction of load application. Both FP-DCB specimens and the AM strips used for AI-DCB specimens were printed in the $\bar{x}yz$, $\bar{x}zy$, $\bar{y}xz$, and $\bar{y}zx$ -orientations to explore the effect of print orientation on fracture resistance, as shown in the middle and right images of Figure 3.2. Additionally, the $\bar{x}zy$ and $\bar{y}zx$ AM strips used for the AI-DCB were printed using different printing arrangements: single and gang-printed, both encased within support material, as shown in Figure 3.3. The latter configuration was used to investigate the possibility that low fracture energies, initially obtained for the single-printed specimens, resulted from difficulties in printing the tall and narrow strips on their edge. As will be shown later, however, both printing configurations yielded similar results for the $\bar{x}zy$ orientation specimens, and the anomalously low fracture values initially obtained for single-printed specimens resulted from a different printing error. AM strips, printed in the $\bar{x}yz$ orientation in the single-printed arrangement, were also used for T-peel tests as shown in the right portion of Figure 3.2.

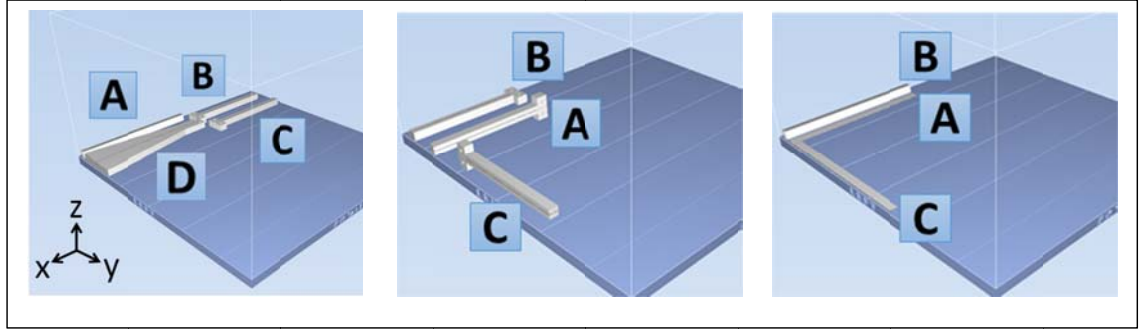


Figure 3.2. Illustration of various print orientations used to fabricate specimens. Left: $\bar{x}zy$ orientation for A) AM sandwich strips, B) and C) FP-DCB, and D) TDCB specimens. Middle: fully-printed DCB specimens oriented A) $\bar{x}yz$, B) $\bar{x}zy$, and C) $\bar{y}xz$. Right: Al-DCB specimens oriented A) $\bar{x}yz$, B) $\bar{x}zy$, C) $\bar{y}xz$. Note: $\bar{y}zx$ orientation is not pictured.

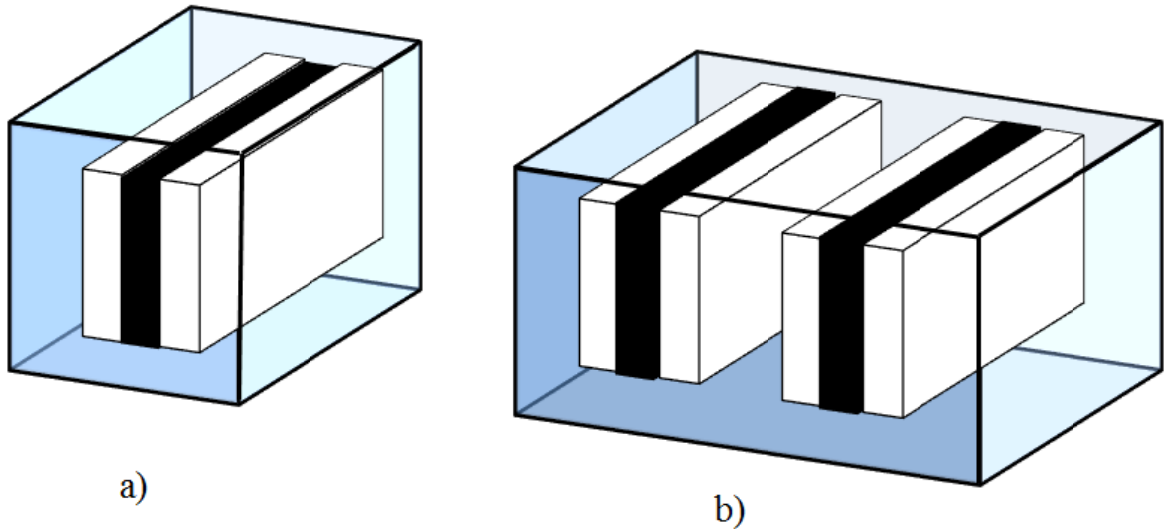


Figure 3.3. Comparison of a) single and b) gang-printed AM strips

Test Procedure

Following accepted practices for testing DCB-type specimens, typewriter correction fluid was applied to the TB bondline as an aid in visualizing the crack tip and paper rulers were affixed onto all DCB specimens in order to facilitate measurements of the crack length. Mode I tests were conducted using a 5800R Instron (Canton, MA) at a crosshead displacement rate of 1 mm/min, unless otherwise noted. Mode I fracture energies are calculated using corrected beam theory (CBT) [19, 20].

$$G_{Ic} = \frac{3P\delta}{2B(a+\hat{a})} \cdot \frac{F}{N} \quad (3.2)$$

where G_{Ic} is the mode I fracture energy; a is the crack length; P and δ are the applied load and the end displacement at crack propagation, respectively; F is the large displacement correction; N is the load block correction; B is the width of the specimen; and \hat{a} is the crack length correction. The large displacement correction F and the load block correction N are calculated by [19, 20]:

$$F = 1 - \frac{3}{10} \left(\frac{\delta}{a} \right)^2 - \frac{3}{2} \left(\frac{\delta l_1}{a^2} \right) \quad (3.3)$$

$$N = 1 - \left(\frac{l_2}{a} \right)^3 - \frac{9}{8} \left[1 - \left(\frac{l_2}{a} \right)^2 \right] \frac{\delta l_1}{a^2} - \frac{9}{35} \left(\frac{\delta}{a} \right)^2 \quad (3.4)$$

The crack correction \hat{a} is used as a means to correct the crack length for a beam that is not perfectly built in. This correction is calculated by plotting the cube root of the corrected compliance $(C/N)^{1/3}$ vs. the observed crack length a ; representative results are shown in Figure 3.4-- the excellent linear fit suggests appropriateness of analysis method. Extrapolation of the linear fit of this plot will yield \hat{a} as the negative of the abscissa intercept.

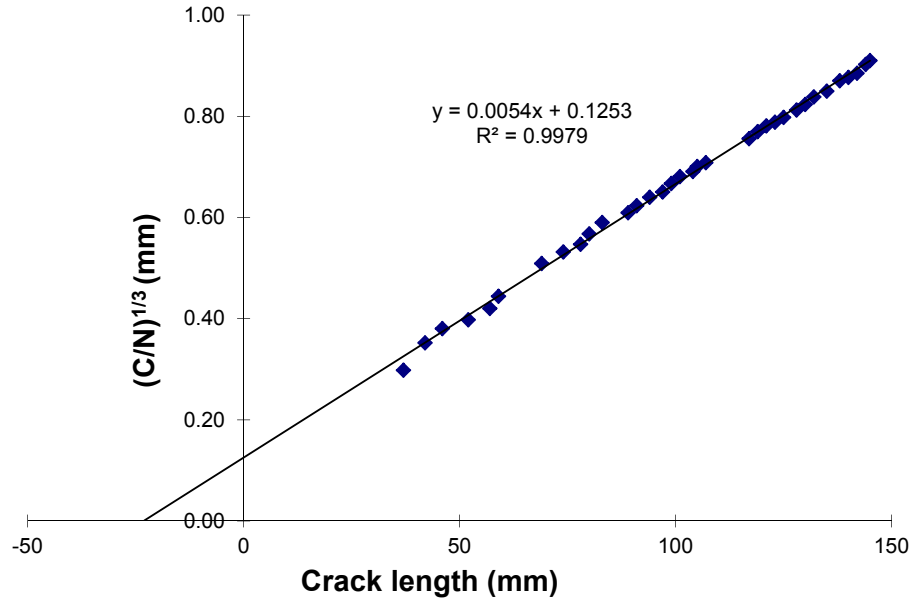


Figure 3.4. $(C/N)^{1/3}$ vs. crack length a for Al-DCB at 1 mm/min

As with the DCB, the mode I fracture energies for the TDCB are also calculated using CBT [20].

$$G_{Ic} = \frac{4P^2}{E_s B^2} \cdot m \cdot \left[1 + 0.43 \left(\frac{3}{m} \right)^{\frac{1}{3}} \cdot a^{\frac{-1}{3}} \right] \quad (3.5)$$

where is E_s Young's Modulus of VW and m is the specimen geometry factor previously described. The modulus of the VW is measured to be 0.96 GPa based on the slope of the compliance C vs. crack length a obtained by CBT [20]. In addition to CBT, the experimental compliance method (ECM) was also used as an alternate method to calculate the fracture energy for all specimens considered above, but as seen in the appendix, fracture energies calculated from ECM were found to be more variable in comparison to CBT. Thus, CBT was used as the primary method for determining and comparing fracture energies among the test specimens.

The T-peel tests were performed at a crosshead displacement rate of 254 mm/min, in accordance to ASTM D1876 [62] in the same Instron load frame. The apparent fracture energy in peel (defined by twice the peel strength per D1876) is given by:

$$G_c = \frac{2P}{W} \quad (3.6)$$

where P is the applied load and W is the specimen width. All of the above tests (DCB, TDCB, and T-peel) were conducted at room temperature.

Results and Discussion

Specimen Comparison

To evaluate the proposed specimen configurations, samples were printed in the same orientation ($\vec{x}zy$ -orientation) and interlayer thickness to assess the effectiveness of each configuration (Al-DCB, FP-DCB, St-DCB, TDCB; Figure 3.2a). Tests were conducted within 1-2 days of printing in order to minimize effects of aging or other phenomena. Figure 3.5 shows the mode I fracture energies obtained for two replicates of the four test configurations, with good consistency observed for the replicates. The downward trends for the constant thickness DCB fracture energies reported herein are believed to be associated with the rate dependence of the interlayer, as will be addressed in a later section.

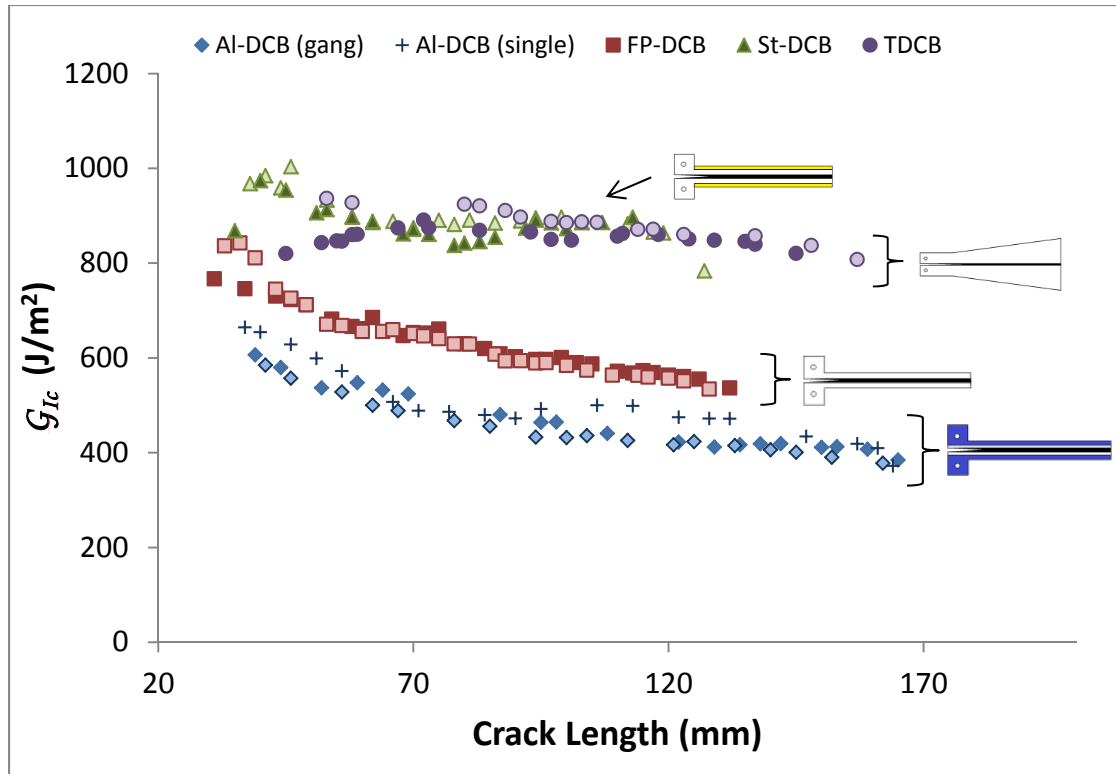


Figure 3.5. G_{Ic} vs. crack length for all DCB configurations in the $\bar{x}zy$ -orientation: blue diamonds (Al-DCB), red squares (FP-DCB), green triangles (St-DCB), and purple circles (TDCB). Note: data points of the Al-DCB are shown for both single and gang-printed specimens as seen in Figure 3.3.

There are significant differences among the specimen configuration results in terms of both the fracture energy and locus of failure. The Al-DCB configuration results in the lowest G_{Ic} of $459 \pm 63 \text{ J/m}^2$ and the loci of failure appear largely cohesive.. Figure 3.5 demonstrates that the fracture energies of the Al-DCB are similar regardless of whether the AM strips single or gang-printed specimens. Optical photographs and SEM images of the fracture surfaces are shown in Figure 3.6a.

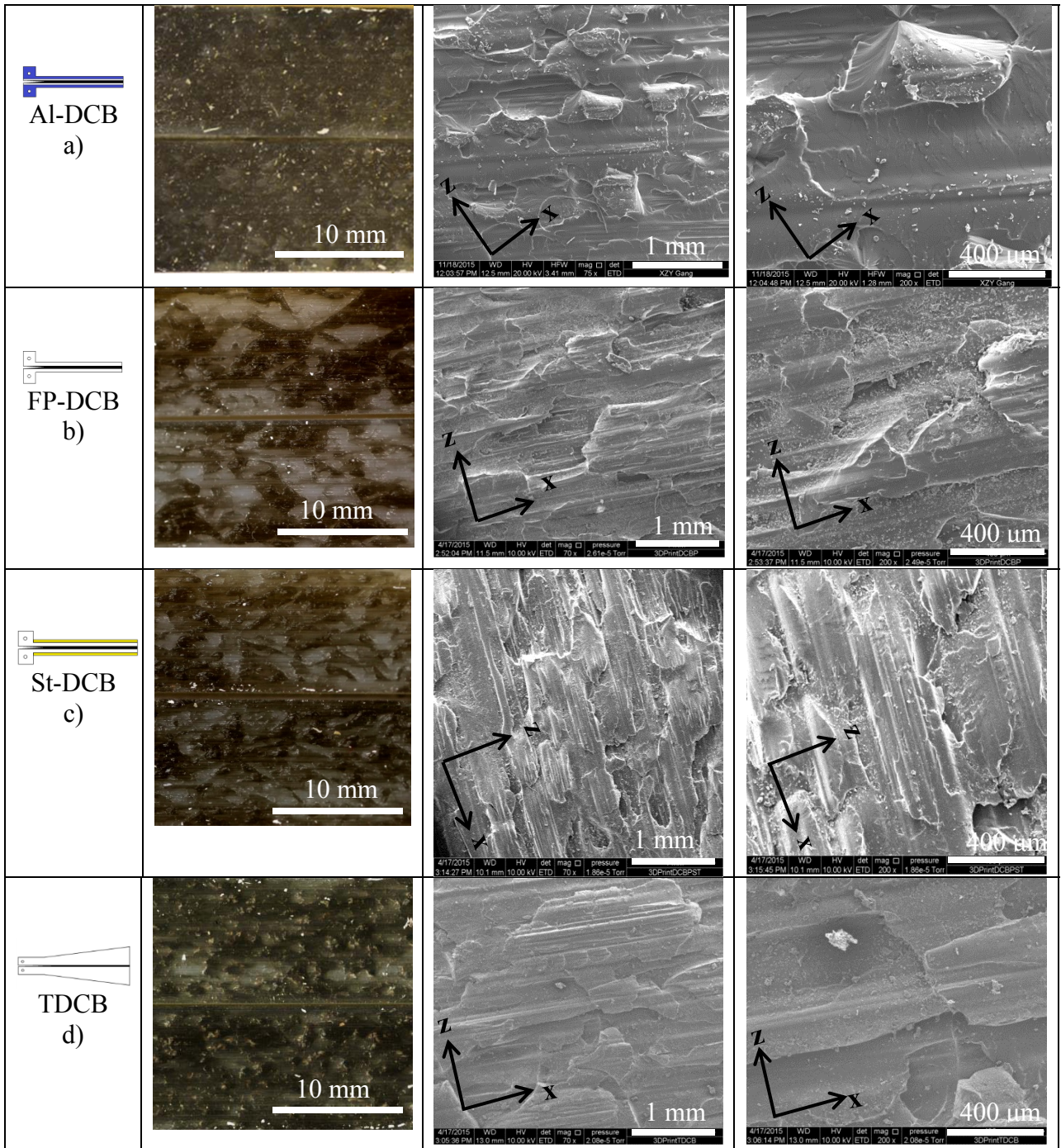


Figure 3.6. Failure surfaces of specimens with corresponding SEM images. Plane of the interlayer is oriented on the xz-plane, with the direction of crack propagation aligned along the x-axis.

In contrast to the rather distinct black or white failure surfaces that will be shown later for specimens prepared with printed VW to TB interfaces in the xy-plane, the failure surfaces for these specimens (with xz-plane interfaces) often appear grey to the naked

eye. Polymer blending of the TB and VW may be occurring, as adjacent VW and TB lines are deposited simultaneously on each pass of the printer head, resulting in a potential interphase region [66] that is tougher than the less blended interface between sequentially applied TB and VW layers that will be discussed later. The reason that the Al-DCB specimens consistently resulted in the lowest fracture energies likely arose from the fact that these specimens, upon unloading after total failure, showed no residual deformation. The other specimen types all showed either permanent or temporary curvature upon failure, indicative of plastic and/or viscoelastic deformation and energy dissipation within the adherends, which would result in higher apparent fracture energies using the analysis methods employed. Also, since all specimens were tested at the same crosshead displacement rate, the average crack propagation rates were considerably different. This rate dependent contribution to the measured fracture energies complicates direct comparisons in Figure 3.5 and will be addressed in a later section.

The three fully-printed specimen configurations all resulted in significantly higher fracture energies and also exhibited fibrillation within the interlayers during testing. Polymer fibrillation can dissipate considerable energy through plastic or viscoelastic deformation, and could arise from surface imperfections or voids, acting as stress concentrations that subsequently expand under the action of the applied tensile stress to form the fibril structure [67, 68]. The TB material reportedly has a random degree of porosity [36], which could facilitate the development of polymer fibrils during mode I testing. Such behavior is known to be a major mechanism of increased fracture energy [67, 68], and may have contributed to this clear trend shown in Figure 3.5 for all fully-printed specimens. SEM images also show signs of localized drawing and plasticity,

some of which may have initiated at the boundaries of defects and voids produced by the printing process.

The fully-printed DCB configurations resulted in higher values of G_{Ic} as obtained by CBT, but as mentioned previously, the adherends experienced significant viscoelastic deformation during testing, thereby dissipating energy and exaggerating the measured G_{Ic} values. While bonding steel plates to the adherends was thought to potentially reduce plastic deformation and dissipation, adding them made little difference to the measured fracture energy. In fact, the steel plate-backed DCB configuration resulted in even larger G_{Ic} values compared to the non-reinforced, fully-printed configuration. This is due to the larger amount of energy being dissipated to deform both the VW and the steel strips during testing. Separate calculations from beam theory confirm that the stresses experience by the specimen exceeded the yield strength of the steel. Following testing, all the fully printed specimens exhibited residual curvature, though the FP-DCB and TDCB specimens straightened out quite completely after a day or two, suggesting viscoelastic recovery, whereas the St-DCB retained considerable curvature due to plastic deformation of the steel. It is noted that fabricating the TDCB required the most amount of polymer to print due to the tapered profile of the beam height, leading to longer print times and production costs than the AM sandwich and flat DCB configurations.

Print Orientation

To evaluate the effects of print orientation, the fully-printed specimens were printed in four orientations ($\bar{x}yz$, $\bar{x}zy$, $\bar{y}xz$, $\bar{y}zx$), as shown in the middle image of Figure 3.2, though the $\bar{y}zx$ orientation is not shown. The variation of fracture energy against

crack length for non-backed, fully-printed DCB specimens from the four print orientations is shown in Figure 3.7, with two specimens tested for each orientation showing good consistency. Extensive polymer fibrillation is observed during tests for all of the fully-printed DCBs. Specimens printed in the $\bar{x}zy$ orientation, where the applied load during testing is perpendicular to the direction of the print build, are shown to have higher fracture energy than the other two orientations, where the applied load is in the same direction of the print build. This corresponds with prior research that indicates that the strength of PolyJet materials is poor when the load is applied in the direction of the print build, wherein failure occurs predominantly at the interlayer boundaries [32, 33]. The FP-DCBs were shown to experience significant viscoelastic deformation during testing, which may have exaggerated the measured fracture energies reported in Figure 3.7.

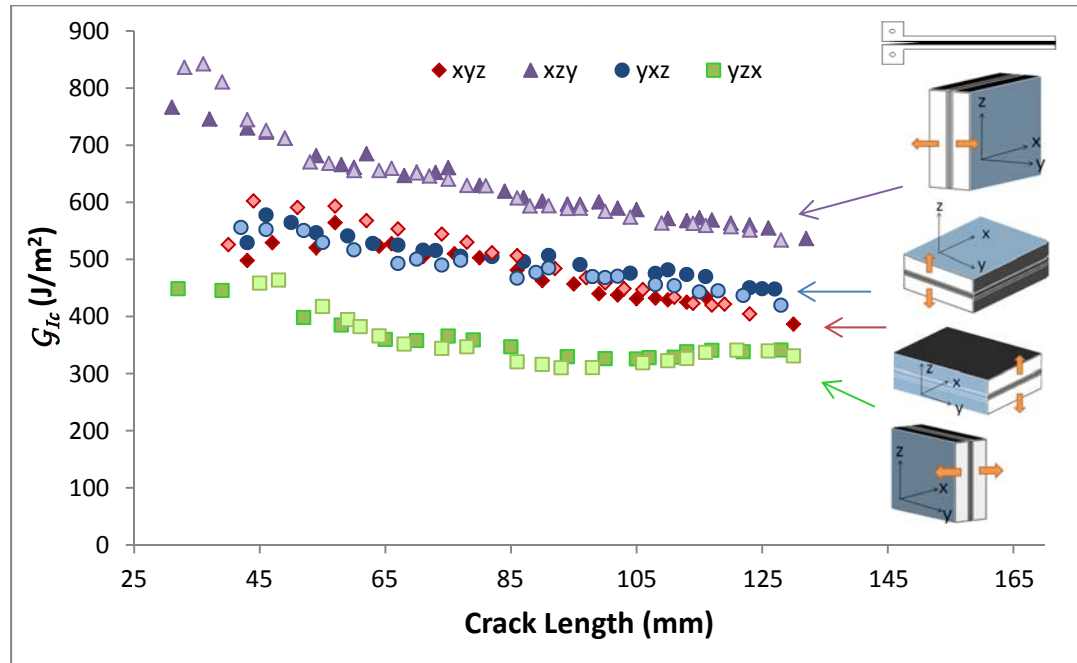


Figure 3.7. G_{Ic} vs. crack length for the fully-printed DCB configurations based on orientation: red diamonds ($\bar{x}yz$), purple triangles ($\bar{x}zy$), blue circles ($\bar{y}xz$), and green squares ($\bar{y}zx$).

Images of the associated failure surfaces are shown in Figure 3.8, where the locus of failure always appears to occur at or near the TB to VW interface for the $\bar{x}yz$, $\bar{x}zy$, and $\bar{y}xz$ specimens. The fractures, however, alternate back and forth between the VW arms across apparently random fragments of TB. Figure 3.8b indicates that the failure surface of the $\bar{x}zy$ specimen has a grey color or appearance that may suggest polymer blending between TB and VW, possibly resulting in an interphase region that is tougher than the less blended interface. In comparison to Figure 3.6a, the appearance of the layer boundaries is not as apparent for this configuration. For the specimens built in the $\bar{x}yz$ and $\bar{y}xz$ orientation, there is a clear distinction between the TB and VW sides of the fracture surface, suggesting a much lower degree of polymer blending, as VW and TB were printed sequentially, on separate passes of the printhead. Thus, a TB (VW) layer would have been deposited on a cured VW (TB) layer deposited in a previous pass. The SEM images shown in Figure 3.8a and Figure 3.8c exhibit discretized failure surfaces with some evidence of plastic deformation tufts distributed across the failure surfaces. The discretized or fragmented TB layer fracture features are somewhat reminiscent of mud crack patterns commonly seen in coatings, adhesive layers [69], and other desiccation cracks [70], though the cause of such formations in these AM specimens is not fully understood. As with classic mud crack patterns, the segment boundaries appear quite random and do not align with the print axes. High residual stresses within the rather soft interlayer, coupled with porosity and defects, could contribute to intralayer cracks, though the pattern is rather unusual. For all three configurations, the growing crack clearly alternated back and forth from one interface to the other, though there is a rate dependence that will be addressed in a later section. Lastly, the FP-DCB printed in

the $\bar{y}zx$ orientation resulted in the lowest fracture energies of all the orientations considered for this comparison, as the failure surface in Figure 3.8d appears more cohesive within the interlayer (albeit closer to one adherend) than the more interfacial failure surfaces seen for the other specimens. The SEM images for the $\bar{y}zx$ specimen also show some signs of polymer drawing, though the feature sizes are much smaller in contrast to the other orientations. In the $\bar{y}zx$ orientation, the print head deposits the TB and VW in a rapid sequential fashion along the print path, printing the VW first, followed by the TB, and then back to VW. This is in contrast to the $\bar{x}zy$ orientation, where the TB and VW are co-printed simultaneously by the printhead. Reduced fracture properties for the $\bar{y}zx$ specimens may have occurred as a result of sequential vs. simultaneous deposition and curing, or with the roller smearing material in an unusual manner.

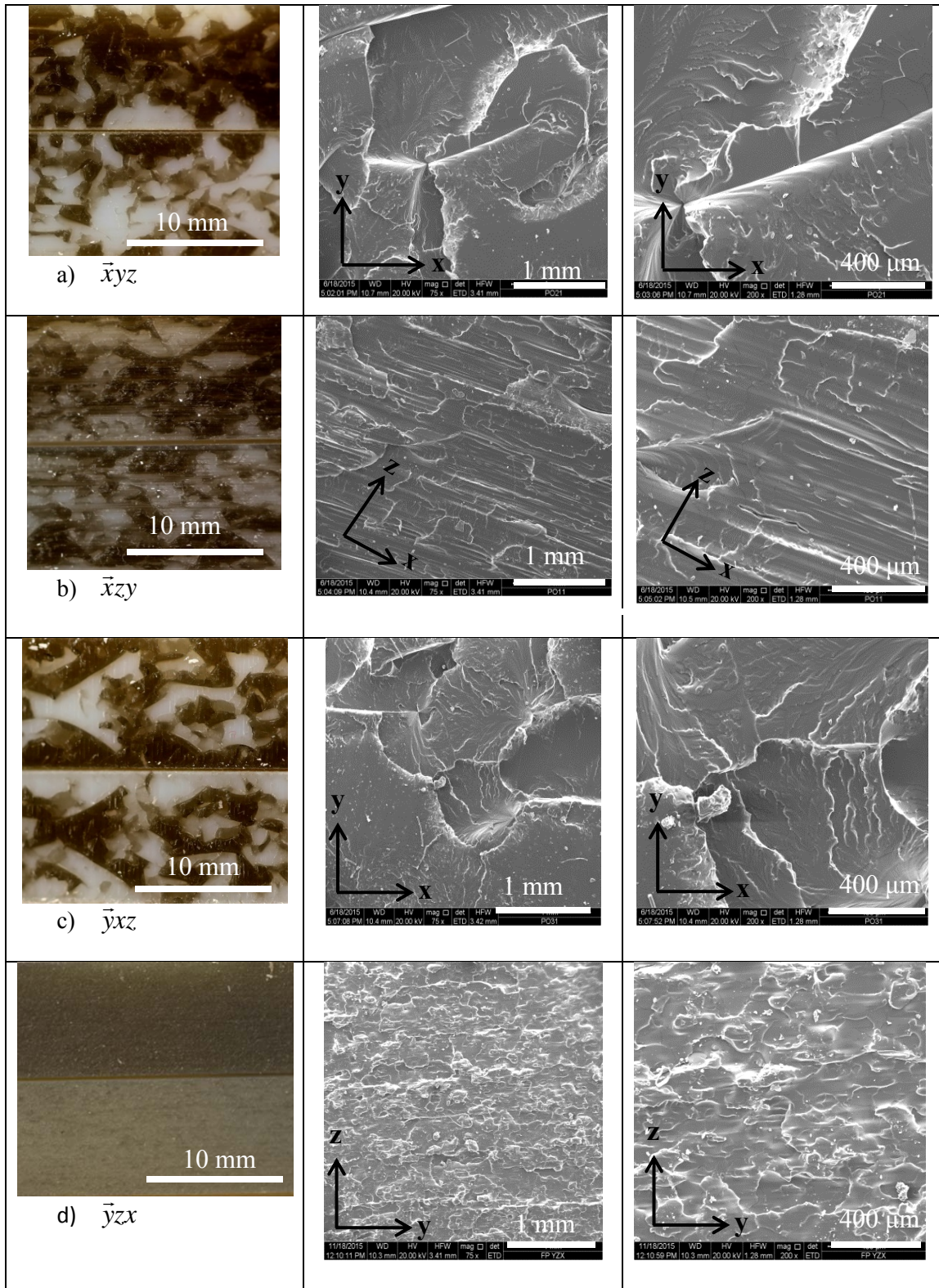


Figure 3.8. Failure surfaces and SEM images of fully-printed DCBs printed in the a) $\bar{x}yz$, b) $\bar{x}zy$, c) $\bar{y}xz$, and d) $\bar{y}zx$ orientation.

The Al-DCB strips were also printed in the same four orientations, as shown in the right image of Figure 3.2a, with two specimens tested for each orientation. In comparison to the fully-printed configuration, the Al-DCB specimens had the shortest test time as there was minimal adherend deformation and the majority of the energy dissipation is focused on crack propagation about the TB interlayer. The measured fracture energies as a function of crack length are shown on Figure 3.9, revealing stark differences in fracture resistance among the three print orientations. In addition, a dramatic contrast is evident when comparing the measured fracture energies between the Al-DCB and FP-DCB configurations. While the fracture energy of the FP-DCB configuration was seen to be higher in the $\bar{x}zy$ orientation, this is not seen for the Al-DCB configuration.

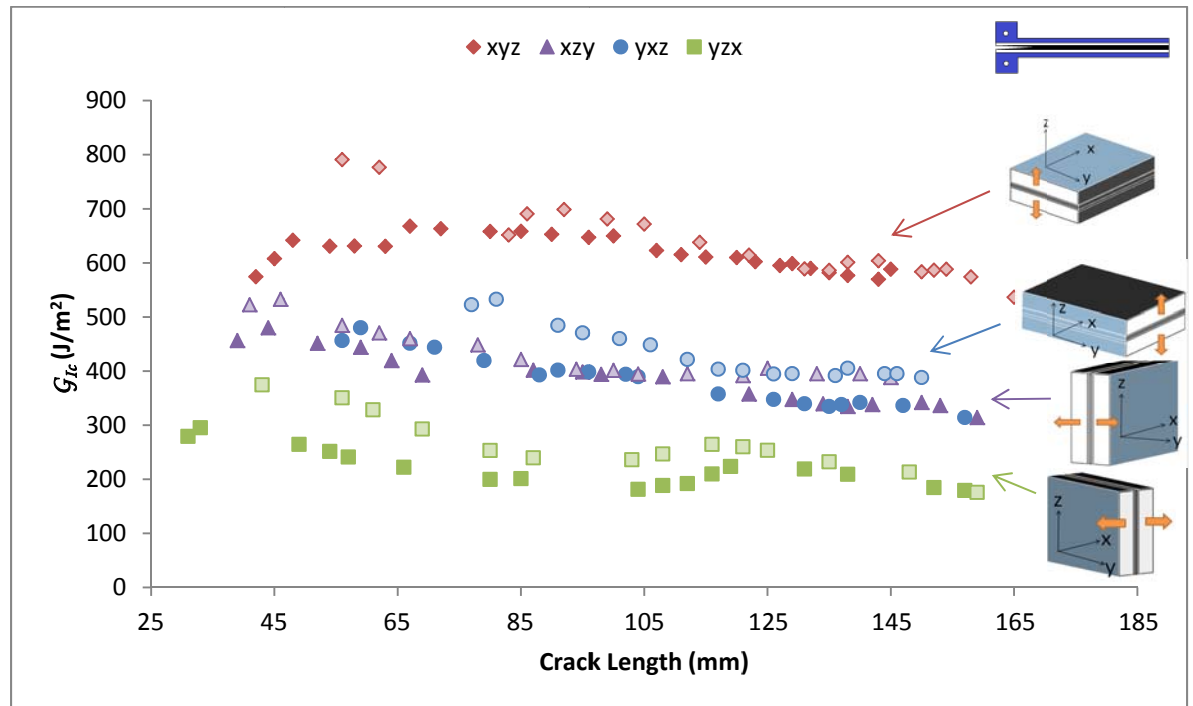


Figure 3.9. G_{Ic} vs. crack length for the Al-DCB configurations based on orientation: red diamonds ($\bar{x}yz$), purple triangles ($\bar{x}zy$), blue circles ($\bar{y}xz$), and green squares ($\bar{y}zx$). Note: data points in the $\bar{x}zy$ and $\bar{y}zx$ orientation represent “gang-printed” specimens.

The loci of failure within specimens for the $\bar{x}yz$ and $\bar{y}xz$ orientations are shown to alternate from one adherend interface to another, again somewhat reminiscent of alternating locus of failures reported for adhesive joints [71-74], although in a much more random manner. Distinct polymer tufts indicative of plastic drawing are left on the failure surface after testing as shown on the top and bottom portions of Figure 3.8 and Figure 3.10. While the FP-DCB resulted in equivalent fracture energies for the $\bar{x}yz$ and $\bar{y}xz$ print orientations, this was not seen in the Al-DCB configuration, as the $\bar{x}yz$ orientation is shown to be the highest in terms of fracture energy. Once again, the AM strips gang-printed in the $\bar{y}zx$ orientation are shown to have the lowest fracture energy of all the orientations, possibly due to the same printing phenomenon that occurs when printing the FP-DCB in the same orientation. The failure surfaces for both FP-DCB and Al-DCB are quite consistent for the same print orientation, though the Al-DCB $\bar{x}zy$ specimen shows much less discretization with the interlayer and a clearly cohesive failure. The locus of failure in the Al-DCB $\bar{y}zx$ specimen shows a similar cohesive crack that is farther from the interfaces.

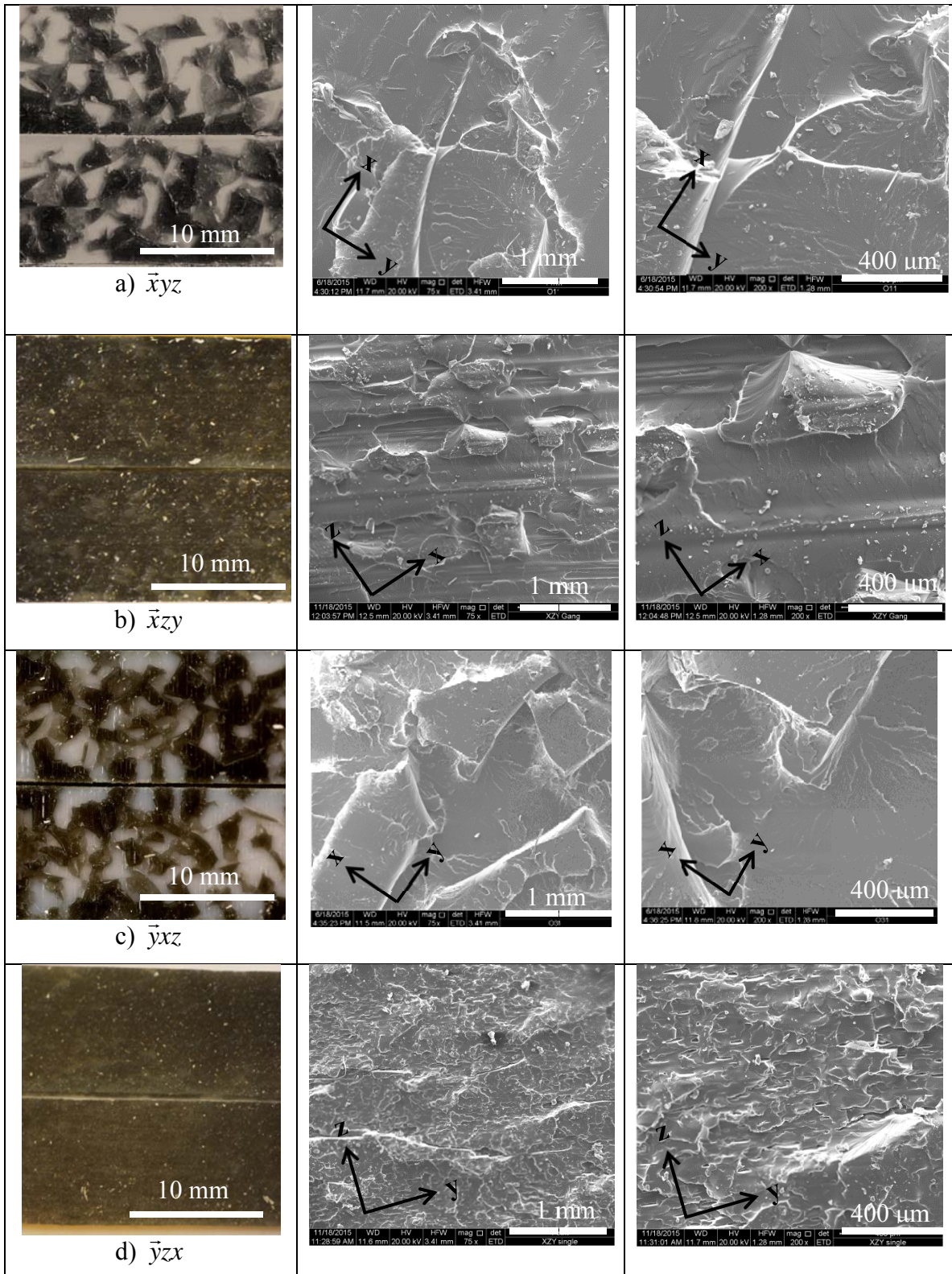
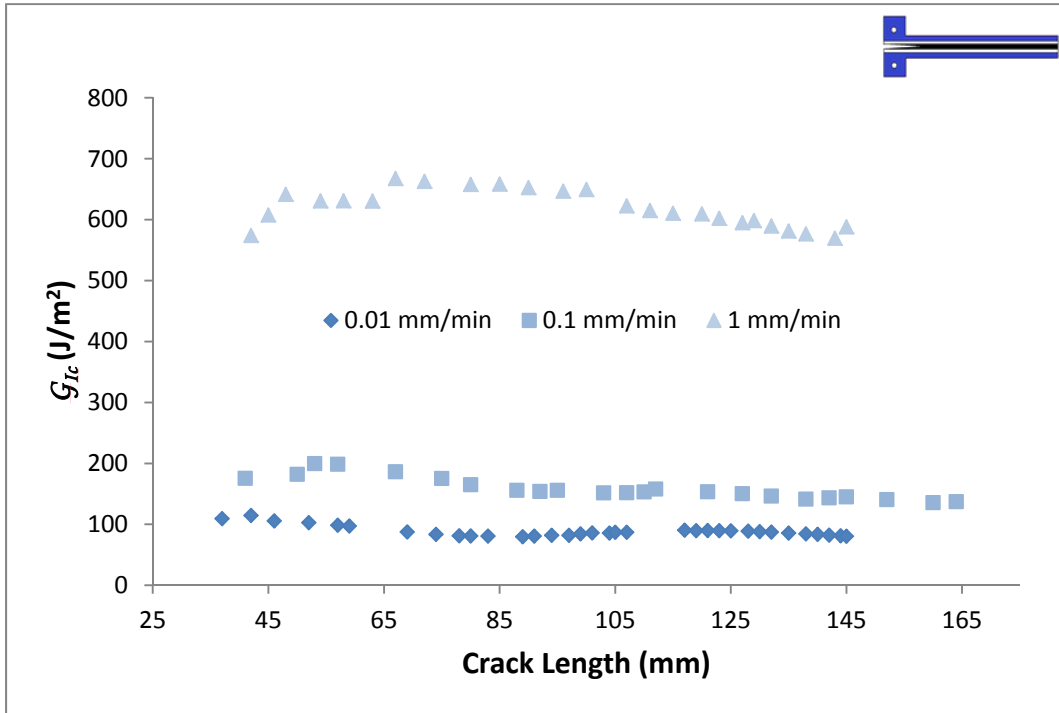


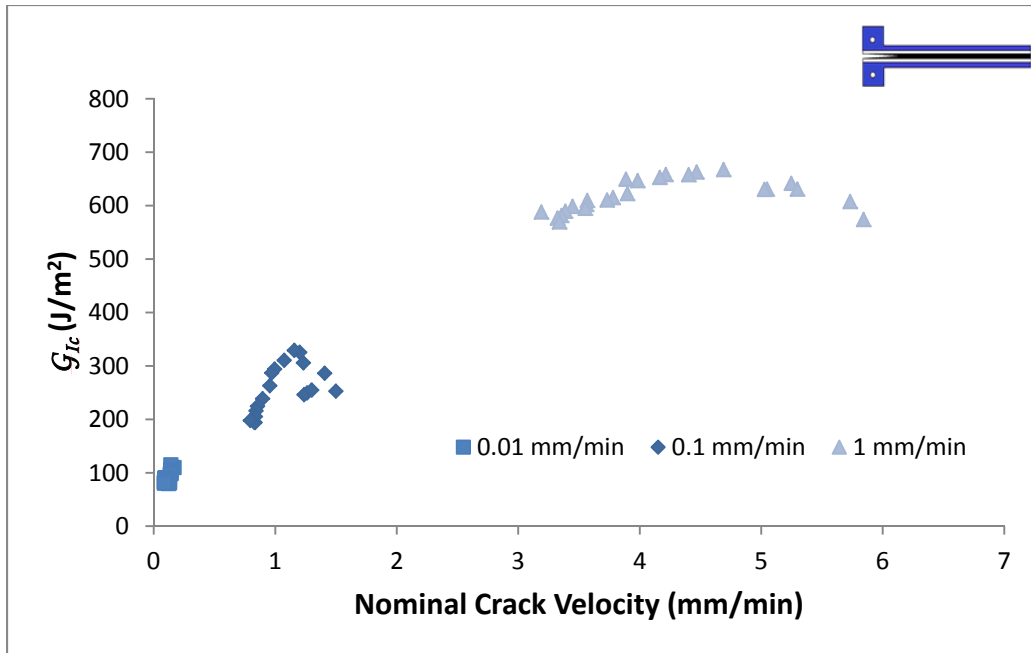
Figure 3.10. Failure surfaces of Al-DCBs printed in the a) $\bar{x}yz$, b) $\bar{x}zy$, c) $\bar{y}xz$, d) $\bar{y}zx$ orientation.

Rate Dependency

To evaluate the rate dependency of the TB/VW interface, additional mode I tests were performed on the AI-DCB configuration at crosshead displacement rates of 0.01, 0.1 and 1 mm/min using AM sandwiches printed in the $\bar{x}yz$ orientation. The results are shown in Figure 3.11.



a)



b)

Figure 3.11. Fracture results for AM sandwich printed in the $\bar{x}\bar{y}\bar{z}$ orientation and tested at three crosshead displacement rates: a) G_{Ic} vs. crack length and b) G_{Ic} vs. crack velocity showing clear crack velocity dependence.

The dramatic differences in fracture energies seen in Figure 3.11a for the three different crosshead speeds, along with the general downward trends in fracture energy seen for most results herein, come into focus when fracture energy is plotted as a function of the nominal crack velocity, as shown in Figure 3.11b. The nominal crack velocity is determined using simple beam theory, which infers a crack velocity based on the known crosshead rate, the crack length, and the assumption that the fracture energy is approximately constant. Essentially, at a constant crosshead rate, the crack grows more rapidly for smaller values of crack length, and then slows as the crack grows. (This is a known artifact for flat DCB tests conducted at constant displacement rates, though is not the case for TDCB specimens.) It is clearly shown that the fracture energy of the TB/VW interface is highly rate dependent, as the fracture energy is seen to increase with

increasing displacement rate. This is believed to result in the downward trends seen for most of the relevant figures in the paper, for all constant thickness specimens. (The TDCB results in Figure 3.5 shows less evidence of this, as would be expected for the more consistent crack propagation rate in this configuration when tested at constant crosshead displacement rate.) The resulting failure surfaces are also dependent on displacement rate and are shown on Figure 3.12.

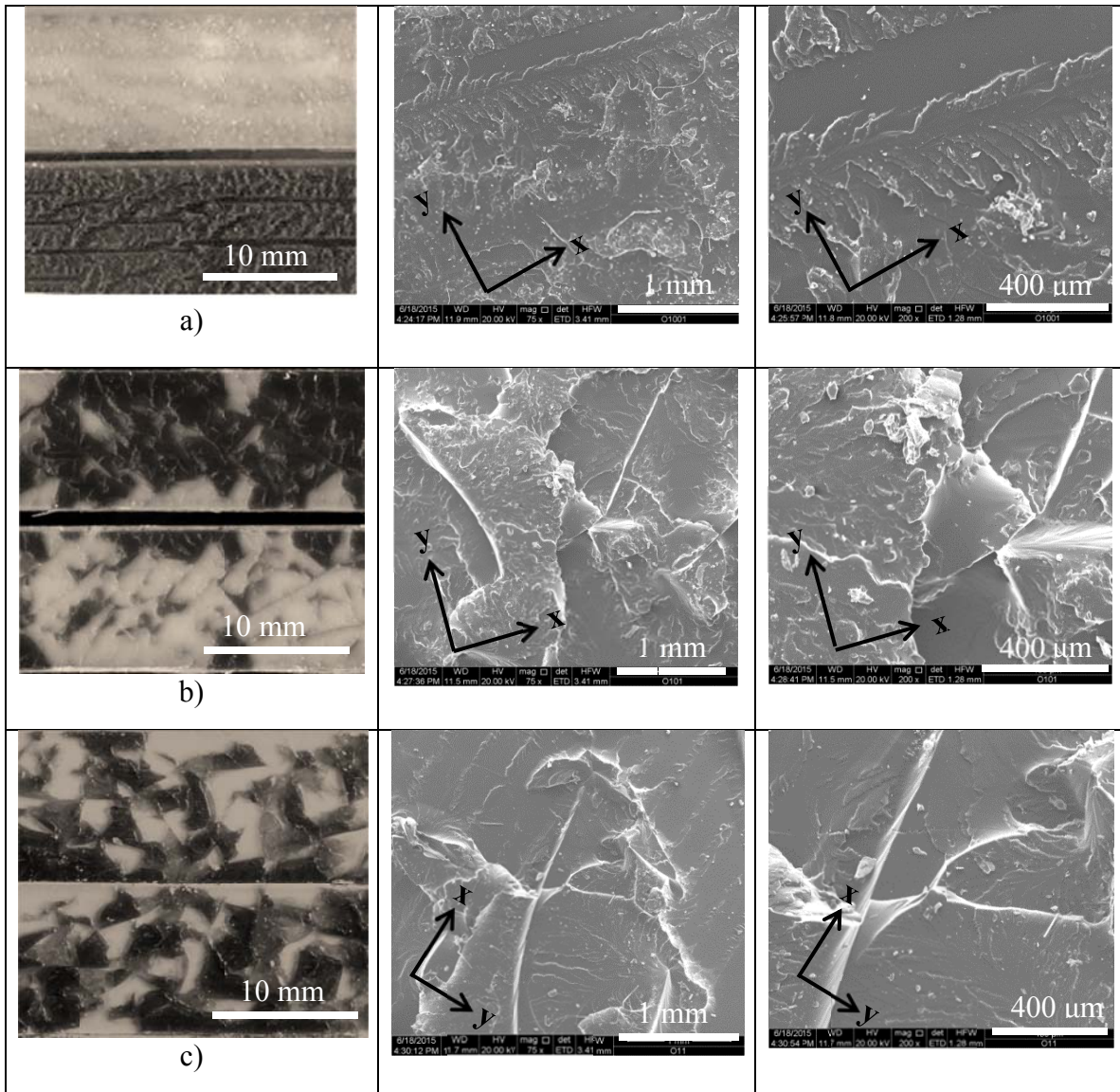


Figure 3.12. Fracture surface of Al-DCB printed in the $\bar{x}\bar{y}\bar{z}$ orientation at the displacement rate of a) 0.01 mm/min, b) 0.1 mm/min, and c) 1 mm/min

For the lowest displacement rate of 0.01 mm/min, the failure surface appears largely interfacial along a single interface to the naked eye. Features are indicative of time dependent flow and have characteristics that appear in highly viscoelastic failures. As the displacement rate increases, the failure of the TB/VW interface remains interfacial, with larger amounts of TB fragments or islands are scattered across both adherend surfaces. Such differences to crack propagation and crack path selection was seen in the work of

Chen et al., where they observed the effects of T-stress for symmetric DCBs tested in both quasi-static and low-speed impact conditions [73]. They demonstrated that DCBs with positive T-stress levels had a locus of failure that was dependent on the rate of crack propagation, where interfacial failures were seen under quasi-static rates and cohesive failures alternating between the adherends were seen for the low impact rates [73]. This was consistent with the earlier findings of Fleck et al., who demonstrated that adhesive layers with a positive T-stress displayed an alternative fracture trajectory [75]. In regards to the current findings above, it is speculated that the TB/VW interface may also have a positive level of T-stress [75] and similar results to Chen et al. [73] are observed when testing the materials at higher displacements rates, though further evidence is needed to substantiate this claim.

DCB and TDCB summary

Figure 3.13 provides a summary of fracture energies measured for all DCB specimens considered in this study. It is demonstrated that each specimen demonstrates significantly different fracture energy values along with variations in the loci of failure. The size of the error bars are representative of the decreasing trend of fracture energy associated with the rate dependency of the interface. While it is seen that the FP-DCB printed in the $\bar{x}z\bar{y}$ orientation are observed to have higher fracture resistance, this was not demonstrated for the AI-DCB. It is predicted that when printing the AM strips on its edge, these specimens result in reduced fracture toughness due to deformations from the roller or possible polymer blending of the TB/VW interface. Despite the variation in data and observations generated in this study, the authors conclude that the AI-DCB is the most accurate specimen that can be used for fracture testing of AM materials because the

TB/VW interface experiences the least amount of adherend dissipation that would distort the calculated fracture energies in comparison to the fully-printed variety. This configuration also requires the least amount of printing material to fabricate, though actual specimen preparation is much longer than the other configurations. However, more research is necessary to probe the potential manufacturing problems associated with printing the AM sandwich in the $\vec{x}zy$ orientation. Other print orientations were not printed and tested for the St-DCB and TDCB due to larger amount of resources required for fabrication.

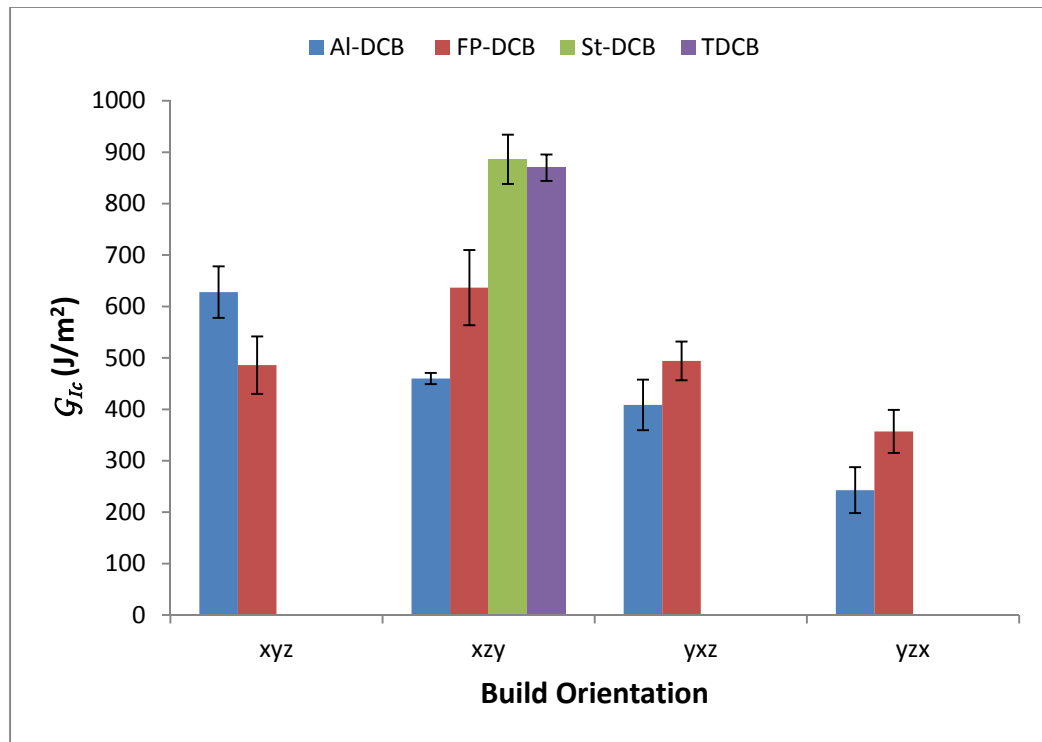


Figure 3.13. Summary of average G_{Ic} for DCB specimens according to print orientation.

One concern in making comparisons of the fracture energy results arose because these values tended to decrease with increasing crack length for all specimens tested, with the exception of the TDCB specimens. Suspecting that these trends resulted from the demonstrated rate dependence of these materials and the known relationship for

decreasing crack propagation speeds for constant cross section specimens tested at constant crosshead displacement rates, the following attempts to address the issue and facilitate more meaningful comparisons. Figure 3.14 conveys plots of averaged crack velocity data plotted as a function of test time on logarithmic scales. Due to the rather erratic data resulting from derivatives of discrete visual observations of difficult to see crack tips, a 7-point moving average was applied to the raw crack velocity data to reduce the experimental variation. A power law fit is then applied to the averaged data of the Al-DCB, FP-DCB, and St-DCB to obtain an equation from which to infer crack velocity. Such fits are analogous to fits used for CBT and experimental compliance method (ECM) analyses of visually observed crack tips. Data from these and other TDCB specimens showed no systematic variation in fracture energy as a function of crack length. If fracture energy were rate dependent, this observation would be consistent with the anticipated constant crack velocity at constant crosshead displacement rate. A zero slope fit is assumed, using the average value as the effective, constant crack velocity for the TDCB specimens here. The apparent G_{Ic} values are plotted in Figure 3.15 against the calculated crack velocities from respective fits of data shown in Figure 3.14. The data for replicate pairs of specimens appears to have collapsed along single lines with relatively consistent slopes.

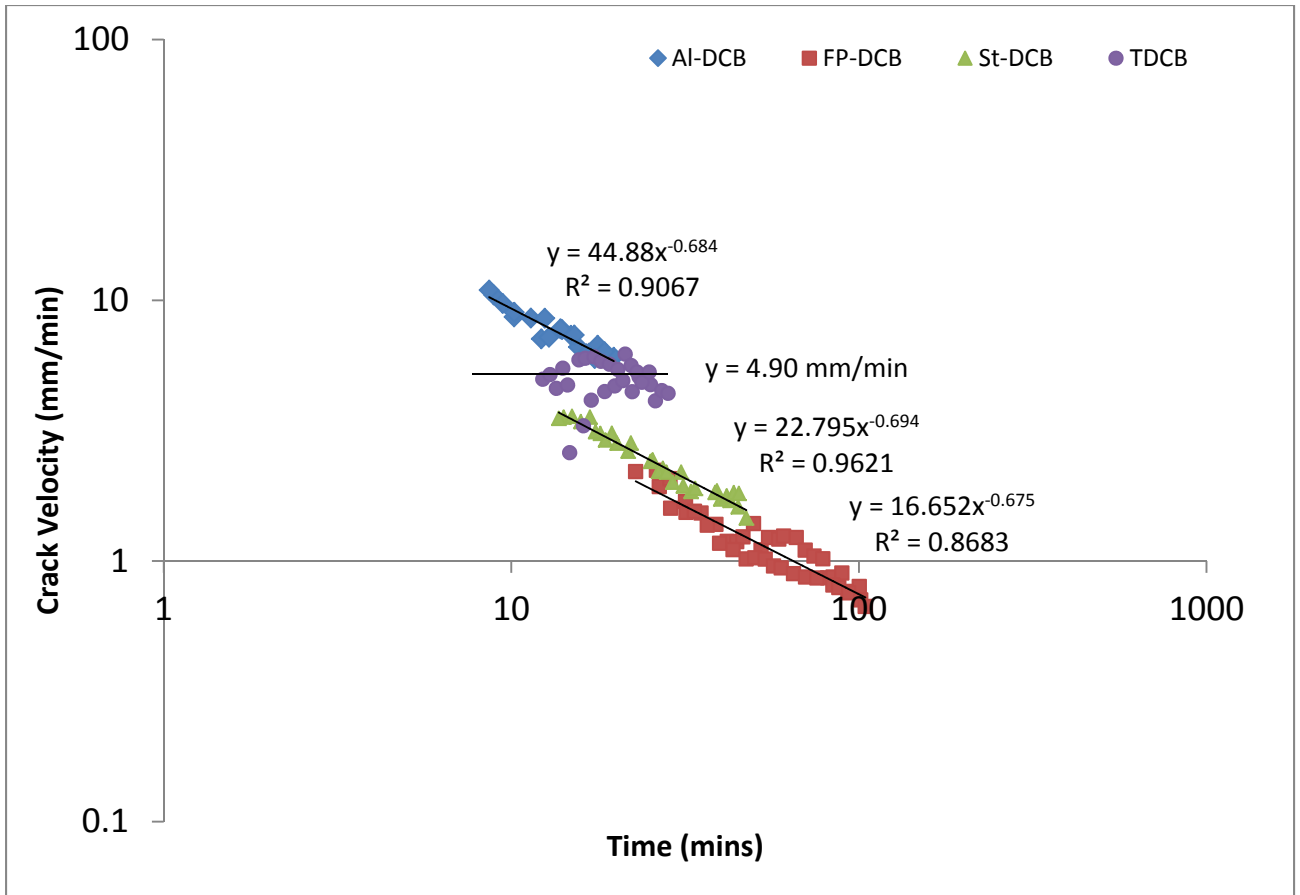


Figure 3.14. Log-log plot of 7-point moving average crack velocity vs. test time for two replicates of specimens printed in the \vec{xzy} orientation.

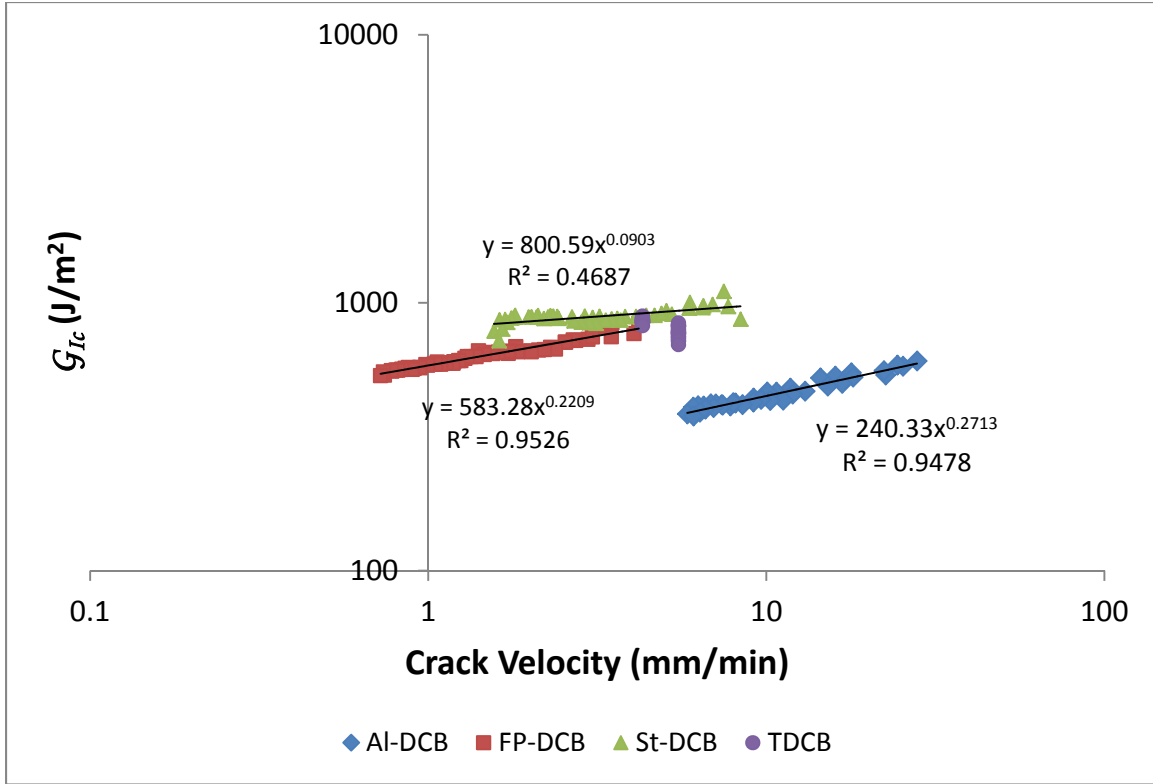


Figure 3.15. Log-log plot of G_{Ic} vs. crack velocity for all $\bar{x}zy$ orientation specimens tested.

Figure 3.15 suggests several key observations. The rate dependence for these $\bar{x}zy$ orientation specimens suggests a relatively consistent time dependence of the form $G_{Ic} = k \cdot \dot{a}^n$, where k and n can be evaluated for each replicate pair. Table 3.2 conveys these values for the cases shown, and the slopes are seen to be relatively consistent for the AI-DCB and FP-DCB, though not for the rather anomalous St-DCB fit. No values are shown for the TDCB specimens, but interestingly, the extrapolation of the FP-DCB fit is quite close to the TDCB cluster, and we note that both types of specimens exhibited a post-failure curvature that disappeared after several days. The AI-DCB fall well below the TDCB, FP-DCB, and St-DCB data (also evident in lower k values). The higher fracture energies for these latter configurations may suggest an exaggeration of measured

fracture energies based on dissipation in these specimens, as noted earlier. There were also some differences in the loci of failure among the specimens, and this could also have affected the measured energies.

Table 3.2. Power law coefficients for Al-DCB, FP-DCB, and St-DCB printed in the $\bar{x}zy$ orientation, yielding $G_{Ic} = k \cdot \dot{a}^n$ in J/m².

	k	n
Al-DCB	240.33	0.27
FP-DCB	583.28	0.22
St-DCB	800.59	0.09

The procedure above was repeated to facilitate comparisons of fracture energies for the four print orientations for both the Al-DCB and FP-DCB specimens. Figure 3.16 conveys a plot of averaged crack velocity data for the two specimens, plotted as a function of test time on logarithmic scales, clearly conveying the consistent drop in velocity with time (and crack length) due to the nature of the test method. Once again, power law fits were applied to the averaged data to obtain an equation from which to infer crack velocity for each print orientation. Fracture energies plotted in Figure 3.17 show more scatter than seen in Figure 3.15, though reasonable power law fits can still be made to the results and slopes are reasonably consistent, suggesting a common time dependence mechanism. The values of k and n are shown in Table 3.3.

The results above demonstrate several key observations of the materials used in this study. Specimens printed in the $\bar{x}zy$ orientation consistently resulted in the highest fracture energies in light of anticipated blending between the deposited materials. When printing in the $\bar{x}yz$ orientation, the Al-DCB unexpectedly demonstrated larger energy dissipation, though the reasons for this behavior are unclear. Printing in the $\bar{y}zx$

orientation are shown to have the lowest fracture energies, and the failure surfaces for both specimen types lack the discretization of TB when compared to the other three orientations. In general, higher fracture energies for FP-DCB configurations may suggest an exaggeration of measured fracture energies based on dissipation of the polymeric adherends.

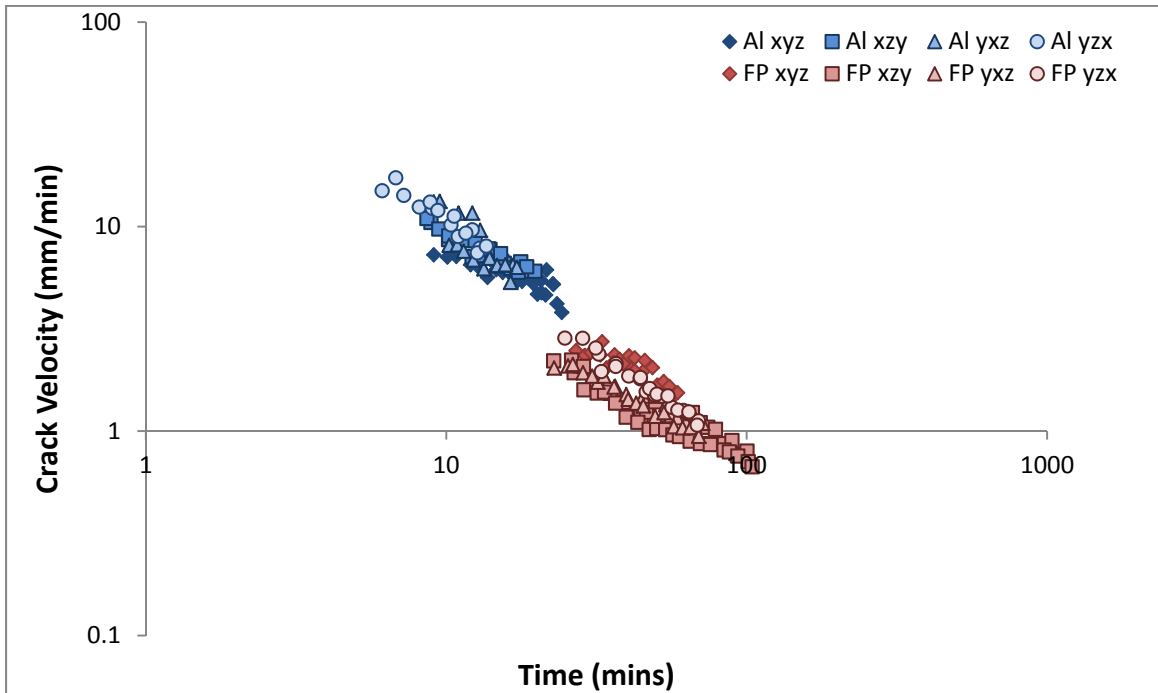


Figure 3.16. Log-log plot of crack velocity vs. time for the Al-DCB and FP-DCB specimens printed in four orientations.

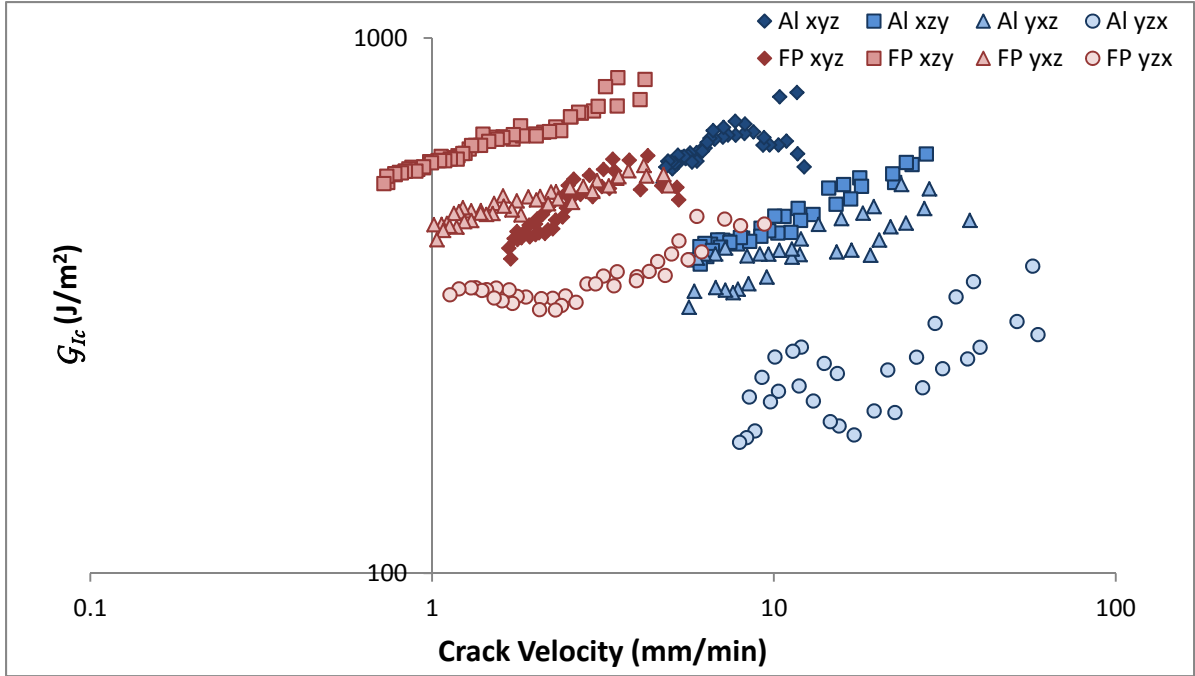


Figure 3.17. Log-log plot of G_{Ic} vs. crack velocity for the Al-DCB and FP-DCB specimens printed in four orientations.

Table 3.3. Power law constants for the Al-DCB and FP-DCB for four print orientations, yielding $G_{Ic} = k \cdot \dot{a}^n$ in J/m^2 .

	Al-DCB		FP-DCB	
	k	n	k	n
$\bar{x}yz$	447	0.18	367	0.29
$\bar{x}zy$	240	0.27	583	0.22
$\bar{y}xz$	245	0.20	446	0.15
$\bar{y}zx$	125	0.22	302	0.16

T-peel specimens and Gradient Architecture

T-peel specimens are a common means to test adhesive bonds, though plastic energy dissipation within the adherends can complicate the analysis. Because of its simplicity, however, attempts to apply this method to the AM strips, as it could offer a useful quality control test if breakage within the adherend arms is not experienced. In addition to the original TB/VW interface, a gradient interface was printed wherein the

central layers transition from VW to TB in the center, and back to VW. Note that in this configuration, VeroGrey60 is also incorporated in addition to TangoBlack60. The test strips were printed in the $\bar{x}yz$ orientation, which had resulted in lower values of fracture energy for the FP-DCB specimens due to the sequential placement of the VW and TG on previously cured layers, though this is the easiest configuration to print. The load traces for the T-peel tests are shown in Figure 3.18.

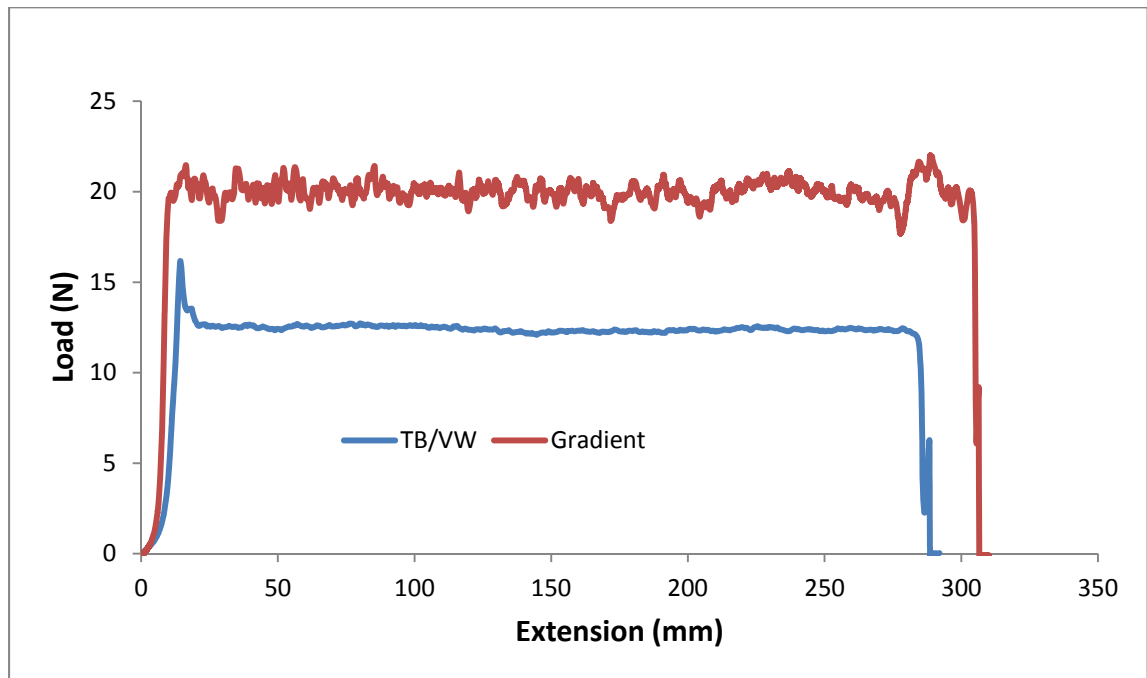


Figure 3.18. Load vs. extension curves from T-peel tests.

Table 3.4. T-peel results

	TB/VW	Gradient
Average Force (N)	12.40	20.08
Apparent Fracture Energy (J/m²)	2505	4057

The TB/VW interlayer configuration is weaker in terms of peel resistance than the specimen produced with a gradient interface. The failure surface shows a pure interfacial failure at the TB/VW interface. While the exact location of failure is not visually clear, the gradient transition had significantly better peel performance, as it shows a 62% increase in average force and apparent fracture energy when compared to pure TB. The apparent fracture energy is calculated from equation 3.6 and has not been corrected for plastic dissipation within the peel arms [76]. The failure surface for the gradient specimen is largely interfacial, where little material is left on one of the adherends as shown in Figure 3.19. Nonetheless, the increased peel resistant for the $\bar{x}yz$ print orientation (weakest orientation for FP-DCB specimens) with gradients suggests the potential benefit of gradient deposition for multi-material components.

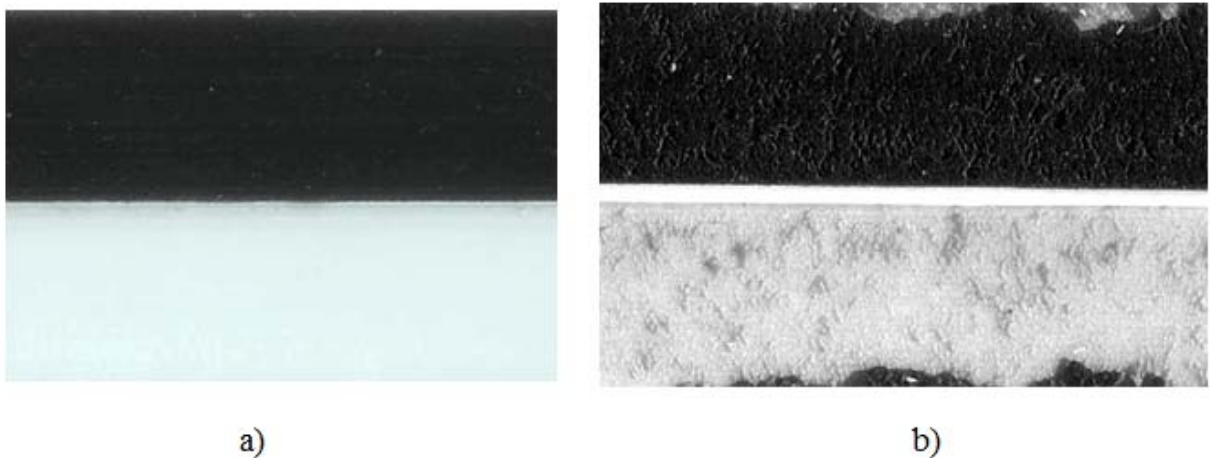


Figure 3.19. Failure surface of T-peel specimens. a) TangoBlack and b) gradient

Conclusions

In an effort to characterize the fracture resistance of PolyJet trilayer systems consisting of a TangoBlackPlus interlayer joining two VeroWhitePlus layers fabricated

using various print build orientations, several fracture mechanics-based test configurations were adapted to assess the mode I fracture energy. Various DCB and TDCB configurations were constructed and tested to establish which specimen configuration would be most appropriate for accurately measuring the fracture energy. Each specimen is shown to have significantly different fracture energy values due to rate dependency and differing amounts of adherend dissipation, but to the naked eye, each configuration has a common grey appearance at the failure surface that may be indicative of polymer blending that occurs when printing in the $\vec{x}zy$ orientation where both TB and VW are deposited simultaneously in a single pass. Other print orientations ($\vec{x}yz$ and $\vec{y}xz$) are explored where the VW and TB are deposited sequentially along the build direction (z-axis). Specimens printed in this fashion are seen to have significantly different failure patterns where distinct patches or tufts of TB are left on the adherend surface, predicted to have occurred along the defects produced by the printing process. Such trends are not seen in the AI-DCB, as the measured fracture energies are seen to be unique to each orientation. Printing the strips at smaller length scales is predicted to lead to reduced fracture energies when printing in the $\vec{x}zy$ and $\vec{y}zx$ orientation, possibly due to distribution of material phases or manufacturing errors from the printer. Regardless of this result, the authors conclude that the AI-DCB is the most representative specimen to be used for fracture characterization of AM materials as this configuration experiences minimal adherend dissipation and requires the least amount of printing material to fabricate.

The fracture energy is seen to be highly rate dependent, as an increase in displacement rate leads to increased fracture energies. Increasing the displacement rate

also leads to failures that transition from purely interfacial to alternating interfacial failures. It is speculated that T-stresses may have developed as a result of cure shrinkage that occurs after printing. For specimens printed in the $\vec{x}zy$ orientation, the rate dependency of fracture energy can be modeled by a power law relationship given by the form $G_{Ic} = k \cdot \dot{a}^n$. This relationship was also applied for the other three print orientations, though larger variations of fracture energy are apparent, even after applying the moving average to the raw crack velocity data.

T-peel tests were performed on the AM test strips and different interface architectures were implemented at the central layers to observe any increased peel performance when compared to the pure TB configuration. It is demonstrated that the gradient pattern had much better peel performance than the TB/VW interface, being 62% higher in terms of both average peel force and apparent fracture energy.

While the viscoelastic nature of PolyJet materials tend to introduce complexities during deformation, it is shown that these materials can offer adequate fracture performance if the proper print parameters are selected. Other combinations of material and pattern architecture not considered in this study may offer other design options for enhanced fracture toughness.

Acknowledgments

The authors would like to thank the Biomedical Engineering and Mechanics (BEAM) Department, the College of Engineering, and the Provost's Office for partial support of IV; the DREAMS Laboratory and the Mechanical Engineering Department for fabricating the specimens tested; and the Macromolecules and Interfaces Institute at

Virginia Tech for fostering interdisciplinary research in polymer science. We also acknowledge adhesives and bonding advice provided by the LORD Corporation.

Chapter 4: Tool-ply friction of composite prepregs using the rheometer

Abstract

Friction in the composite forming process is an important phenomenon that has a strong influence on the quality of composite parts and structures. Interply friction, and friction between the laminate and forming tool, are two mechanisms that contribute to deformations encountered during the forming process. In this study, a commercial rheometer is utilized to evaluate tool-ply friction under a variety of temperatures, contact pressures, and sliding velocities. Friction tests were conducted on dry textile fabrics and composite prepregs, with results indicating different friction and shear phenomenon occurring for the two materials. In addition to Coulomb friction, the resin acts as a lubricant between the rotating plate and prepreg at higher temperature conditions, introducing an interaction of both Coulomb and viscous friction that can be interpreted under the regions of the Stribeck curve.

Keywords

Textile fabric, graphite fiber reinforced prepreg, rheometer, friction, torque, shear stress, tool-ply friction, composite fabrication, Stribeck curve

Introduction

Due to increased awareness of product performance and competition in the global market for lightweight components, composite materials have become widely accepted in a variety of applications where high performance and light weight are desired. Much of the earlier usage of composites can be traced back in the 1950s when the Wright-Patterson Air Force Base began conducting investigations on plastics embedded with

glass fibers and other related materials that would meet the increasing demand for higher performance aircraft [77]. Composites such as continuous S-Glass fibers and epoxy were eventually developed and introduced as the result of a collaboration with Owens-Corning Fiberglass and Union Carbide [77]. It was later in the 1960s when agencies such as NASA sought other composite variations, such as oriented carbon or graphite fibers, that became preferred over glass fibers due to their low density, high stiffness, and superior strength [77]. Now widely employed or considered in aircraft, marine, automotive, and consumer products, composites offer other beneficial material properties that include corrosion resistance, low electrical and thermal conductivity, superior fatigue life, and vibration dampening. The cost of tooling required for fabricating composites is much lower than metals because of lower pressure and temperature requirements, which provides greater flexibility for design changes [78]. Greater design freedom is available by tailoring material properties to meet performance specifications, which can be achieved by changing the fiber type, fiber orientation, and resin system. However, the use of composite materials is limited to applications where the weight penalty is large enough to justify the use of more expensive, yet light weight material. The mechanical properties of fiber reinforced composites are limited to the polymer matrix, as average composites work in the temperature range of -40 to 100°C , but service temperatures greater than 200°C can be achieved with high temperature plastics such as bismaleimides and PEEK [78]. The polymer matrix is also susceptible to solvent and moisture infiltration, which directly affect dimensional stability [78] or induce damage [79].

In the recent decade, composite production processes have been automated to achieve higher production rates with consistent product quality. In regards to

thermoplastic composites, processes such as match-die pressing, hot diaphragm forming, autoclave/vacuum forming, and rubber pad pressing are available to create composite structures of a desired geometry [37-39]. Each forming method is unique in terms of cost and quality of the finished structure, but a common issue that links these processes is the presence of friction between subsequent plies, or between the tool and laminate. Friction during the forming process is particularly undesirable as it causes residual stresses and shape distortions such as wrinkling and thickness variations in the laminate [4, 42, 80]. The level of frictional contact is known to be a complex function of the forming process parameters such as temperature, pressure, and sliding velocity. Martin et al. conducted some of the earlier investigations of friction in composite forming, demonstrating that friction was dependent on both resin viscosity and distribution [44]. Systems with high fiber volume fraction showed higher frictional resistance due to mechanical interlocking of the fibers as the resin softened at higher temperatures [44]. Ersoy et al. would later reveal increases of interply friction at higher temperatures up to the vitrification point of the resin [45, 46]. They also demonstrated that the layup of the laminate has a considerable effect on tool-ply friction, indicating that the presence of 90° plies increased the interfacial shear stresses and reduces stress relaxation due to increased mechanical interlocking of the fibers [45]. Thijs et al. extensively studied tool-ply interaction in thermoplastic composite forming, where they developed a model based on Reynolds' equation that accounted for the rheological properties of the matrix material and the geometry of the fabric weave [8]. The model demonstrates that typical trends within the hydrodynamic regime of the Stribeck curve, indicating that the coefficient of friction

increases when the velocity increases, but decreases when the temperature and normal pressure increase [5, 8].

As indicated in the benchmark study of Sachs et al., frictional measurements of composites exhibit high variability due to design differences between various test instruments and approaches used [3]. The differences between experimental apparatuses are attributed to the accommodation of different specimen sizes, as well as the ability to maintain uniform temperature and pressure distribution over the contact area. While the majority of friction test instruments are entirely tribological by design [3, 44, 45, 81], very few instruments are capable of characterizing friction in the scope of both tribology and rheology, as both are necessary to characterize the frictional effects of composite forming [6, 82]. In this study, a modified torsional rheometer based on the design of Kavehpour et al. [6] is used to evaluate tool-ply friction of the composite forming process, as the fixture has the capability to capture tribological and bulk rheological properties of the polymer matrix under shear. The main advantage of the rheometer lies in the broader range of shearing rates that can be achieved in contrast to traditional pull-out and pull-through methods and greater temperature control can be obtained by its smaller environmental chamber [83, 84]. In its current configuration, the instrument is not able to account for the anisotropy of the fabric weave as the upper plate rotates across the warp and weft directions of the fabric, effectively providing an average coefficient of friction. Nonetheless, the rheometer is predicted to be a useful tool that may provide characterization of the prepreg's frictional response to manufacturing variation.

Experimental Methods

Frictional Measurements

The measurement of sliding friction using the rheometer is an approach that has been utilized by a number of researchers [6, 83-85], as the rheometer is particularly attractive for its control of temperature, pressure, and sliding velocity between the upper rotating plate and sample of interest. In this study, a standard torsional rheometer (Anton Parr MCR 302) with a parallel plate configuration is modified in order to obtain frictional measurements.



Figure 4.1. Anton Parr MCR 302 rheometer

The parallel plate configuration consist of two flat circular plates: one stationary plate at the bottom of the instrument, while the upper plate rotates under user specified inputs. One characteristic of the parallel plate configuration is that the sliding velocity is not constant as it varies linearly with the radius. To minimize radial variations of velocity, the upper rotating plate is machined to create a raised annulus plate. Three

annulus plates, made of 6061-T6 aluminum, are used to enable variation of annulus width, as shown in Figure 4.2. Note that the flat base plate also has a radius of 12.5 mm.

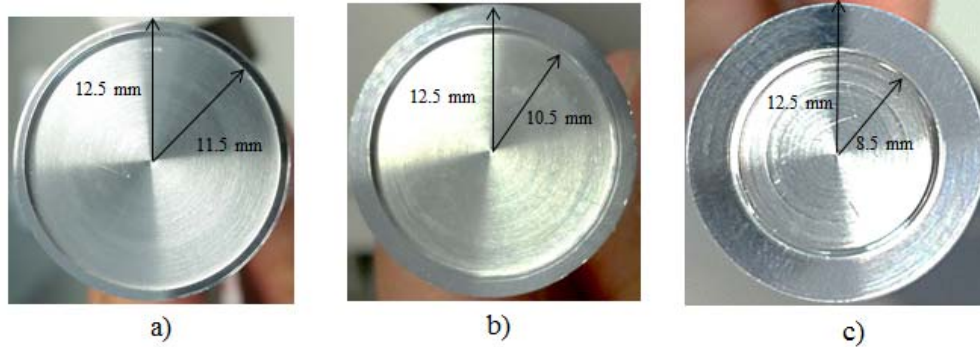


Figure 4.2. Three annulus geometries. a) 1 mm, b) 2 mm, and c) 4 mm

Couched in the framework of an effective coefficient of friction over a range of Coulomb and viscous contributions for the rheometer and annulus geometry, the torque is given by [85]:

$$T = 2\pi\mu P \int_{R_1}^{R_2} r^2 dr \quad (4.1)$$

where μ is the effective coefficient of friction (COF), P is the normal pressure, and R_2 and R_1 are the outer and inner radii of the annulus, respectively. Equation 4.1 is presented under the assumption that both pressure and COF are constant and can be taken outside of the integral. By integrating with respect to r , the torque equation is then given by:

$$T = \frac{2}{3} \pi \mu P (R_2^3 - R_1^3) \quad (4.2)$$

Under the assumption of uniform contact pressure, the normal force N can be defined by:

$$N = P\pi(R_2^2 - R_1^2) \quad (4.3)$$

By substituting equation 4.3 into 4.2 and rearranging, the coefficient of friction μ is defined by the equation below:

$$\mu = \frac{3T(R_2^2 - R_1^2)}{2N(R_2^3 - R_1^3)} \quad (4.4)$$

Specimen Preparation and Materials

Preliminary tests were conducted on dry textile fabric to ensure reliable friction measurements can be collected from the rheometer. While these tests are performed as a validation of friction measurements, such tests can provide insight into the Coulomb friction mechanisms of fibers prior to resin transfer molding where resin is injected into the dry reinforcement prior to lamination [86]. The materials used for preliminary friction testing consist of two sets of dry textile fabrics: a plain weave carbon fiber fabric (Carr Reinforcement DW0164) and twill weave glass fiber fabric (PD-Interglas 92125 UD). A double sided pressure sensitive adhesive (PSA) is applied to the back of a sheet of both materials to maintain fiber stability and orientation prior to cutting samples.

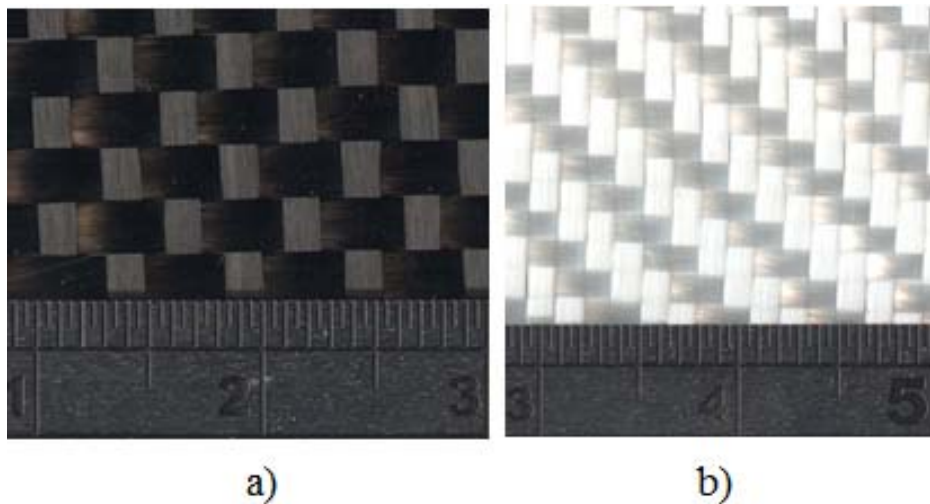


Figure 4.3. Dry fabric materials. a) Carr Reinforcement DW0164 plain weave carbon fiber and b) PD-Interglas 92125 UD twill weave glass fiber

As the base plate of the rheometer has an approximate diameter of 25 mm, squares of 32 x 32 mm were cut from the taped fabrics to minimize the presence of edge effects that may potentially distort measurements. The samples were attached onto the base plate using the double sided PSA. The table below lists the range of normal forces, contact area, and rotational sliding velocities used to perform the friction tests. Each test is performed at a constant temperature of 20°C and until a 100 mrad, or 5.73° rotation is achieved. A single sample of each material was reused to conduct tests under the possible combinations of test parameters given in Table 4.1.

Table 4.1. Test parameters for friction testing of textile fabric (for carbon and glass fiber).

Annulus Width (mm)	1	2	4
Normal Force (N)	10	15	20
Rotational Sliding Velocity (mrad/sec)	1	10	100

The composite prepreg used for this study is the Cytec MTM49/CF5700, a twill weave carbon fiber fabric with an epoxy resin. Following the procedure outlined above, double sided PSA was applied to the back of the prepreg sheet and cut into 38 x 38 mm squares. The 1 mm annulus is only used for these tests as this annulus has the lowest radial variations of velocity and was able to be tested within the torque limits of the rheometer. The other annulus geometries (2 and 4 mm) exceeded the torque limits, even at small axial loads. Temperature variation is introduced to evaluate any temperature dependencies that may arise from the resin. Each test is conducted until a 1571 mrad or 90° rotation is achieved. Table 4.2 outlines the range of normal forces, sliding velocities, and temperatures utilized for the tests. It is noted that a virgin specimen is used for each

test and each sample was set into the chamber and left for 5 minutes to allow them to equilibrate at the desired test temperature before testing began.

Table 4.2. Test parameters for friction testing of Cytec MTM49/CF5700.

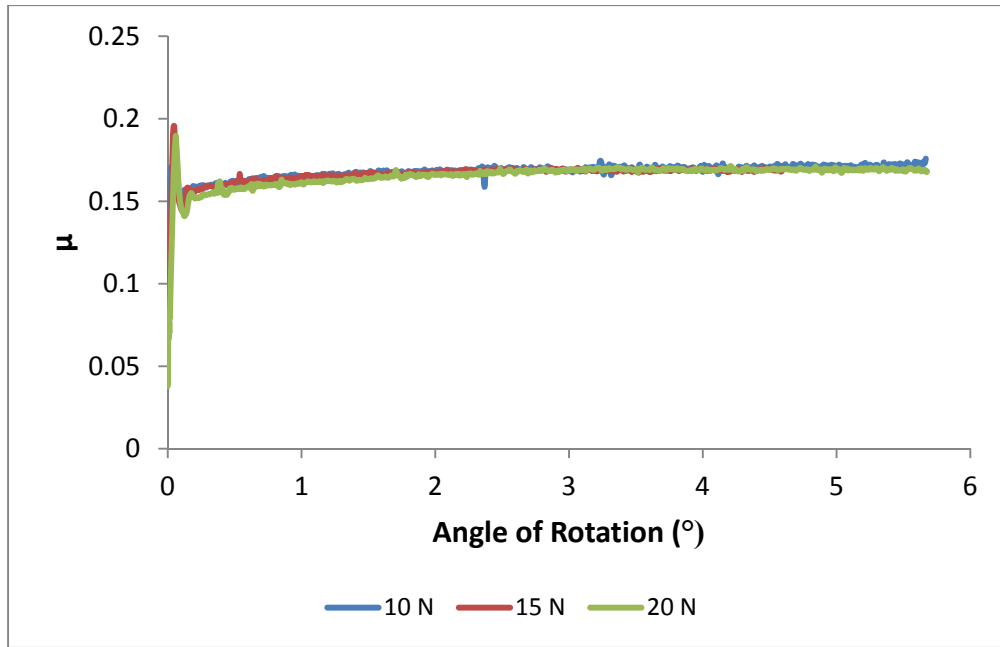
Temperature (°C)	20	30	40	50
Rotational Sliding Velocity (mrad/sec)	5	10		15
Normal Force (N)	5	10		15

The test program created for friction testing is split into two phases: the first phase consists of a 30 second interval during which the rotating plate is lowered onto the sample until the target normal force is reached and the second phase initiates sliding between the contacting surfaces based on the user’s input of sliding velocity and total angle of rotation.

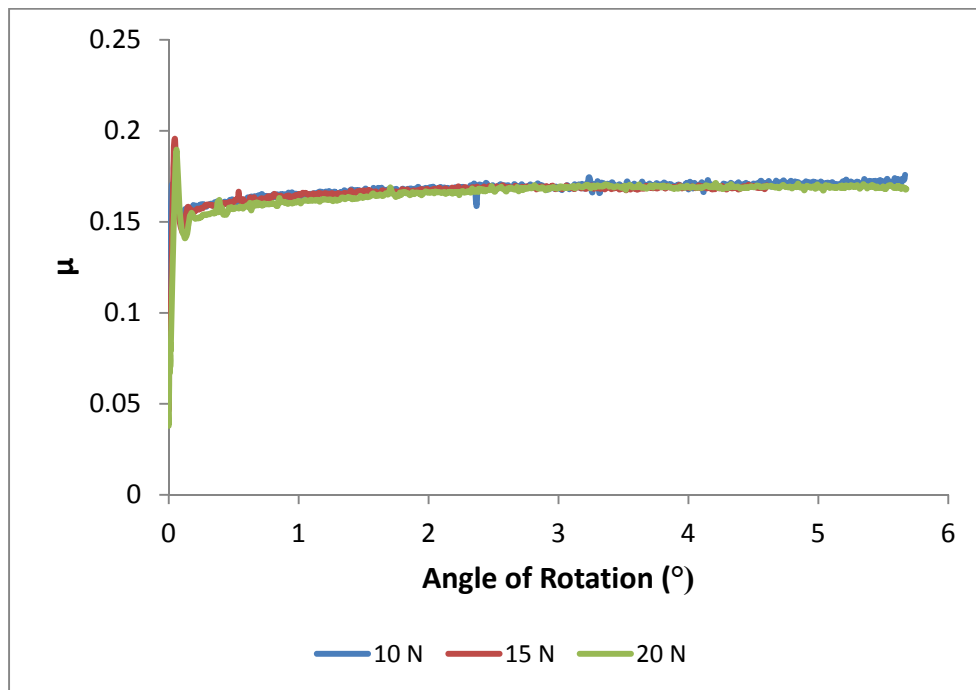
Results

Preliminary Tests – Textile Fabrics

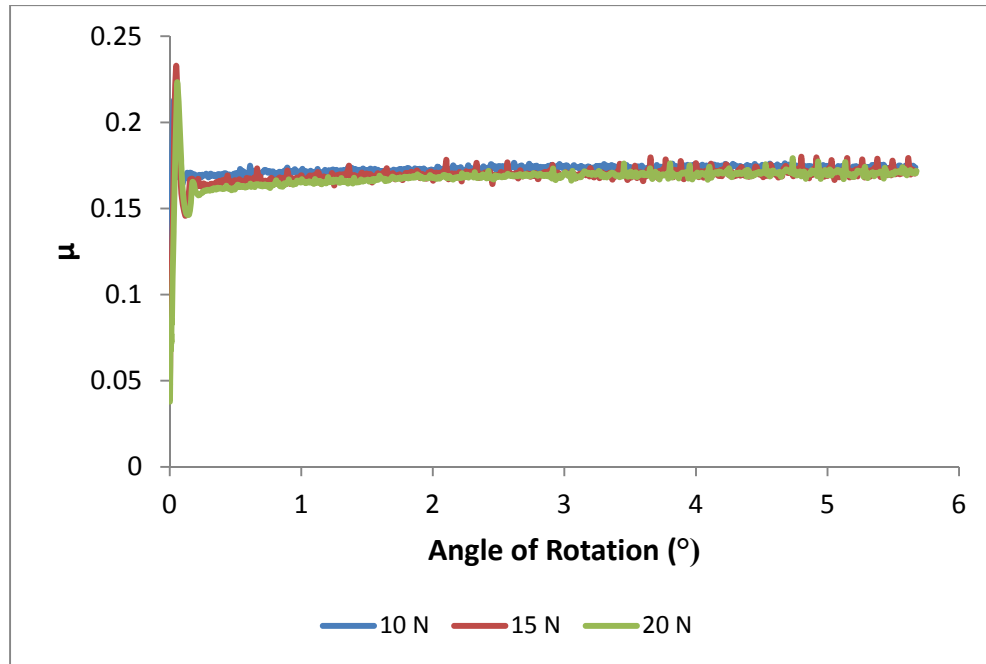
Frictional measurements were collected from the textile fabric samples under a range of normal forces and sliding velocities listed in Table 4.1. All tests conducted on the fabrics were performed at a constant temperature of 20°C. Slippage of the fabric/PSA interface was not observed during testing. Representative friction curves for the carbon fiber and glass fiber are shown in Figure 4.4 and Figure 4.5, respectively.



a)

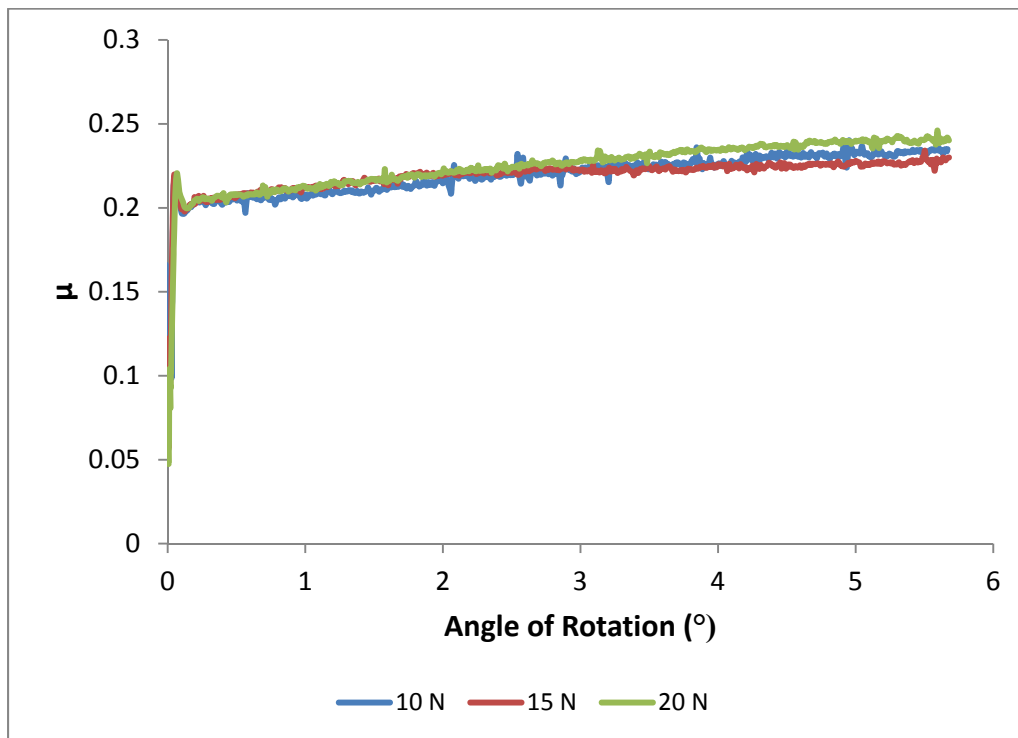


b)

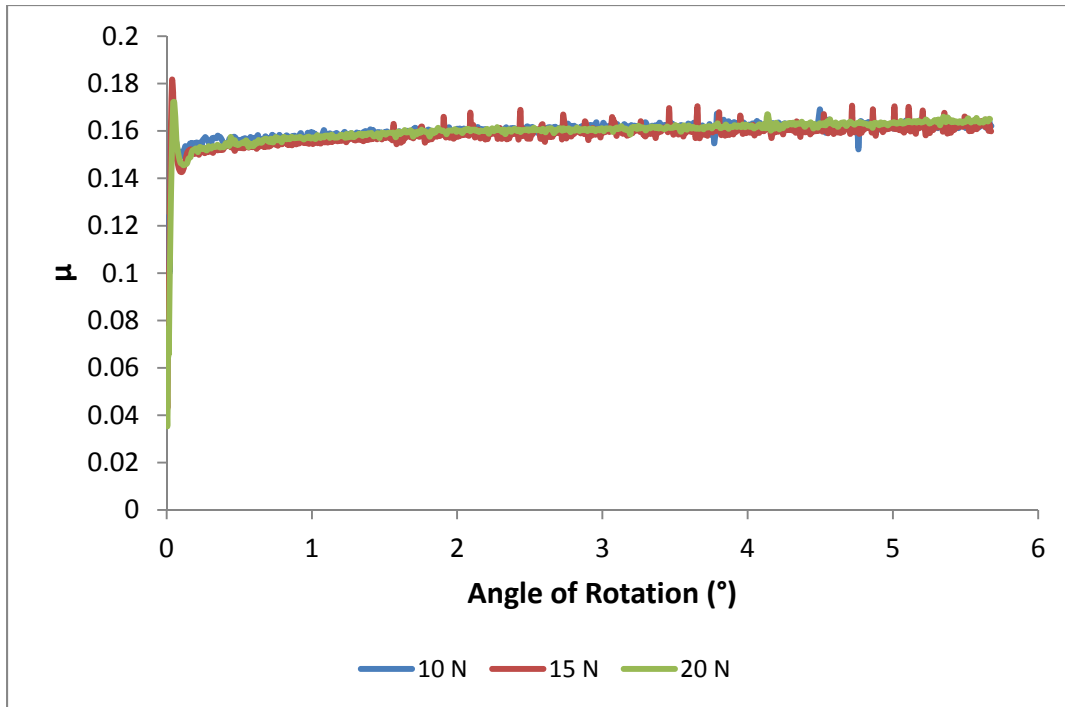


c)

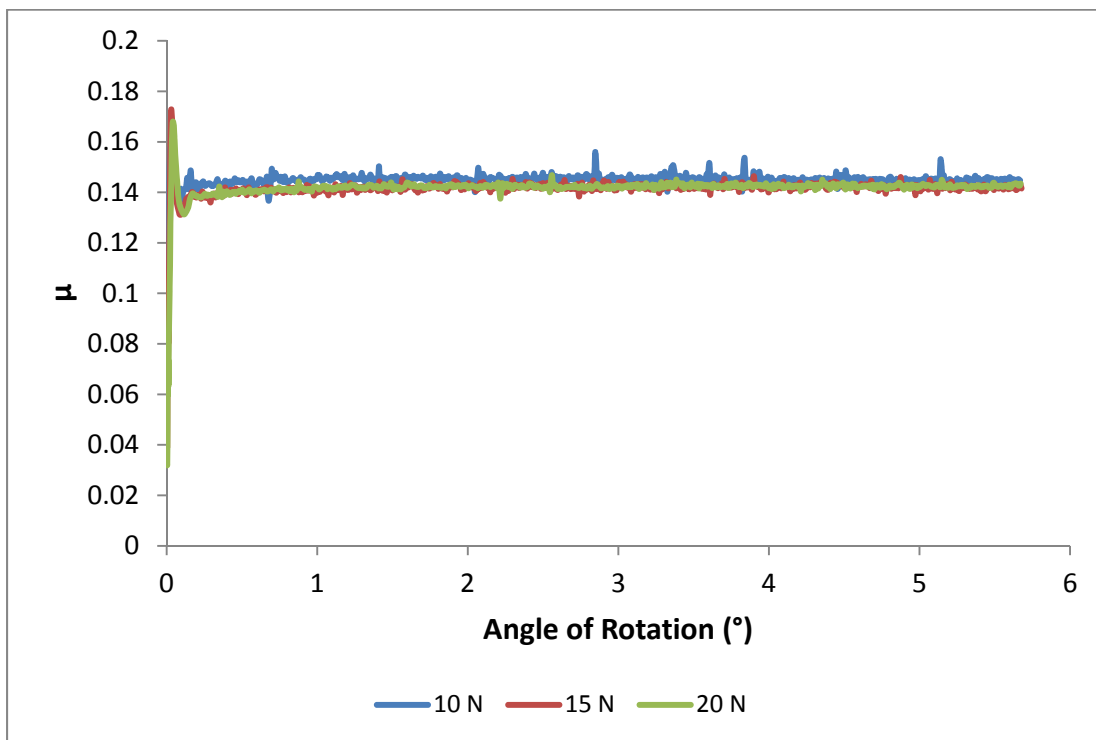
Figure 4.4. Calculated coefficient of friction (μ) against angle of rotation for carbon fiber fabric at a) 1 mm, b) 2 mm, and c) 4 mm annulus (rotational sliding velocity – 100 mrad/sec)



a)



b)



c)

Figure 4.5. Calculated coefficient of friction (μ) against angle of rotation for glass fiber fabric at a) 1 mm, b) 2 mm, and c) 4 mm annulus (rotational sliding velocity – 100 mrad/sec)

The curves have a distinct maximum friction peak that is representative of static friction, while the plateau region represents the region of kinetic friction. It is demonstrated that the frictional processes on the carbon fiber are primarily Coulomb-dominated, as both the static and kinetic coefficients of friction are independent of the contact pressure and velocity as shown in Figure 4.6 and

Figure 4.7.

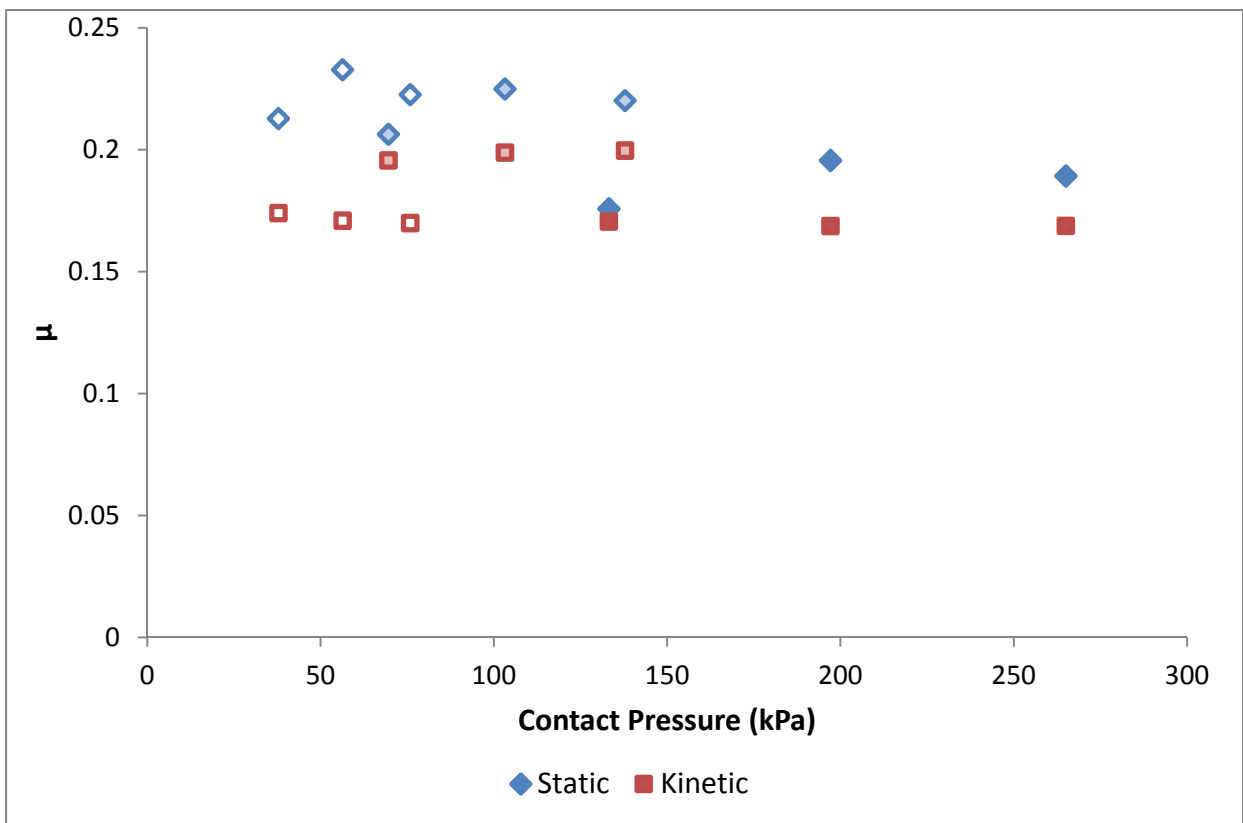


Figure 4.6. Calculated coefficient of friction (μ) against contact pressure for carbon fiber fabric at a rotational sliding velocity of 100 mrad/sec. (open symbols – 4 mm annulus, lightly filled symbols – 2 mm annulus, and filled symbols – 1 mm annulus).

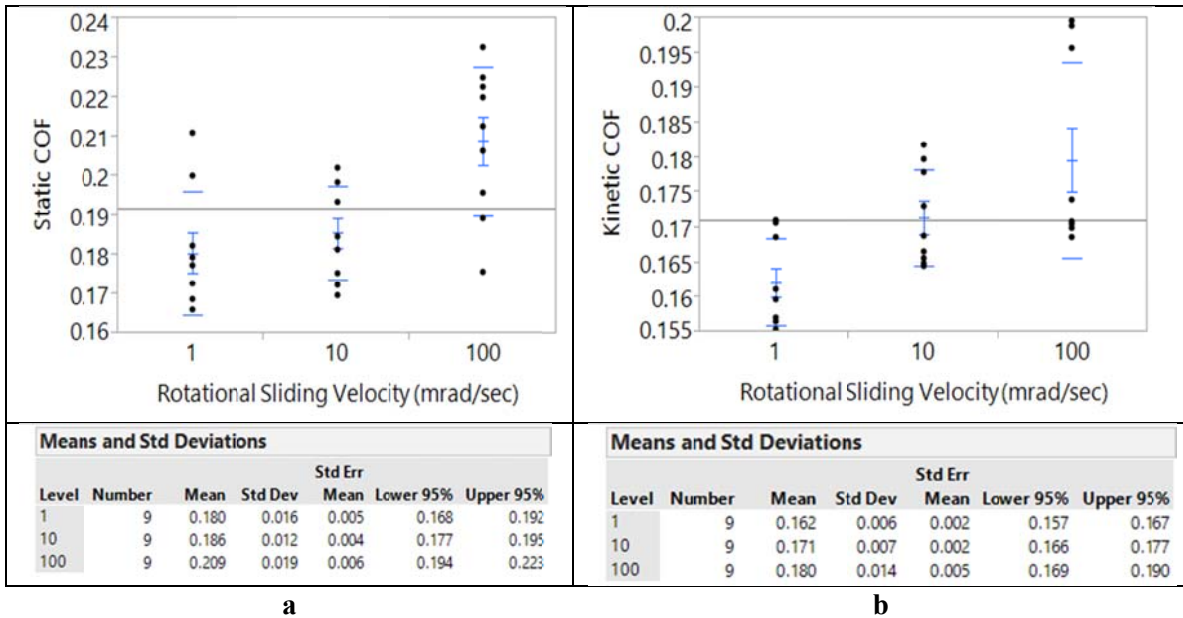


Figure 4.7. Calculated a) static and b) kinetic COF vs. rotational sliding velocity of carbon fiber with means and standard deviations.

Such behavior was not observed in tests of the glass fiber fabric, as there are clear trends of contact pressure dependency, where calculated friction is shown to increase with increasing contact pressure, as demonstrated in Figure 4.8. Such dependencies in the glass fiber fabric could be attributed to the compressibility of the fabric, though other structural characteristics such as yarn crimp, spacing, and crown height are reported to have a significant effect on the frictional characteristics of woven fabrics [87-89]. Ajayi et al. investigated trends of fabric compressibility, indicating that the softer fabrics were subjected to higher values of friction coefficients due to greater out-of-plane compressibility that reorients the fibers, leading to higher contact area and subsequent mechanical interlocking of surface protuberances [88, 89]. It is thought that such behavior is occurring with the glass fiber fabric, as the material is much less axial stiffness than carbon fiber [90]. Twill weave fabrics are generally more mobile, which

may increase the probability of fiber reorientation during testing [91]. As repeated tests were performed on the same sample, it is also possible that abrasion of the material may have occurred as low pressure tests were conducted before the high pressure tests; leading to higher values of friction coefficients at higher contact pressures, though further testing and observation is needed to evaluate this possibility. Figure 4.9 indicates that the glass fiber also has more pronounced velocity dependence, though the reasons behind this behavior are unclear.

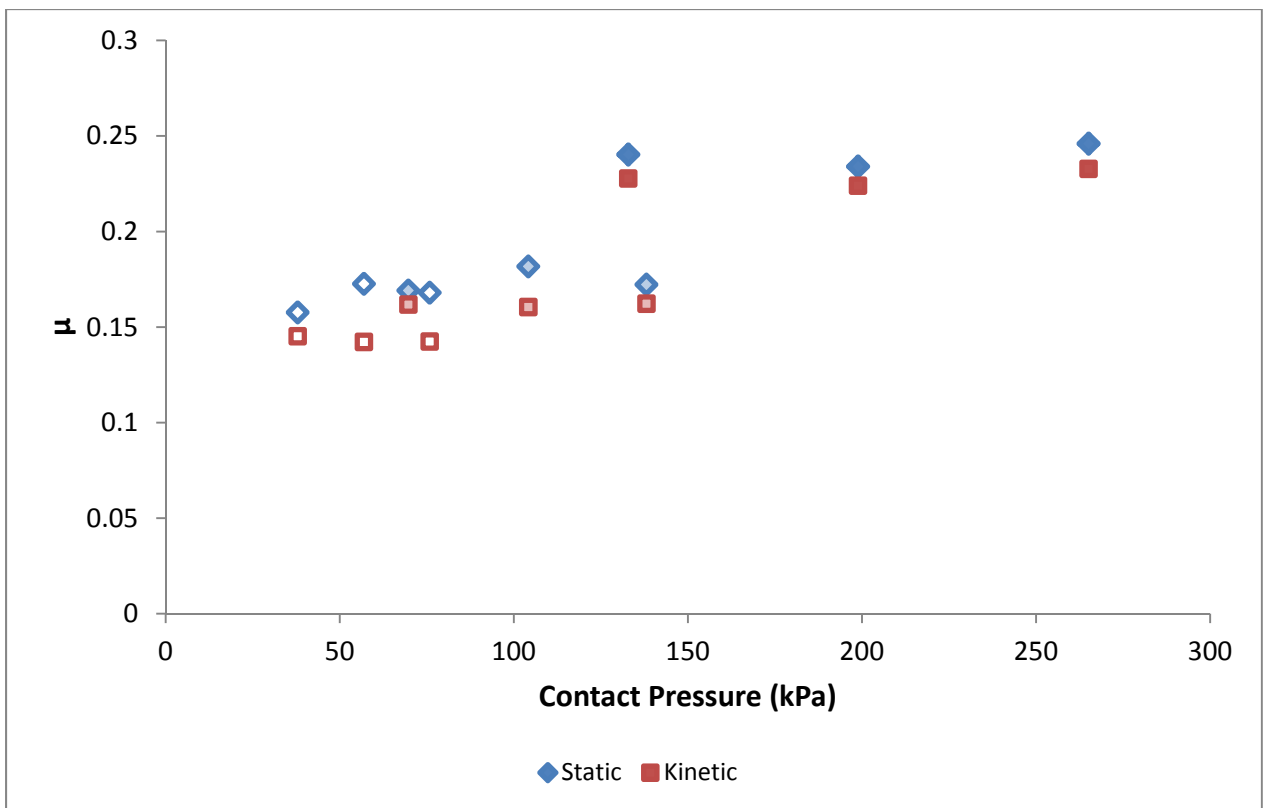


Figure 4.8. Calculated coefficient of friction (μ) against contact pressure for glass fiber fabric at a rotational sliding velocity of 100 mrad/sec. (open symbols – 4 mm annulus, lightly filled symbols – 2 mm annulus, and filled symbols – 1 mm annulus).

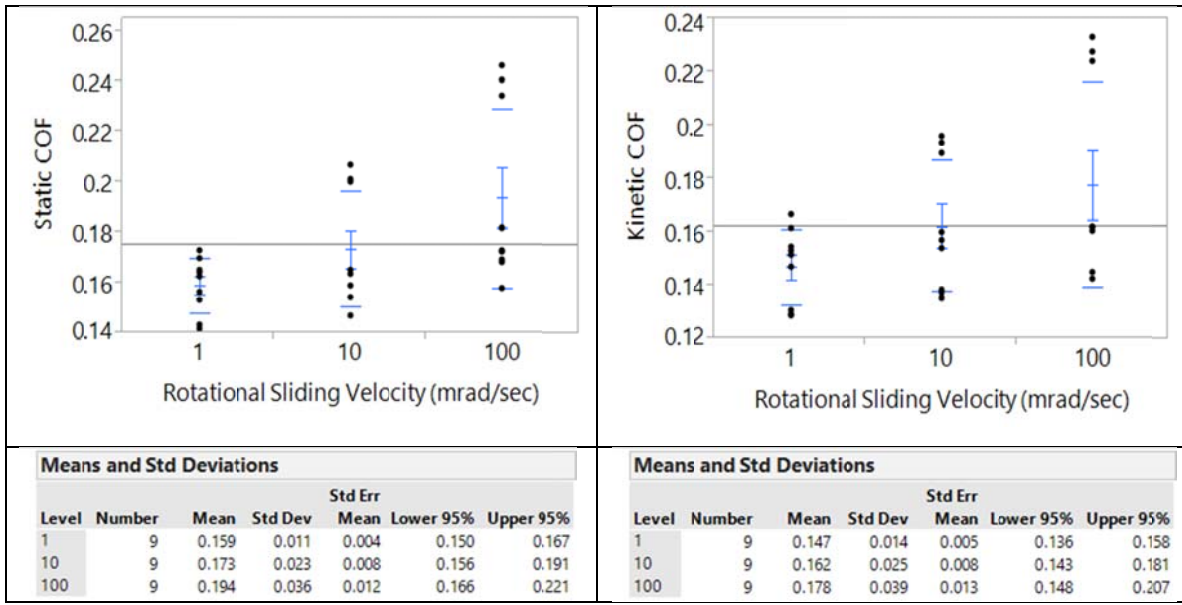


Figure 4.9. Calculated a) static and b) kinetic COF vs. rotational sliding velocity of glass fiber fabric with means and standard deviations.

When the addition of the matrix resin is introduced to the textile fabrics to create composite prepregs, the frictional mechanisms become less clear to explain as a more detailed experiment is required to account for the presence of the resin, especially under high temperature conditions where the prepregs are consolidated to create composite laminates.

Prepreg friction

Data Repeatability

To evaluate the data repeatability of the rheometer on prepregs, seven tests were conducted using the 1 mm annulus, where a new sample was used for each test. A sliding velocity of 10 mrad/sec, temperature of 20°C, and a normal force of 10 N was utilized for all tests. In contrast to the textile fabrics, measurements of the prepregs demonstrate some variability between all samples, especially for the last test where the torque reached a maximum of 170 mN.m.

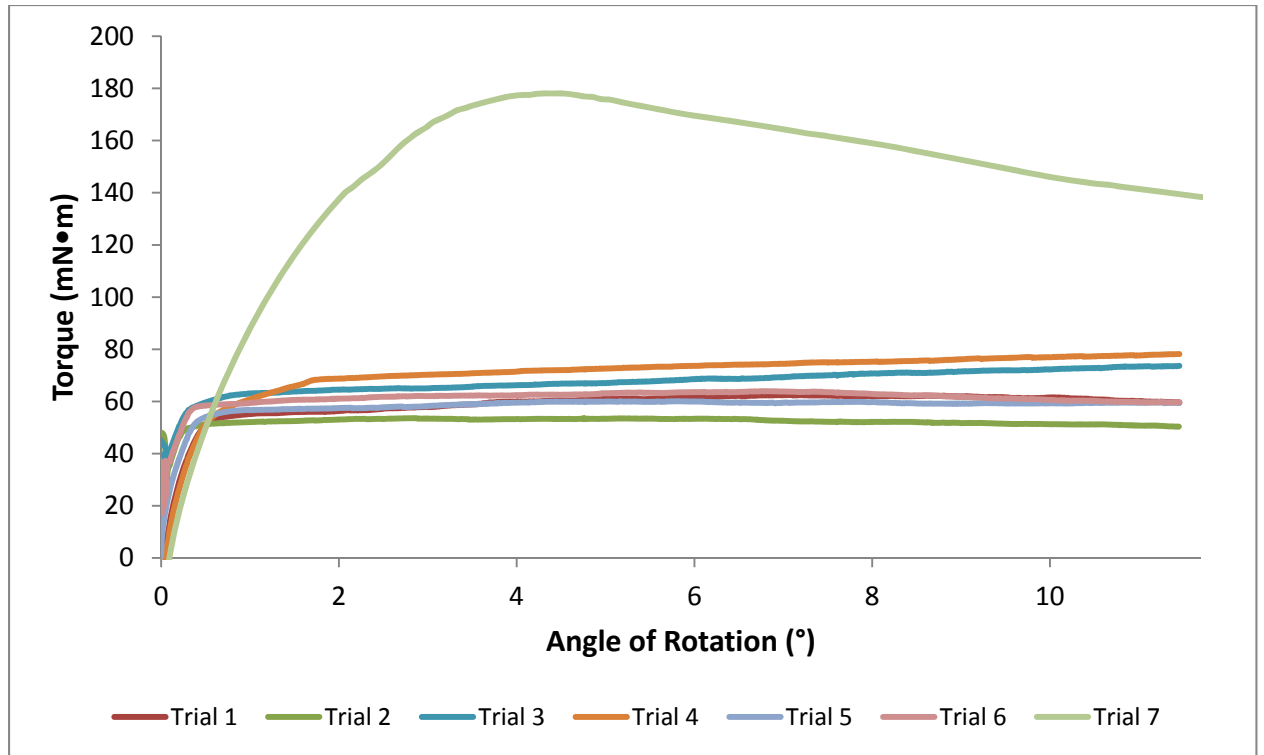


Figure 4.10. Torque vs. angle of rotation for repeated tests performed at 10 N normal force, 10 mrad/sec, and 20°C.

Influence of Temperature

While the frictional processes of the dry textile fabric were dominated by Coulomb friction, the presence of the epoxy resin on preregs introduces additional complexities associated with the viscous nature of the resin. It is predicted that at higher temperatures, the reduced viscosity allows the resin to effectively act as a lubricating film between the tool and prepreg, and shearing of the resin becomes an additional mechanism that contributes to the frictional processes. Sliding of the PSA/base plate interface was not observed during testing. To evaluate the temperature dependency of the prepreg, friction tests were conducted over the ranges of temperature, pressure, and sliding velocity listed in Table 4.2. A new specimen is used for each test to avoid any distortion of measurement associated with redistribution of the resin after each test. The 1 mm

annulus, used for all prepreg tests, was thoroughly cleaned with acetone after each test to avoid redepositing resin onto a new sample. The results of the friction tests at various temperatures are shown in Figure 4.11.

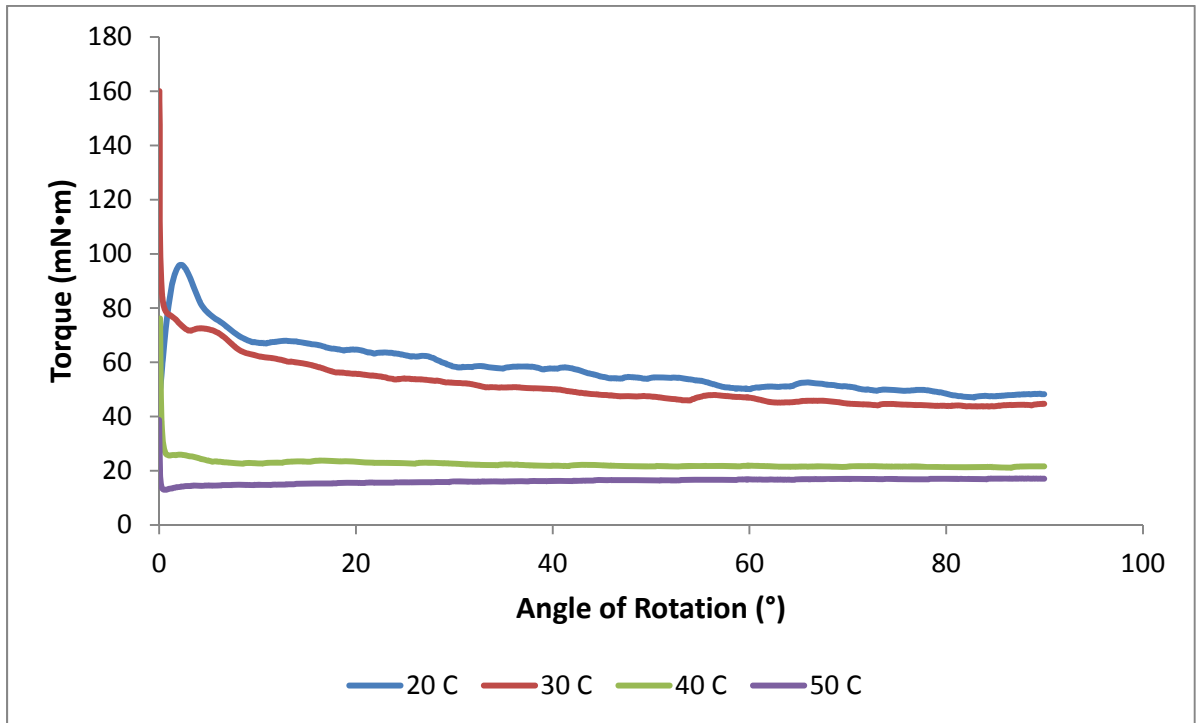


Figure 4.11. Torque vs. angle of rotation at four different temperatures (angular velocity: 10 mrad/sec, normal compressive force: 5 N).

As shown in Figure 4.11, temperature is seen to have a significant effect, as higher temperatures result in lower torque and shear stress acting on the prepreg. This is primarily due to the reduction of the resin viscosity at higher temperatures. At 20°C, the torque plot is shown to exhibit some Coulomb-like friction characteristics, where there is a maximum peak of shear stress followed by a plateau region, which may be indicative of static and kinetic regions of dry Coulomb friction. The peak torque may arise due to an adhesive bond that forms between the rotating plate and resin prior to testing, which must be broken before sliding of the relatively stiff prepreg could occur [92]. The decreasing values of torque at the lower temperatures (20 and 30°C) may be associated with

localized frictional heating occurring at the interface of the annulus and prepreg which causes the resin to become less viscous. At higher temperatures, the maximum torque peak is less noticeable, potentially as a result of cavitation that more easily disrupts the bond formation after contact in less stiff materials, as has been reported for pressure sensitive adhesives [93]. Figure 4.12a also shows additional deformations occurring in the prepreg, showing possible signs of warpage during rotation as a result of higher torque and frictional forces exerted on the prepreg.

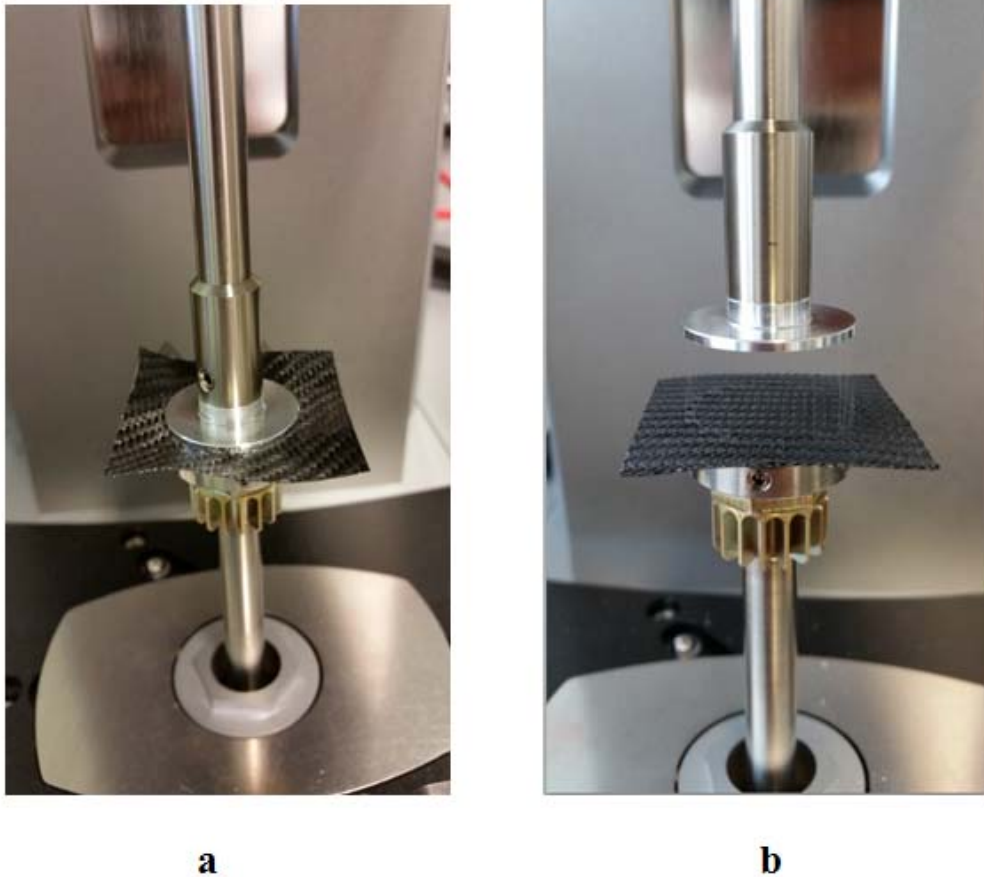


Figure 4.12. Images of prepreg after completing friction tests at a) 20°C and b) 50°C. At 50°C, there is an initial spike of the torque, followed by a rapid fall and gradual increase in torque with increasing angle of rotation. This behavior is likely to be redistribution of the resin during testing as the rheometer continues to decrease the gap

size slightly to maintain the targeted normal force and pressure. Resin is possibly being squeezed out at the interface, leading to mechanical interlocking or abrasion of the fibers during rotation that could subsequently increase the torque and COF.

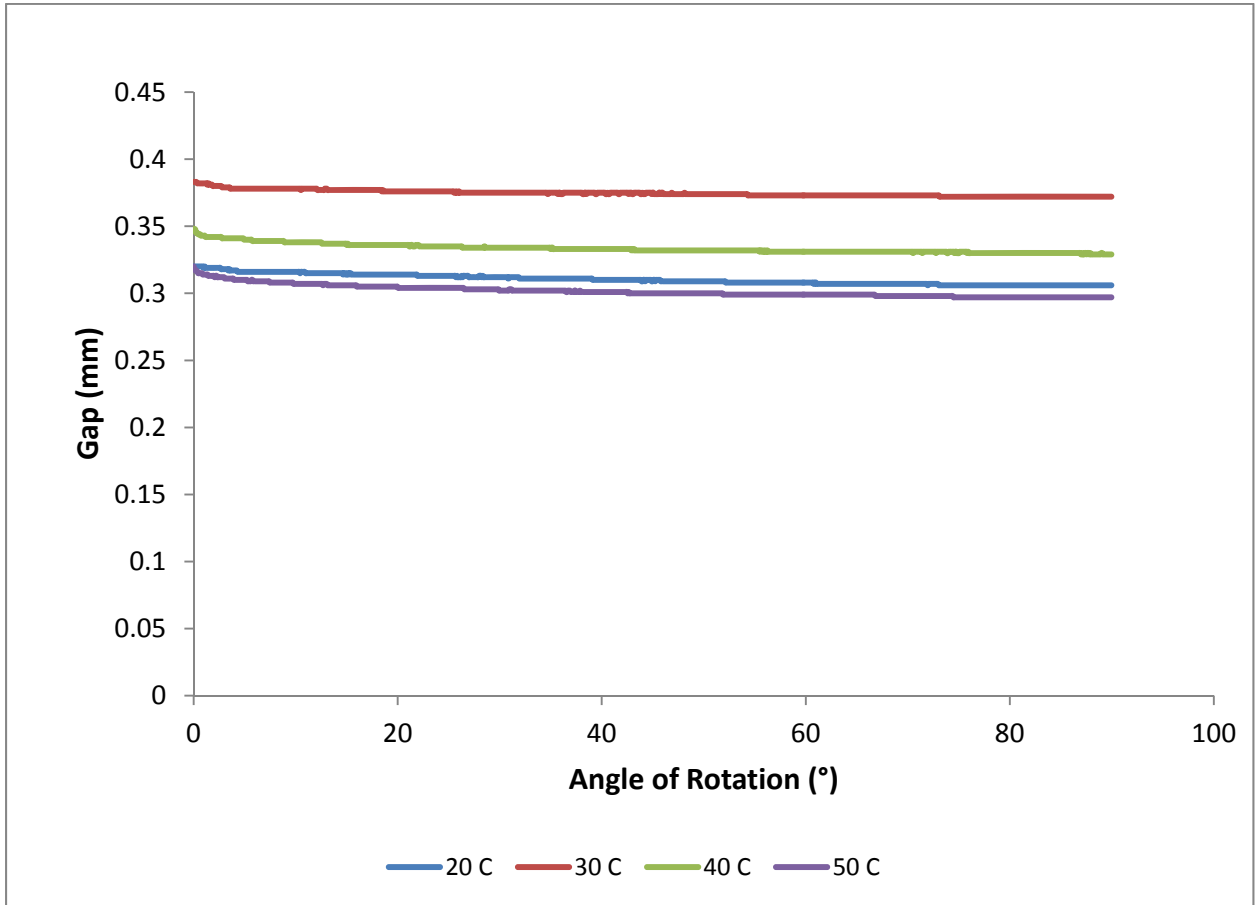


Figure 4.13. Gap size vs. angle of rotation for tests conducted at four different temperatures.

Influence of velocity

To explore rate effects, the angular velocity is adjusted according to Table 4.2 and tests were performed at temperatures of 20°C and 50°C. Results of the friction tests conducted at 20°C are shown in Figure 4.14. Similar to Figure 4.11, the torque plots have characteristics of Coulomb-dominated friction, and the appearance of a peak torque and shear stress is due to the breaking the adhesive bond that forms between the rotating plate

and resin prior to testing. It is demonstrated that higher sliding velocities result in larger torque and shear stress due to higher forces required to deform the resin. At a test temperature of 50°C, much of the velocity dependence remains, as demonstrated in Figure 4.15. In contrast to the torque plots at 20°C, the torque instantly peaks at a maximum value at the start of the test, decrease to a minimum then increasing toward a plateau level. Increasing the velocity and shear rate increases the torque and corresponding shear stress, which would be an expected trend in viscous materials if no sliding occurs; however, it is likely that the annulus has initiated mechanical interlocking of the prepreg fibers as the rheometer gap continually decreases while redistributing the resin during rotation. Local heating at the prepreg/annulus interface at higher velocities may also be a possibility as frictional sliding continues to larger rotation angles.

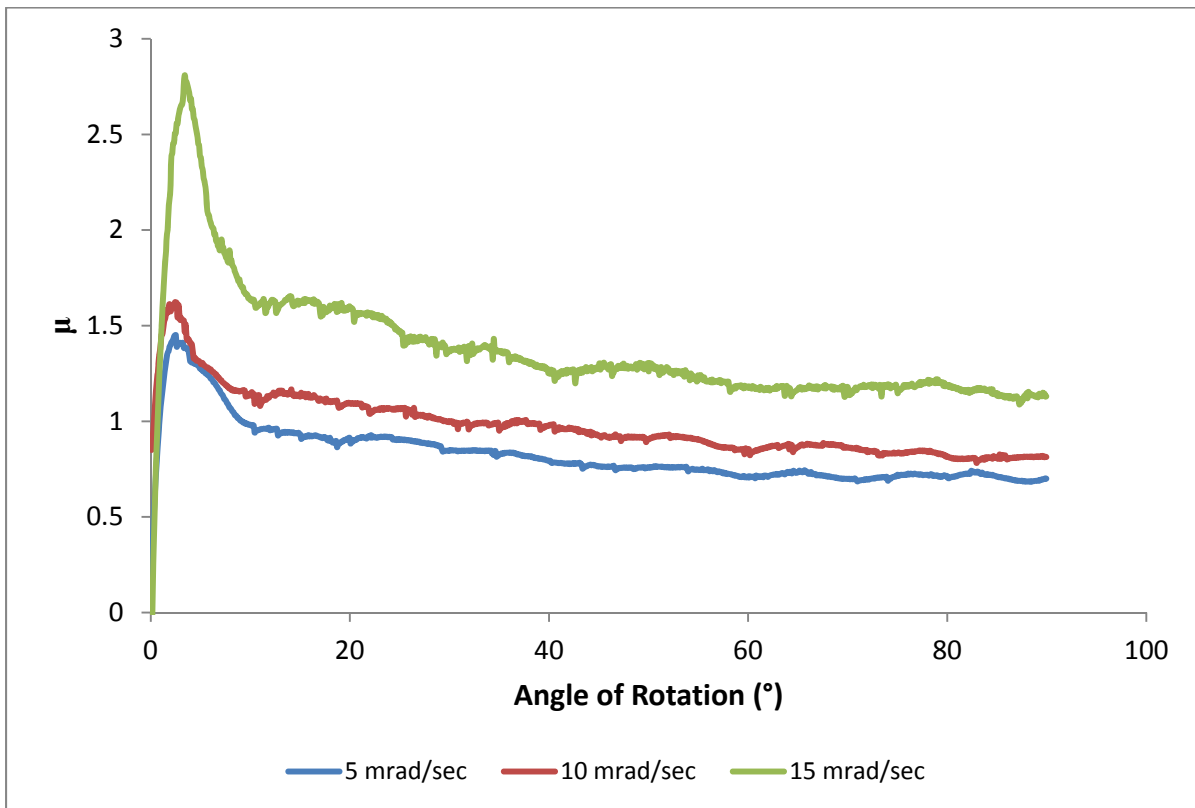


Figure 4.14. Calculated COF (μ) vs. angle of rotation for friction tests conducted at 20° C and 5 N normal compressive force.

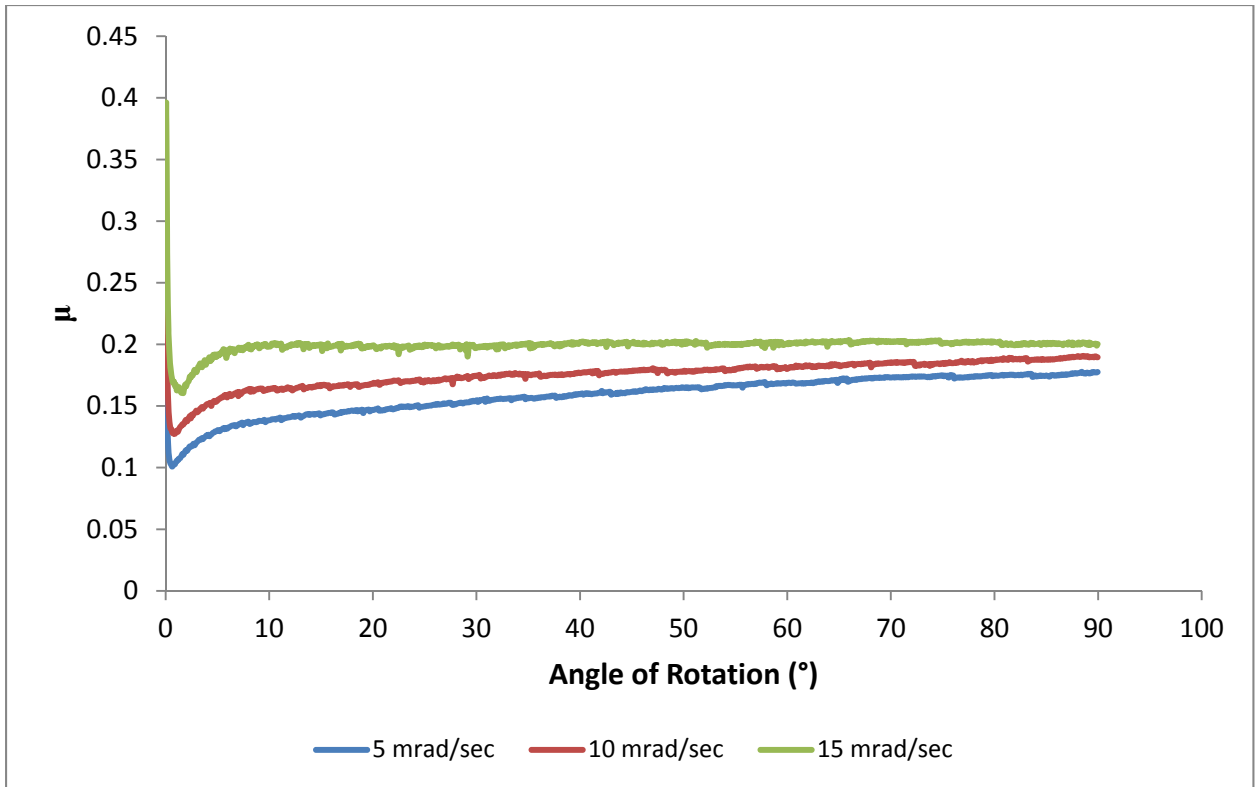


Figure 4.15. Calculated COF (μ) vs. angle of rotation for friction tests conducted at 50° C and 15 N normal force.

Influence of pressure

Normal forces of 5, 10, and 15 N corresponding to contact pressures of 13.94, 27.88, and 41.83 kPa were investigated to observe the influence of contact pressure. Results from the tests are shown in Figure 4.16.

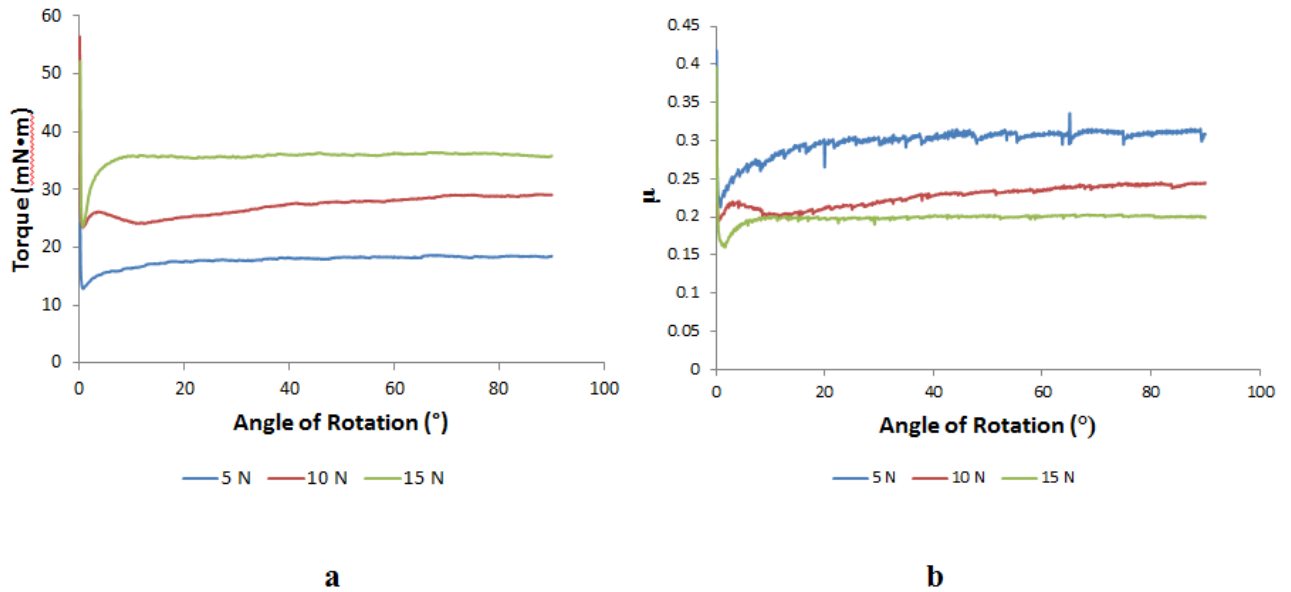


Figure 4.16. a) Torque and b) COF (μ) vs. angle of rotation for friction tests conducted at 50° C and 15 mrad/sec.

Similar trends of velocity dependence are also observed for contact pressure. The torque is shown to have a maximum peak at the start of the test due to the same reasons outlined in the previous section. Increases in contact pressure lead to higher values of torque and shear stress, trends which are consistent with interply shear with the Twintex fabric as shown in the work of Vanclooster et al [94]. Increasing the normal force also leads to lower values of the COFs for the prepregs, as expected for more viscous-like behavior. Assuming a non-uniform resin surface, introducing larger contact pressures may result in resin being squeezed out from the interface, resulting in smoothing of the resin surface that would increase the contact area and effectively reduce the COF.

Discussion

Literature Overview

Within the context of the rheometer, the results indicate that the frictional mechanisms of composite forming involve complex interactions between the annulus,

resin, and prepreg fibers. When exposed to higher temperature conditions, the resin is predicted to become less viscous and could act as a lubricating film between the tool and prepreg fibers. Such a phenomenon introduces additional complexity as both Coulomb friction and viscous flow of the resin are predicted to contribute to the frictional responses. While the viscosity of the resin was not determined or available from the manufacturer, such information is needed to generate a Stribeck curve, which can be used to convey the level of frictional contact at the annulus/prepreg interface.

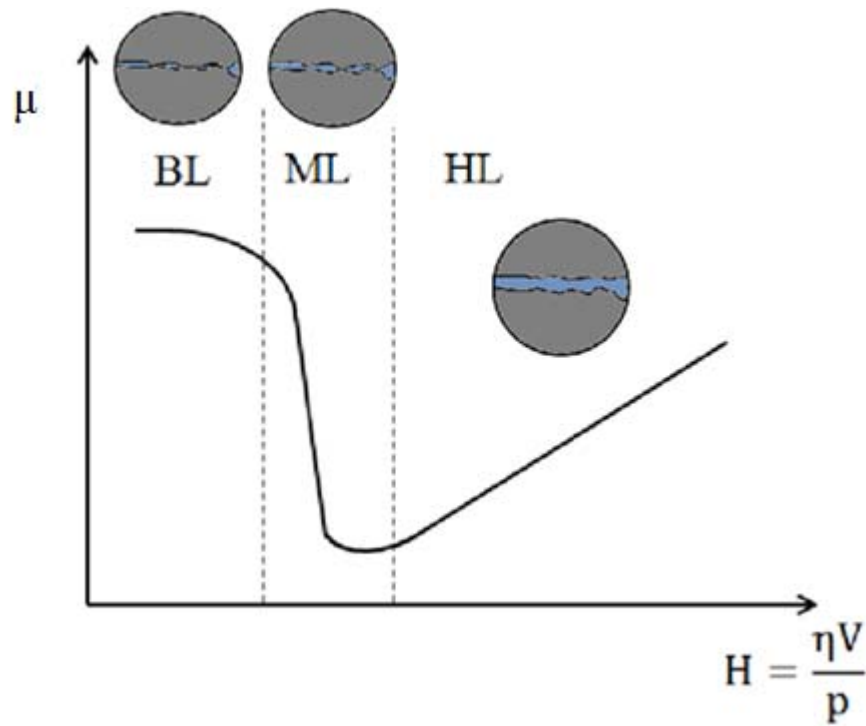


Figure 4.17. Generalized Stribeck curve divided into three regions. a) boundary lubrication (BL), b) mixed lubrication (ML), and c) hydrodynamic lubrication (HL).

The curve plots the variation of the friction coefficient of μ against the Hersey number H , a nondimensional quantity that is dependent on the dynamic viscosity of the fluid η , the velocity V , and the normal load per unit width p . The curve is categorized into three regions based on the level of contact between the surfaces of interest. Boundary

lubrication (BL) is the initial region that is primarily governed by Coulomb friction or interaction between surface asperities [4, 7], where the fluid film thickness is negligible and has an insignificant effect on friction. As the film thickness increases, the curve moves into the mixed lubrication (ML) regime where the contacting surfaces are completely separated by the fluid film and the coefficient of friction reaches a minimum value. In this region, characteristics of Coulomb and hydrodynamic friction will be present between the surfaces. As the fluid film thickness increases and becomes more viscous, the coefficient of friction will increase due to viscous shear and drag that occurs between the contacting surfaces [7]. At the hydrodynamic lubrication (HL) regime, viscous behavior dominates and the fluid film has sufficient thickness and viscosity to support the loads between the contacting interface at high velocities by hydrodynamic pressure [4, 7, 43].

From observation of the friction graph in Figure 4.15 collected at 50° C, under a constant pressure, increasing the velocity produces an increase in the torque and corresponding COF. Such trends indicate that this frictional behavior may be at the transition between mixed and hydrodynamic lubrication as indicated in Figure 4.17. This result is further supported by Figure 4.16, where the COF is seen to decrease with increasing normal force, which is demonstrated to be within the mixed lubrication regime. While these predictions are based on three data points, a wider range of temperatures, pressures, and velocities are clearly needed to confirm the concave parabolic shape of the mixed lubrication regime shown in Figure 4.17.

While the Stribeck curve provides a general perspective on the level of contact between the two surfaces, the individual contributions of Coulomb and viscous friction

remain relatively unknown due to the limited data collected. However, some observations on the relative contributions of Coulomb and viscous friction can be made by considering how the two mechanisms are coupled. One may consider a Kelvin-Voigt model or parallel coupling of Coulomb and viscous friction, where each component experiences the same displacement (assuming negligible radial variation) during rotation as shown in Figure 4.18.

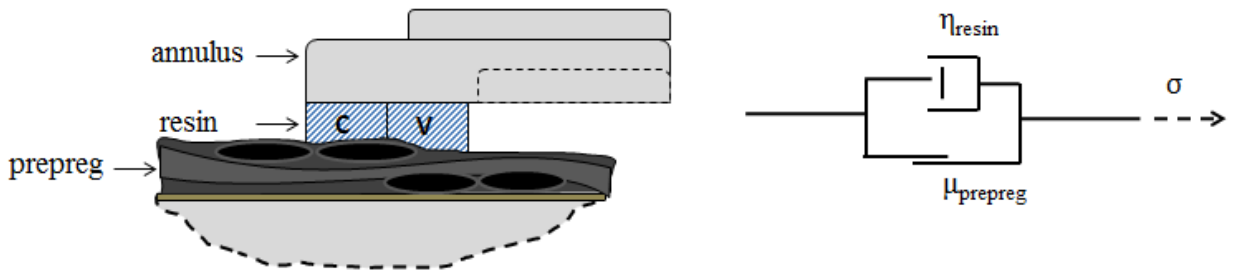


Figure 4.18. Depiction of parallel coupling of Coulomb (C) and viscous (V) friction.

In reviewing the literature, a number of frictional models can be utilized in order to approximate the parallel coupling of Coulomb and viscous friction. One approach may be used by summing the shear stresses from Coulomb friction and viscous shear [95]:

$$\tau = \mu\sigma_n + \eta\dot{\gamma} \quad (4.5)$$

where σ_n is the normal stress and $\dot{\gamma}$ is the shear rate. Wilks employed this model when analyzing the effect of processing parameters on shear stress during the forming process [95]. Clifford et al. extended the model from equation 4.5 by adding a factor ϕ , which is the ratio of contact area between the fibers and tool to the area of the tool [96].

$$\tau = \mu\sigma_n + \phi\eta\dot{\gamma} \quad (4.6)$$

Chow derived a model for his research which combines the effects of Coulomb and hydrodynamic friction to calculate an effective COF given by [97]:

$$\mu_{eff} = \frac{F_T}{N_T} = \frac{\mu_c N_c + \eta_r \dot{\gamma} A_r}{N_T} \quad (4.7)$$

where μ_c is the Coulomb COF, N_c is the normal load applied to asperities, η_r is the resin viscosity, $\dot{\gamma}$ is the shear rate, A_r is the fluid film contact area, F_T is the total friction force and N_T is the total normal load. The Coulomb portion of the total frictional force consists of a sum of individual forces from the contacting asperities, while the viscous shear term accounts for fluid shear resulting from contact between the resin layer and forming tool. Equation 4.7 can be further modified by replacing the viscosity term with known rheological models such as the Power Law [97].

$$\mu_{eff} = \frac{\mu_c N_c + (m \cdot \dot{\gamma}^{n-1}) \dot{\gamma} A_r}{N_T} \quad (4.8)$$

where m is the consistency and n is the power law index, both which are experimentally determined parameters. To account for the proportions of Coulomb normal force to the total normal force, Chow introduced a factor a which ranges from 0 to 1 [97].

$$\mu_{eff} = \frac{\mu_c (a \cdot N_T) + (m \cdot \dot{\gamma}^{n-1}) \dot{\gamma} A_r}{N_T} \quad (4.9)$$

Chow derived this model based on the observation that his data fell within the mixed lubrication regime.

Statistical Modeling

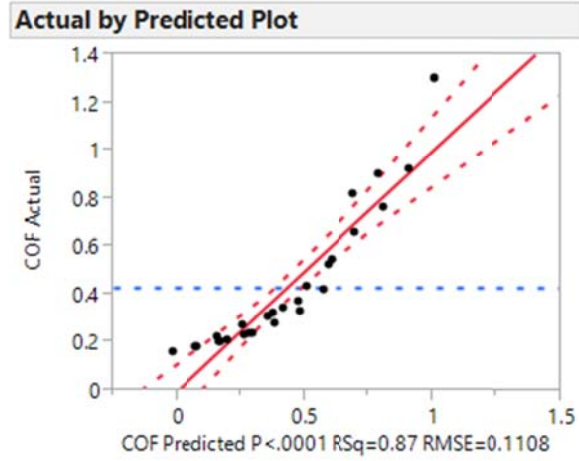
In addition to methods established in the literature, a design of experiment analysis is conducted with data collected from this study to model the COF as a function of the test temperature, pressure, and rotational sliding velocity using the JMP software (Cary, NC). Developing a model of the COF with the existing data may be used for modeling work and to see what insights can be gained from the generated models. By

modeling the COF using first order terms only, an empirical model of the COF is developed and shown in Figure 4.19. The model developed provides a reasonable fit of the actual COFs, as suggested by the R-squared value of 0.87. However, the data points in the initial region of the curve indicates that non-linearity in the frictional processes is prevalent. This non-linearity is likely associated with the temperature, which is shown to be the most statistically significant; given that the probability value ($Prob > |t|$) of the t -ratio is much smaller than the alpha value of 0.05 at a 95% level of confidence. Alpha is a threshold value used to judge whether a test statistic, or t -ratio, is statistically significant. From Figure 4.19, the values of the estimates column from the parameter estimates table provide the coefficients from the first order terms. The resulting relationship is given by:

$$\mu = 7.157 - 1.337 \cdot 10^{-3} P - 0.022 T_k + 0.019 V \quad (4.10)$$

where P is the pressure in kPa, T_k is the absolute temperature in Kelvin, and V is the velocity in mrad/sec. As the shape of this non-linearity is reminiscent of a parabola, the model is modified as the order of approximation is increased to include a complete set of the second order terms as depicted in Figure 4.20. At a 95% level of confidence and alpha value of 0.05, the accuracy of the second order model in relation to experimental data is greatly improved given by the R-squared value of 0.97, as it accounts for the non-linearity associated with the test temperature. Although this model contains ten terms, the parameter estimates table in Figure 4.20 indicate that some terms in the model may be omitted as they are statistically insignificant to the COF as they exceed the alpha value of 0.05. The resulting relationship using second order terms is given by:

$$\begin{aligned} \mu = & 4.69410^{-4} T_k^2 + 6.84610^{-6} P^2 + 1.67010^{-4} V^2 - 1.32810^{-3} T_k V - 6.18310^{-5} P V \\ & - 5.63810^{-5} P T_k - 0.305 T_k - 0.020 P + 0.436 V + 49916 \end{aligned} \quad (4.11)$$



Summary of Fit	
RSquare	0.869
RSquare Adj	0.852
Root Mean Square Error	0.111
Mean of Response	0.428
Observations (or Sum Wgts)	27.000

Parameter Estimates				
Term	Estimate	Std Error	t Ratio	Prob> t
Intercept	7.157	0.686	10.43	<.0001*
TK	-0.022	0.002	-9.60	<.0001*
V	0.019	0.005	3.66	0.0013*
P	-0.001	0.000	-3.03	0.0059*

Figure 4.19. Statistics of first order model of COF as a function of T_K (temperature in Kelvin), V (rotational sliding velocity in mrad/sec), and normal pressure P (in kPa)

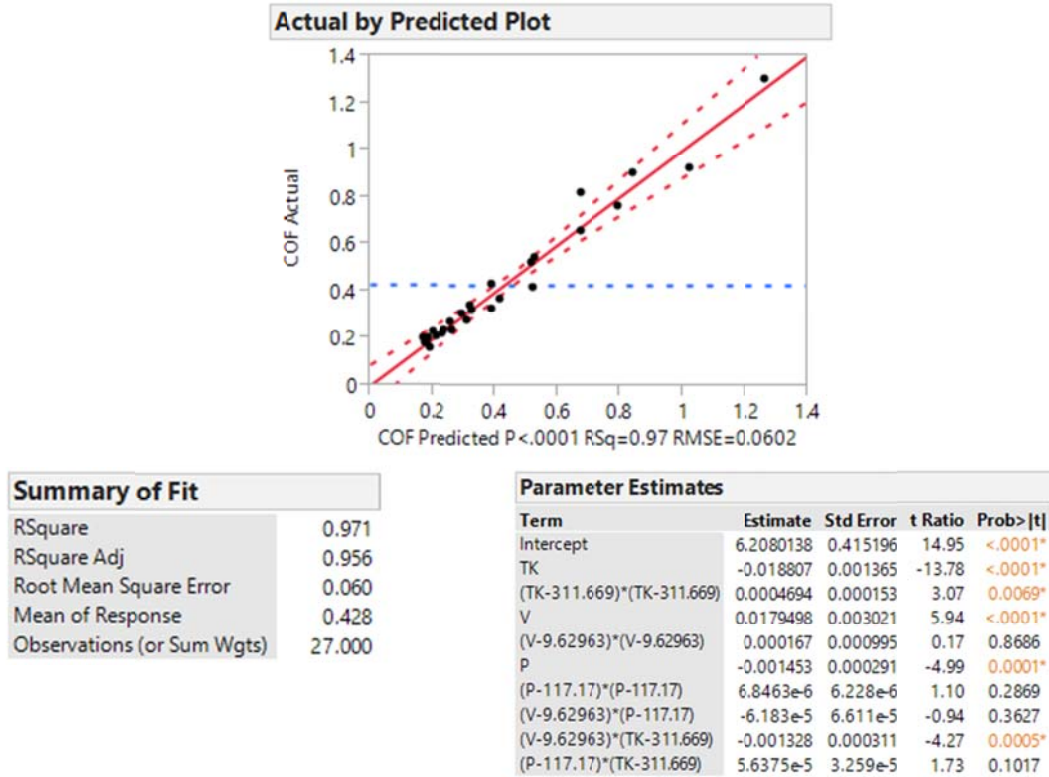


Figure 4.20. Statistics of second order model of COF as a function of T_K (temperature in Kelvin), V (rotational sliding velocity in mrad/sec), and normal pressure P (in kPa)

In addition to the parallel friction models discussed earlier, a series configuration was derived by the authors to model the frictional mechanisms, but this model was incapable of capturing the rate dependence that was observed when slip was occurring. It was then necessary to develop a more complex approach where a parallel and series combination coupling of the frictional mechanisms is considered and depicted in Figure 4.21.

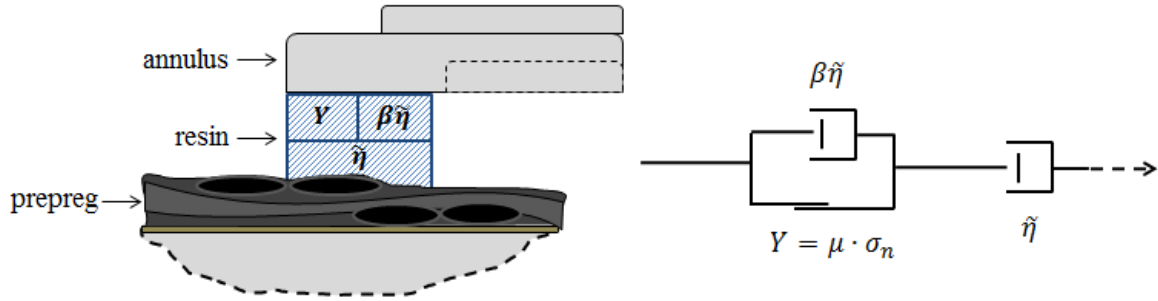


Figure 4.21. Parallel + series model for friction

where $\tilde{\eta}$ is a lumped term that consists of the effective viscosity and thickness of the resin, β is a fractional term, and Y is the shear stress due to Coulomb effects. In this configuration, the displacement of the system can be characterized by the equation below:

$$\delta = \frac{\tau t}{\tilde{\eta}} + \frac{\tau t}{\beta \tilde{\eta}} - \frac{Yt}{\beta \tilde{\eta}} = r_{avg} \dot{\theta} t \quad (4.12)$$

where τ is the shear stress, t is the time, r_{avg} is the average radius of the annulus, and $\dot{\theta}$ is the angular velocity. By rearranging terms, the shear stress τ of the system can be determined:

$$\tau = \frac{\eta r_{avg} \dot{\theta}}{\left(1 + \frac{1}{\beta}\right)} + \left(\frac{Y}{\beta + 1}\right) \quad (4.13)$$

By dividing equation 4.13 by the normal stress or pressure σ_n , the effective COF μ_{eff} is shown to be:

$$\mu_{eff} = \frac{\tau}{\sigma_n} = \frac{\eta r_{avg} \dot{\theta}}{\sigma_n \left(1 + \frac{1}{\beta}\right)} + \left(\frac{\mu}{\beta + 1}\right) \quad (4.14)$$

For this prepreg system, the epoxy resin is assumed to follow an Arrhenius relationship,

where the viscosity can take the form $\tilde{\eta} = \tilde{\eta}_0 e^{\frac{E}{RT}}$, where R is the universal gas constant,

E is the activation energy, and T is the absolute temperature. Equation 4.14 is modified to give the equation below.

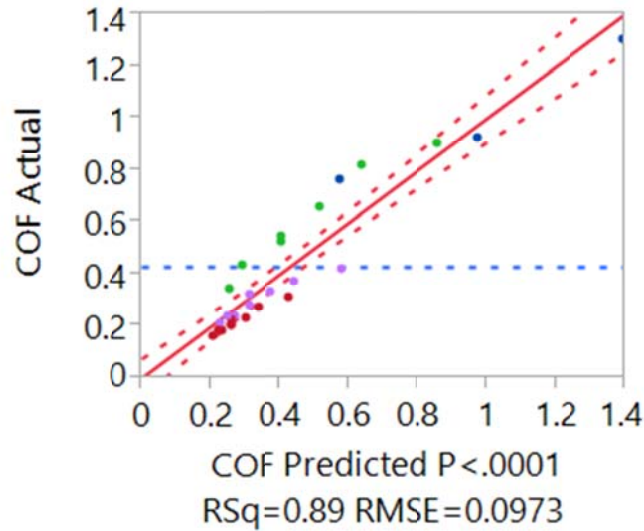
$$\mu_{eff} = \frac{\tilde{\eta}_0 r_{avg} \dot{\theta}}{\sigma_n \left(1 + \frac{1}{\beta}\right)} e^{\frac{E}{RT}} + \left(\frac{\mu}{\beta + 1}\right) = A \left(\frac{\dot{\theta} e^{\frac{E}{RT}}}{\sigma_n}\right) + B \quad (4.15)$$

where $A = \frac{\tilde{\eta}_0 r_{avg}}{\left(1 + \frac{1}{\beta}\right)}$ and $B = \frac{\mu}{\beta + 1}$. When the COF takes the form of equation 4.15, the

angular velocity $\dot{\theta}$, normal pressure σ_n , and temperature T , all which are known from this study, are extracted as dependent variables. Although data on the current system was not available, the activation energy of an epoxy resin-acid anhydride system was determined by Shimazaki [98] to be in the range of 41.8 – 209.2 kJ/mol from. By using $E = 41.8$ kJ/mol, which is appropriate if the reported resin system is assumed to be in the initial stages of curing [98], one obtains $\frac{E}{R} = 5032$ K. Using the JMP software, a model of the COF is made in accordance to equation 4.15 as shown in Figure 4.22, where the model is given by:

$$\mu = 1.821 \cdot 10^{-7} \left(\frac{\dot{\theta} e^{\frac{E}{RT}}}{\sigma_n}\right) + 0.18 \quad (4.16)$$

This two term model and fit shows reasonable accuracy as given by the R-squared value of 0.89. Figure 4.22 shows that the data points at the lower test temperatures of 20 and 30°C, given by the blue and green data points, respectively, tend to deviate from the model the most. Nonetheless, this result is noteworthy as this simple model shows that the frictional processes of the prepreg can be adequately described by the Arrhenius relationship as derived from this parallel+series combination.



Summary of Fit		Parameter Estimates				
RSquare	0.891	Term	Estimate	Std Error	t Ratio	Prob> t
RSquare Adj	0.886	Intercept	1.801e-1	0.02555	7.05	<.0001*
Root Mean Square Error	0.097	theta*exp(1/T)/sigma	1.821e-7	1.276e-8	14.27	<.0001*
Mean of Response	0.428					
Observations (or Sum Wgts)	27.000					

Figure 4.22. JMP model and statistics of equation 4.15. Data points are plotted for 20°C (blue), 30°C (green), 40°C (purple), and 50°C (red)

Conclusions

A standard torsional rheometer is used as a means to study the frictional processes associated with the composite forming process. Dry textile graphite and glass fabrics and graphite/epoxy composite prepregs were tested and analyzed under a variety of contact pressures, temperatures, and sliding velocities. The preliminary results show that textile fabric sliding is predominantly controlled by dry Coulomb friction, though the glass fiber fabric exhibited some contact pressure dependency, perhaps due to its higher compressibility and fiber mobility. The prepregs demonstrate much larger variations to measurement due to the nature of the resin. Statistical modeling of the data reveals that temperature has the highest influence on friction as it is the most statistically significant

variable. When observing results in relation to the Stribeck curve, the prepregs exhibit behavior and trends typically seen within the mixed lubrication regime, such as decreasing COF with increasing temperature and normal pressure. Within the mixed lubrication regime, both Coulomb and hydrodynamic lubrication dominate the frictional processes, but the relative contributions from each component remain unknown due to the lack of data. While a number of methods from the literature are available to describe the parallel coupling of frictional mechanisms, an attempt was made to model the system as a parallel+series configuration using JMP. Assuming an Arrhenius relationship with the resin viscosity, the model constructed for the parallel+series configuration is shown to have reasonable accuracy in relation to experimental results.

The rheometer is shown to have the capability of performing frictional tests within the typical parameters of the composite forming process. While the results in this study were limited to a small range of temperature, pressure, and sliding velocities, future experiments may be conducted to test the prepregs within the wider range of parameters that may be extrapolated within the regions of the Stribeck curve.

Chapter 5: Summary and Conclusions

Observations

This thesis presents a study of characterizing the fracture properties of AM materials with specific interest in the fracture resistance and interface between the TB and VW. An attempt is made to extend the test methods and standards created for adhesive bonding to the application of AM materials by printing specimens as laminated beams, particularly in the DCB, TDCB and T-peel configurations. A comparison of the methods is made to determine which specimen would be most appropriate for test standardization in terms of the accuracy of measurement and minimization of manufacturing costs. The results revealed stark differences of fracture energy and failure loci for each specimen considered, but in general, the TB/VW interface shows significant rate dependency that is modeled by a power law relationship. The fully-printed test configurations revealed possible exaggeration of the measured fracture energies, primarily due to viscoelastic dissipation of the polymeric adherends. Attempts to reduce this effect with the addition of bonded steel plates proved to be insufficient and resulted in larger fracture energies than anticipated. Small AM strips were also printed and bonded to aluminum auxiliary adherends to minimize adherend dissipation, but the results reveal that this particular configuration demonstrated the lowest fracture resistance in contrast to the other test configurations. Print orientation is documented to have a significant effect on the fracture resistance of AM materials. The interlayer is shown to have increased fracture properties when printed on its edge ($\bar{x}zy$ orientation) due benefits of polymer blending and loading perpendicular to the print direction, though this was not seen for the $\bar{y}zx$ as this orientation resulted in the lowest fracture resistance due to the

lack of polymer drawing and discretization of the TB. The T-peel reveals potential opportunities for enhanced mechanical performance by implementing intricate material patterns at the interlayer.

While the results of the AI-DCB are vastly different for each orientation, it is concluded that this configuration is the preferred specimen to be used for fracture testing of AM materials due to minimal adherend dissipation in comparison to the fully-printed variety. Such variation of the fracture energies for this specimen may be associated with the part spacing of the AM strips, which was not considered when printing the parts on the same tray [35].

In addition to AM materials, this study is also extended to the manufacturing of composite materials with particular emphasis on the frictional mechanisms involved in the forming process. While the rheometer is traditionally used for measuring the viscous properties of polymer liquids and melts, certain modifications are made to perform friction testing while taking advantage of the instrument's precise control of normal force, temperature, and sliding velocity. The rotating plate is machined into an annulus geometry which would allow an approximately constant sliding velocity to occur between the contacting surfaces. Dry textile fabrics and composite prepregs are tested on the rheometer and the results show different frictional mechanisms govern each material. The dry textile fabrics are shown to be primarily governed by Coulomb friction, as the COF is independent of pressure and velocity, though this was not the case for the glass fiber, as the material is predicted to have higher fiber compressibility and mobility. The prepregs are shown to have higher variation of measurement due to the presence of the epoxy resin. In general, the prepreg shows a large dependency to temperature, pressure,

and sliding velocity and displays frictional behavior within the mixed lubrication regime of the Stribeck curve. By coupling the frictional processes as a parallel+series combination, statistical modeling has revealed that the resin may be in the initial stages of curing, given by the significant amount of resin drawing that occurs at the higher test temperatures.

Areas of Improvement and Future Work

While the research conducted for this thesis has provided significant insight to both AM and composite materials, there are certain items or areas that can be improved to further the understanding of these materials. In relation to AM, it would of interest to observe the fracture properties of these materials under the other fracture modes such as mode II or mixed mode I/II. Such additional data may have provided additional understanding of the failure path of these materials and determine whether the alternating failures and discretized patches of TB would also hold in the other fracture modes. Aside from the gradient pattern, other designs of interface architecture are also worth exploring. As seen from the work of Dimas et. al [59], the fracture properties of printed composites can be optimized when the appropriate material topology is selected. It is predicted that multiple material combinations can be printed and fracture energy can be maximized for any print orientation. To expand this study to a much larger scope, a thorough survey of fracture characterization of multi-materials specimens developed from other AM methods would have been valuable to the research community.

This thesis has also demonstrated that the frictional interactions associated with the composite forming process are highly dependent on temperature, pressure, and sliding velocity. Since the resin was shown to introduce temperature and time dependencies on

friction, additional analyses, such as time temperature superposition, would have provided some additional perspective on how the frictional response would change under several decades of frequency or shear rates. While friction tests were performed under constant angular velocity, other rheometer tests, such as time or stress sweep, would have been interesting to explore.

Appendix A: Corrected Beam Theory vs. Experimental Compliance Method

In addition to corrected beam theory, the experimental compliance method (ECM) was also used as an alternative method to calculate the fracture energy.

$$G_{ic} = \frac{nP\delta}{2Ba} \cdot \frac{F}{N} \quad (\text{A.1})$$

where P and δ are the load and displacement at crack propagation, B is the width of the specimen, and a is the observed crack length. When using this approach, a plot of normalized compliance C/N against the crack length a , both in logarithm scale, is generated as shown in Figure A.1.

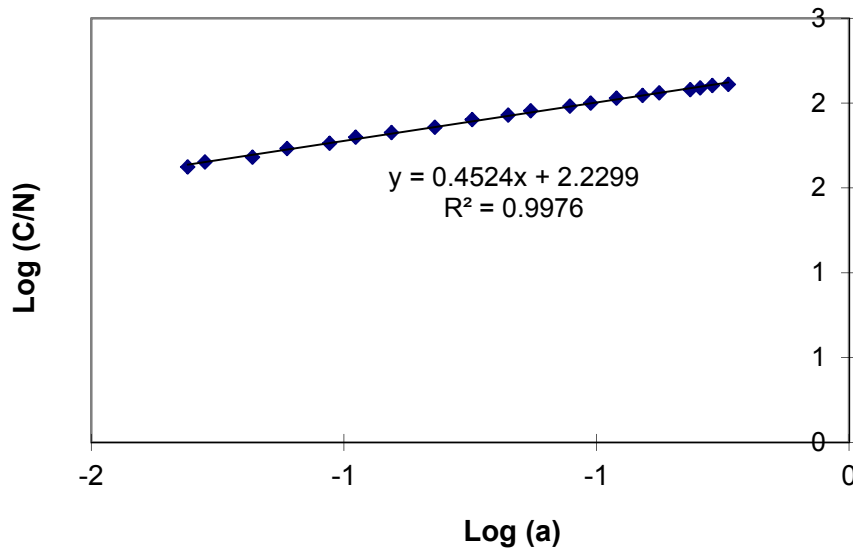


Figure A.1. Plot of logarithm of normalized compliance C/N vs. logarithm of crack length a , with slope n .

The slope of this plot, given by n , can be used to determine G_{ic} using equation A.1 above. The large displacement factor F and load block correction factor N used for CBT are also applicable to ECM. For the purposes of comparison, the fracture energy calculated at different displacement rates is shown in Figure A.2.

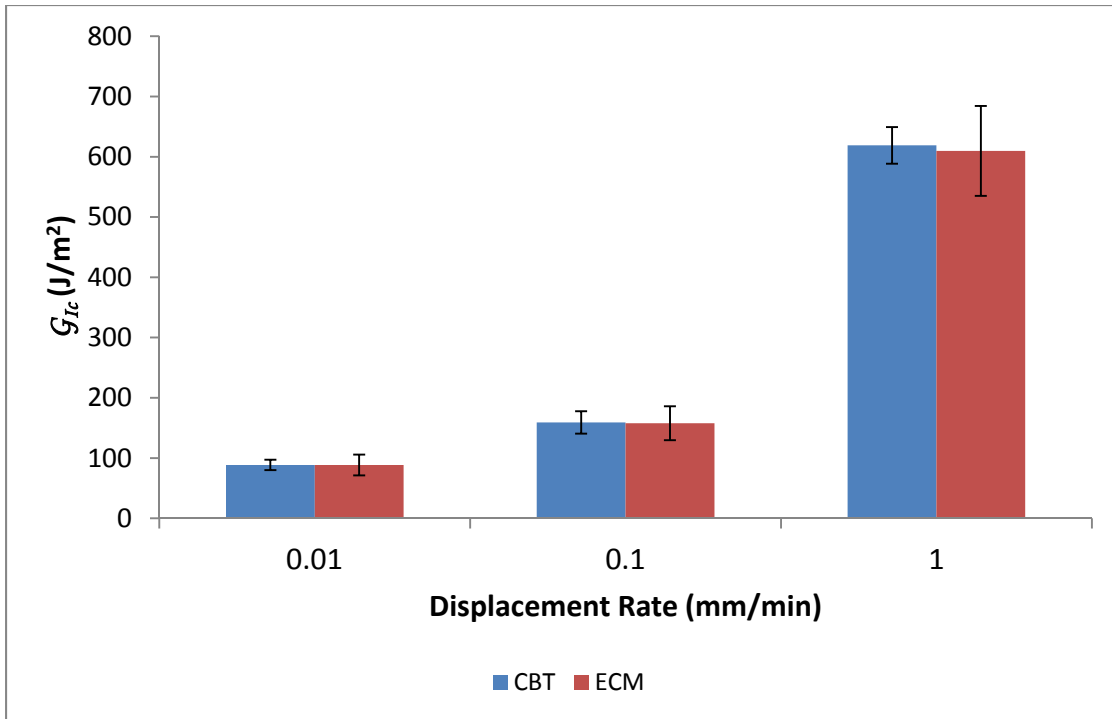


Figure A.2. Comparison of fracture energy calculated by CBT and ECM.

While the fracture energies calculated by both methods show similar values of fracture energies, it is seen that values calculated from ECM have larger variability than those calculated by CBT. Based on these observations, CBT was chosen as the primary method of analysis.

Appendix B: AM Interface Architecture (Checked)

In addition to the original TB/VW and gradient interface, a very coarse checkered pattern with alternating patterns of TB and TB60 is also printed and tested, with dimensions given in Figure B.1. This configuration is also printed in the $\bar{x}yz$ orientation and the data collected is shown in Figure B.2 and Table B.1 with the other configurations.

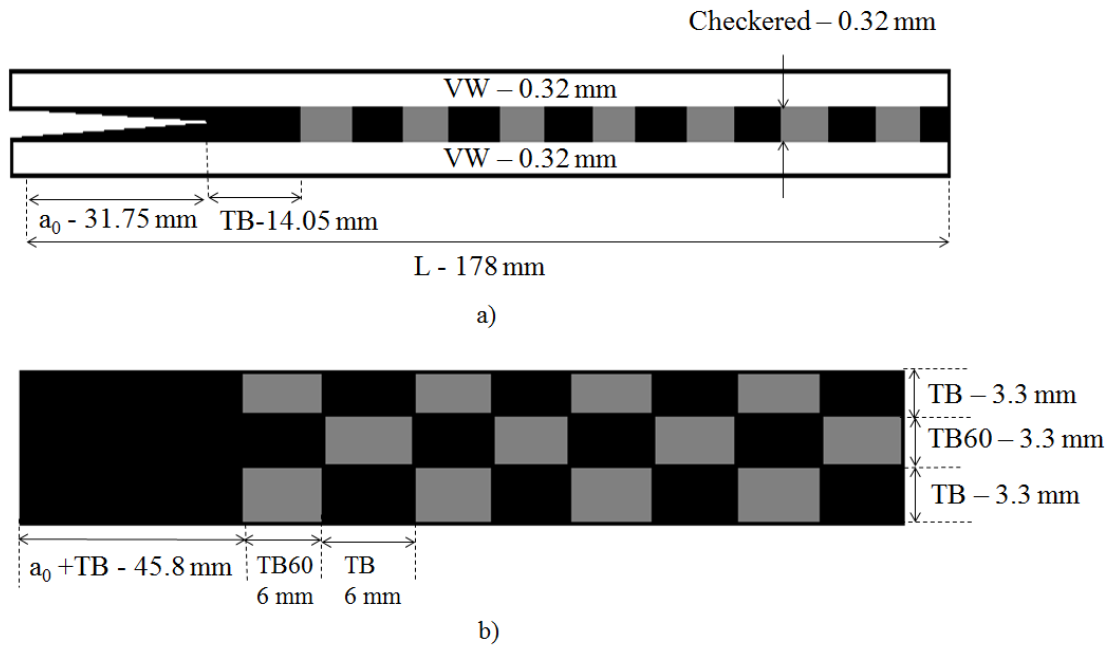


Figure B.1. AM test strip with a very coarse "checked" patterns of TangoBlack (TB) and TangoBlackShore60 (TB60) printed in the $\bar{x}yz$ orientation. a) side view and b) top view of the strip. Note: figure is not to scale.

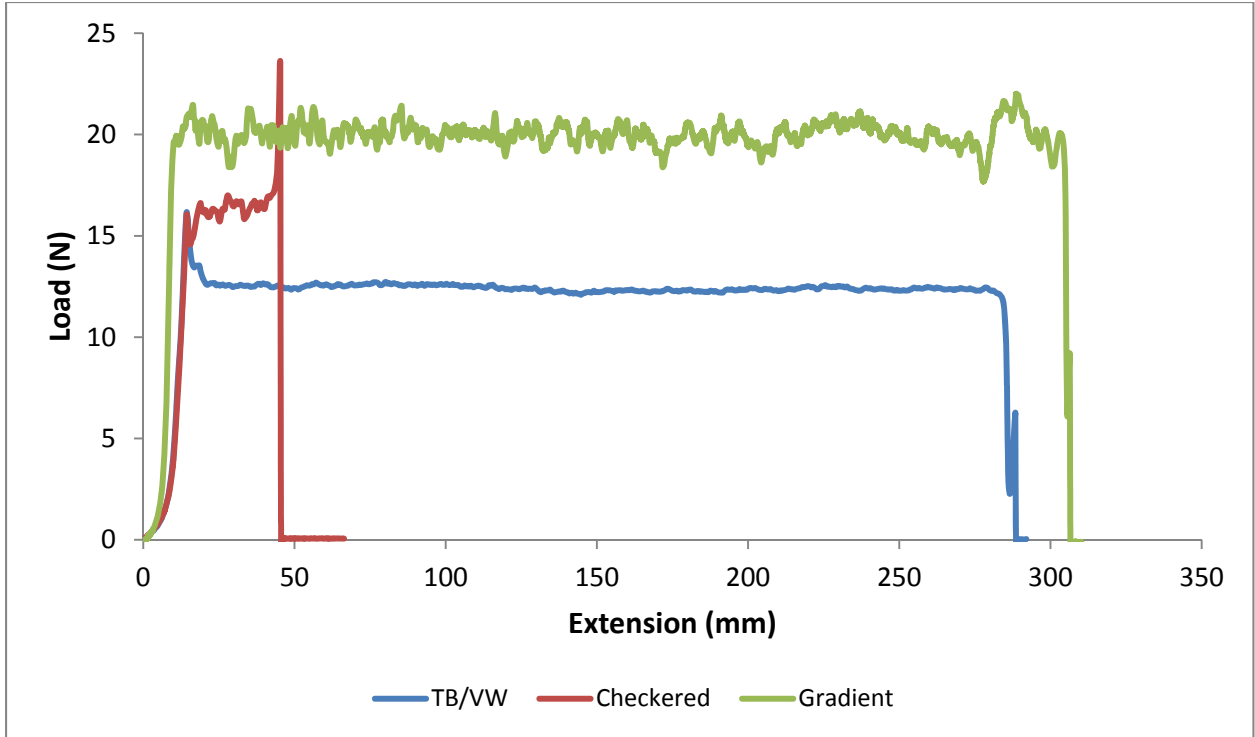


Figure B.2. Load vs. extension curves from T-peel tests with addition of checkered pattern.

Table B.1. T-peel results

	TB/VW	Checkered	Gradient
Average Force (N)	12.40	NA	20.08
Energy Release Rate (J/m^2)	2505	NA	4057

The original TB/VW interlayer configuration is the weakest in terms of peel. Data on the checkered pattern was not acquired as the interface proved to be too strong to perform peel tests, and one of the adherends broke prematurely before the checkered region was reached.

To observe dependencies of print orientation, the patterns above were also printed in the $\bar{x}zy$ orientation using the TDCB configuration and tested at 1 mm/min. The results are shown in Figure B.3. While the gradient configuration is shown to have the highest

energy release rate in the $\bar{x}zy$ orientation, this was not the case for the $\bar{x}zy$ orientation as the gradient configuration is shown to perform poorly when compared to other patterns. It is suspected that the significant polymer blending occurred between all materials used for the gradient interface, creating an interface that was substantially weaker than the TB/VW interface. Using the TDCB configuration, data for the checkered pattern was obtained and is seen to have the highest fracture resistance in the $\bar{x}zy$ orientation. It is clearly seen that an improvement on both peel and fracture performance can be accomplished by utilizing different print patterns and geometries at the central layers.

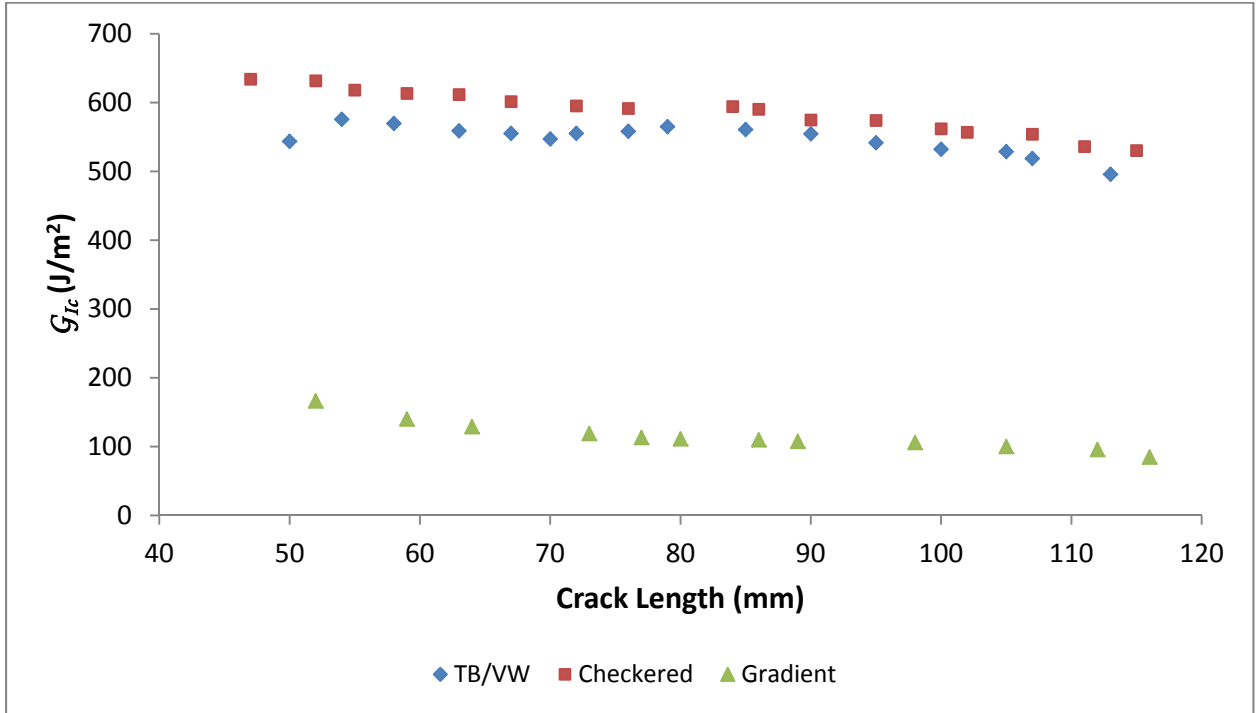
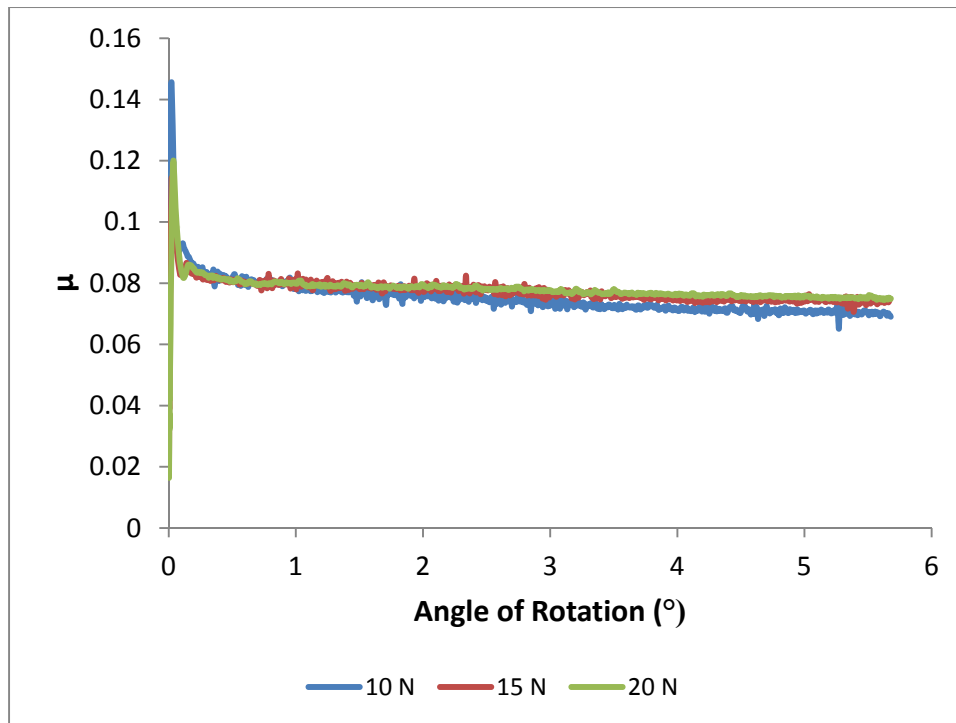


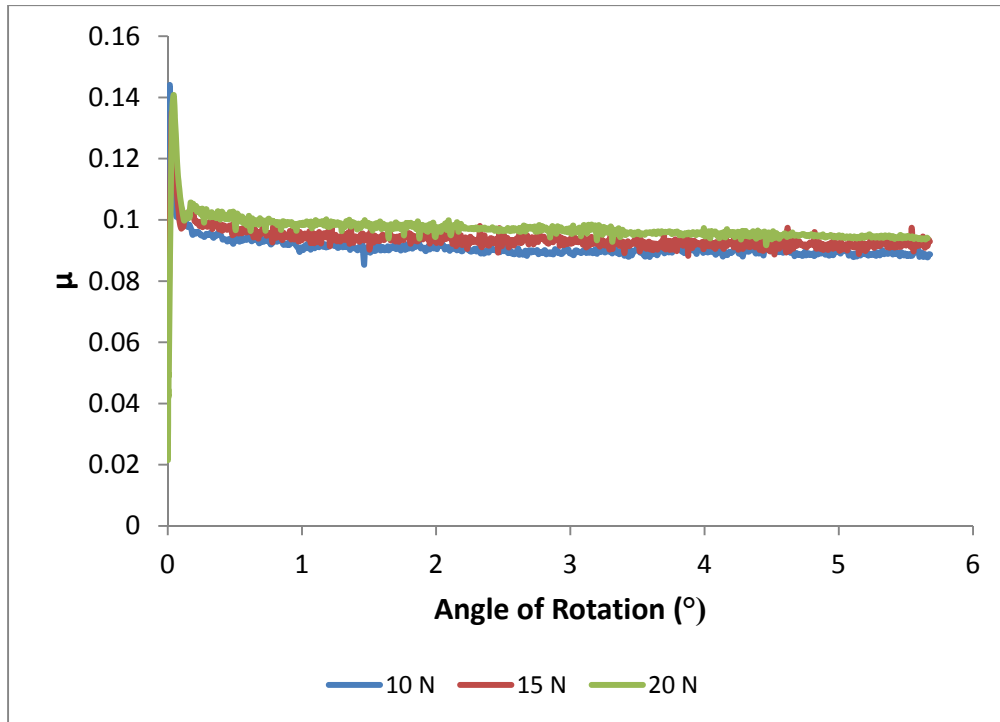
Figure B.3. G_{Ic} vs. crack length of different pattern architectures for the TDCB printed in the $\bar{x}zy$ direction.

Appendix C: Rheometer friction results for PTFE

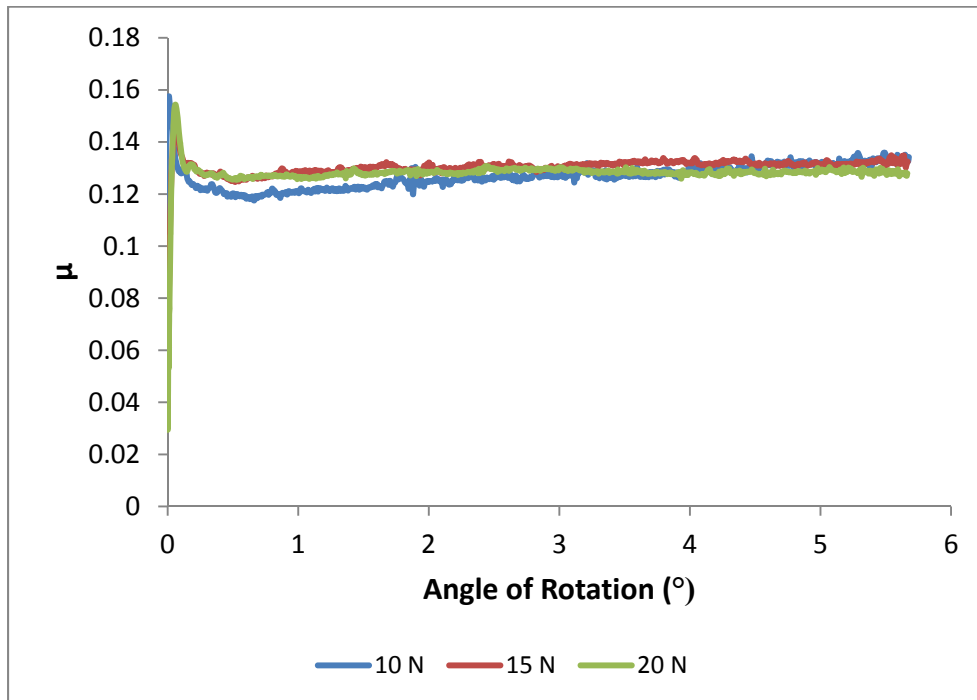
In addition to dry textile fabrics, preliminary friction tests were also conducted on a sheet of polytetrafluorethylene (PTFE). Representative friction curves are given in Figure C.1.



a)



b)



c)

Figure C.1. Coefficient of friction (COF or μ) against angle of rotation for PTFE using the a) 1 mm, b) 2 mm, and c) 4 mm annulus (sliding velocity – 100 mrad/sec).

The results show that contact of the rotating annulus and PTFE are primarily dominated by Coulomb friction as friction is independent of the sliding velocity. Similarly to the glass fiber, PTFE is shown to have contact pressure dependency but as expected with Coulomb friction, larger normal forces results in a lower COF.

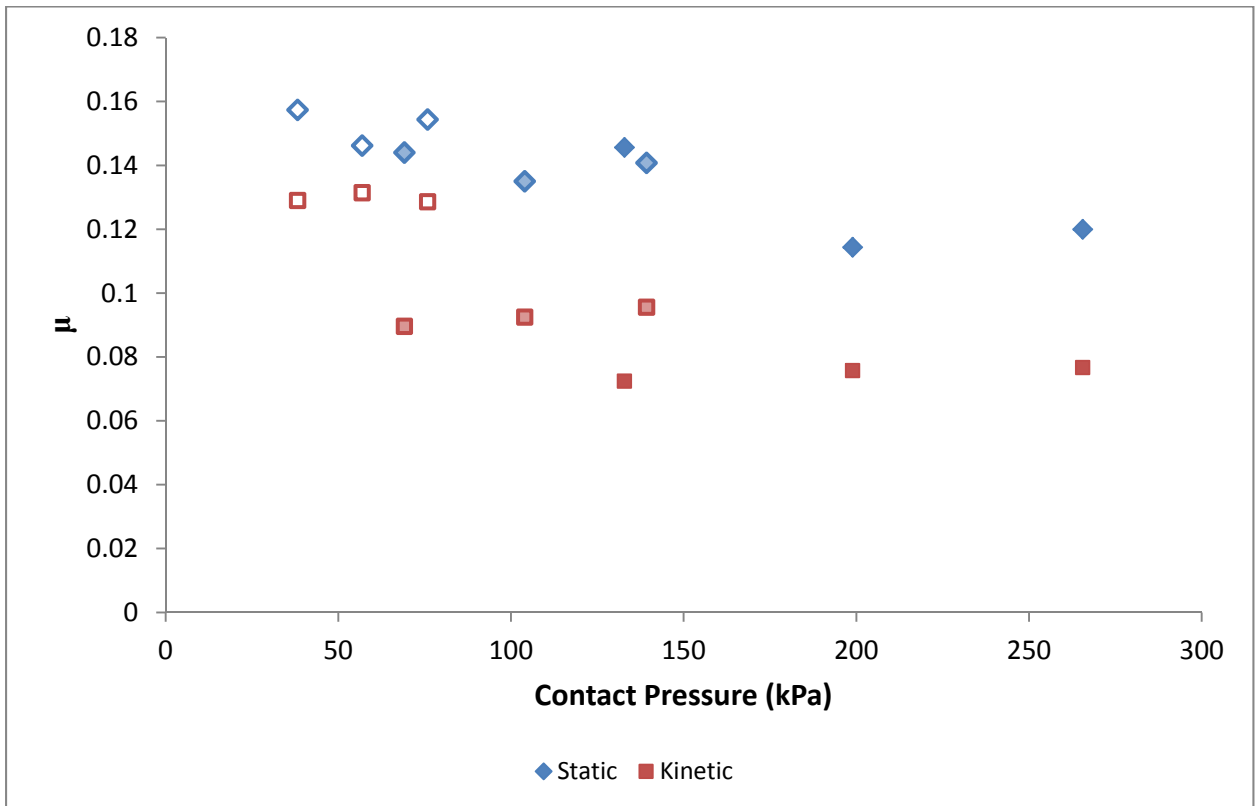


Figure C.2. Calculated coefficient of friction (μ) against contact pressure for PTFE at a rotational sliding velocity of 100 mrad/sec. (open symbols – 4 mm annulus, lightly filled symbols – 2 mm annulus, and filled symbols – 1 mm annulus)

References

- [1] Stamm M., Polymer surfaces and interfaces, *Polymer Surfaces and Interfaces: Characterization, Modification and Applications*, ISBN 978-3-540-73864-0. Springer Berlin Heidelberg, 2008, 1 (2008).
- [2] Sun J., Li M., Gu Y., Zhang D., Li Y., Zhang Z., Interply friction of carbon fiber/epoxy prepreg stacks under different processing conditions, *Journal of Composite Materials*, (2013) 0021998313476320.
- [3] Sachs U., Akkerman R., Fetfatsidis K., Vidal-Sallé E., Schumacher J., Ziegmann G., et al., Characterization of the dynamic friction of woven fabrics: Experimental methods and benchmark results, *Composites Part A: Applied Science and Manufacturing*, 67 (2014) 289-98.
- [4] Larberg Y.R., Åkermo M., On the interply friction of different generations of carbon/epoxy prepreg systems, *Composites Part A: Applied Science and Manufacturing*, 42 (2011) 1067-74.
- [5] Ten Thije R., Akkerman R., Van Der Meer L., Ubbink M., Tool-ply friction in thermoplastic composite forming, *International Journal of Material Forming*, 1 (2008) 953-6.
- [6] Kavehpour H., McKinley G., Tribo-rheometry: from gap-dependent rheology to tribology, *Tribology Letters*, 17 (2004) 327-35.
- [7] Wang Y., Wang Q.J., Stribeck curves, *Encyclopedia of Tribology*, Springer, 2013, pp. 3365-70.
- [8] ten Thije R., Akkerman R., Ubbink M., Van der Meer L., A lubrication approach to friction in thermoplastic composites forming processes, *Composites Part A: Applied Science and Manufacturing*, 42 (2011) 950-60.
- [9] ten Thije R.H.W., Akkerman R., Finite element simulations of laminated composites forming processes, *International Journal of Material Forming*, 3 (2010) 715-8.
- [10] Hallander P., Åkermo M., Mattei C., Petersson M., Nyman T., An experimental study of mechanisms behind wrinkle development during forming of composite laminates, *Composites Part A: Applied Science and Manufacturing*, 50 (2013) 54-64.
- [11] Cotterell B., Rice J.R., Slightly curved or kinked cracks, *International Journal of Fracture*, 16 (1980) 155-69.
- [12] Xie D., Waas A.M., Shahwan K.W., Schroeder J.A., Boeman R.G., Computation of energy release rates for kinking cracks based on virtual crack closure technique, *Computer Modeling in Engineering & Sciences*, 6 (2004) 515-24.
- [13] Erdogan F., Sih G.C., On the Crack Extension in Plates Under Plane Loading and transverse shear, *ASME Journal of Basic Engineering*, 85 (1963) 519-25.
- [14] Palaniswamy K., Knauss W.G., II - On the Problem of Crack Extension in Brittle Solids Under General Loading, in: Nemat-Nasser S. (Ed.), *Mechanics Today*, Pergamon, 1978, pp. 87-148.
- [15] Gol'dstein R.V., Salganik R.L., Brittle fracture of solids with arbitrary cracks, *International Journal of Fracture*, 10 (1974) 507-23.
- [16] ASTM-D3433-99, Standard Test Method for Fracture Strength in Cleavage of Adhesives in Bonded Metal Joints, *Annual Book of ASTM Standards*, ASTM, West Conshohocken, 2001, pp. 225-31.

- [17] Park S., Dillard D.A., Development of a simple mixed-mode fracture test and the resulting fracture energy envelope for an adhesive bond, *International Journal of Fracture*, 148 (2007) 261-71.
- [18] Blackman B.K., Fracture Tests, in: da Silva L.M., Öchsner A., Adams R. (Eds.), *Handbook of Adhesion Technology*, Springer Berlin Heidelberg, 2011, pp. 473-501.
- [19] Blackman B.R.K., Kinloch A.J., Paraschi M., Teo W.S., Measuring the mode I adhesive fracture energy, GIC, of structural adhesive joints: the results of an international round-robin, *International Journal of Adhesion and Adhesives*, 23 (2003) 293-305.
- [20] Determination of the mode I adhesive fracture energy, GIC, of structural adhesives using the double cantilever beam (DCB) and tapered double cantilever beam (TDCB) specimens, BS 7991:2001, 2001.
- [21] Standard Test Method for Fracture Strength in Cleavage of Adhesives in Bonded Metal Joints, ASTM D3433 - 99, West Conshohocken, PA 19428-2959, 2012.
- [22] Blackman B., Dear J., Kinloch A., Osiyemi S., The calculation of adhesive fracture energies from double-cantilever beam test specimens, *Journal of Materials Science Letters*, 10 (1991) 253-6.
- [23] Upcraft S., Fletcher R., The rapid prototyping technologies, *Assembly Automation*, 23 (2003) 318-30.
- [24] Kietzmann J., Pitt L., Berthon P., Disruptions, decisions, and destinations: Enter the age of 3-D printing and additive manufacturing, *Business Horizons*, (2014).
- [25] Utela B., Storti D., Anderson R., Ganter M., A review of process development steps for new material systems in three dimensional printing (3DP), *Journal of Manufacturing Processes*, 10 (2008) 96-104.
- [26] Yan X., Gu P., A review of rapid prototyping technologies and systems, *Computer-Aided Design*, 28 (1996) 307-18.
- [27] Pham D., Gault R., A comparison of rapid prototyping technologies, *International Journal of Machine Tools and Manufacture*, 38 (1998) 1257-87.
- [28] Bellini A., Güçeri S., Mechanical characterization of parts fabricated using fused deposition modeling, *Rapid Prototyping Journal*, 9 (2003) 252-64.
- [29] Perez A.R.T., Roberson D.A., Wicker R.B., Fracture surface analysis of 3D-printed tensile specimens of novel ABS-based materials, *Journal of Failure Analysis and Prevention*, 14 (2014) 343-53.
- [30] Ahn S.-H., Montero M., Odell D., Roundy S., Wright P.K., Anisotropic material properties of fused deposition modeling ABS, *Rapid Prototyping Journal*, 8 (2002) 248-57.
- [31] Kęsy A., Kotliński J., Mechanical properties of parts produced by using polymer jetting technology, *Archives of civil and mechanical engineering*, 10 (2010) 37-50.
- [32] Kim G., Oh Y., A benchmark study on rapid prototyping processes and machines: quantitative comparisons of mechanical properties, accuracy, roughness, speed, and material cost, *Proceedings of the Institution of Mechanical Engineers, Part B: Journal of Engineering Manufacture*, 222 (2008) 201-15.
- [33] Cazón A., Morer P., Matey L., PolyJet technology for product prototyping: Tensile strength and surface roughness properties, *Proceedings of the Institution of Mechanical Engineers, Part B: Journal of Engineering Manufacture*, 228 (2014) 1664-75.

- [34] Pilipović A., Raos P., Šercer M., Experimental analysis of properties of materials for rapid prototyping, *The International Journal of Advanced Manufacturing Technology*, 40 (2009) 105-15.
- [35] Barclift M.W., Williams C.B., Examining variability in the mechanical properties of parts manufactured via polyjet direct 3D printing, *International Solid Freeform Fabrication Symposium*, August, 2012, pp. 6-8.
- [36] Moore J.P., Williams C.B., Fatigue Characterization of 3D Printed Elastomer Material, *International Solid Freeform Fabrication Symposium*, 2012, pp. 641-55.
- [37] Okine R.K., Analysis of forming parts from advanced thermoplastic composite sheet materials, *Journal of Thermoplastic Composite Materials*, 2 (1989) 50-76.
- [38] Krebs J., Friedrich K., Bhattacharyya D., A direct comparison of matched-die versus diaphragm forming, *Composites Part A: Applied Science and Manufacturing*, 29 (1998) 183-8.
- [39] Bersee H., Robroek L., The role of the thermoplastic matrix in forming processes of composite materials, *Composites Manufacturing*, 2 (1991) 217-22.
- [40] Zampaloni M., Abedrabbo N., Pourboghrat F., Experimental and numerical study of stamp hydroforming of sheet metals, *International journal of mechanical sciences*, 45 (2003) 1815-48.
- [41] Ramezani M., Ripin Z.M., Ahmad R., Computer aided modelling of friction in rubber-pad forming process, *Journal of Materials Processing Technology*, 209 (2009) 4925-34.
- [42] Haanappel S.P., Sachs U., ten Thije R.H., Rietman B., Akkerman R., Forming of thermoplastic composites, *Key engineering materials*, Trans Tech Publ, 2012, pp. 237-42.
- [43] Shigley J.E., *Shigley's mechanical engineering design*, Tata McGraw-Hill Education, 2011.
- [44] Martin C., Seferis J., Wilhelm M., Frictional resistance of thermoset prepreps and its influence on honeycomb composite processing, *Composites Part A: Applied Science and Manufacturing*, 27 (1996) 943-51.
- [45] Ersoy N., Potter K., Wisnom M.R., Clegg M.J., An experimental method to study the frictional processes during composites manufacturing, *Composites Part A: Applied Science and Manufacturing*, 36 (2005) 1536-44.
- [46] Gillham J.K., Formation and properties of thermosetting and high T_g polymeric materials, *Makromolekulare Chemie. Macromolecular Symposia*, Wiley Online Library, 1987, pp. 67-74.
- [47] Brinson H.F., Brinson L.C., *Polymer engineering science and viscoelasticity: an introduction*, Springer Science & Business Media, 2007.
- [48] Crossley R.J., Schubel P.J., De Focatiis D.S., Time-temperature equivalence in the tack and dynamic stiffness of polymer prepreg and its application to automated composites manufacturing, *Composites Part A: Applied Science and Manufacturing*, 52 (2013) 126-33.
- [49] Hunston D., Kinloch A., Shaw S., Wang S., Characterization of the fracture behavior of adhesive joints, *Adhesive Joints*, Springer, 1984, pp. 789-807.
- [50] Kinloch A., *Mechanics and mechanisms of fracture of thermosetting epoxy polymers*, *Epoxy Resins and Composites I*, Springer, 1985, pp. 45-67.

- [51] Sugavaneswaran M., Arumaikkannu G., Modelling for randomly oriented multi material additive manufacturing component and its fabrication, *Materials & Design*, 54 (2014) 779-85.
- [52] Sugavaneswaran M., Arumaikkannu G., Analytical and experimental investigation on elastic modulus of reinforced additive manufactured structure, *Materials & Design*, 66 (2015) 29-36.
- [53] Berman B., 3-D printing: The new industrial revolution, *Business horizons*, 55 (2012) 155-62.
- [54] Standard Test Method for Determination of Tensile Properties and Test Conditions for Moulding and Extrusion Plastics, ASTM D5937-96, American Society of Testing and Materials, Conshohocken, PA, 1998.
- [55] Standard Test Method for Tensile Properties of Plastics, ASTM D638, American Society of Testing and Materials, West Conshohocken, PA, 1997.
- [56] Standard Test Method for Tensile Properties of Polymer Matrix Composite Materials, ASTM D3039/D3039M, West Conshohocken, PA, 1976.
- [57] Plastics - determination of tensile properties - part 1, ISO 527-1, International Standards Organization.
- [58] Plastics - determination of tensile properties - part 2, ISO 527-2, International Standards Organization.
- [59] Dimas L.S., Bratzel G.H., Eylon I., Buehler M.J., Tough composites inspired by mineralized natural materials: computation, 3D printing, and testing, *Advanced Functional Materials*, 23 (2013) 4629-38.
- [60] VeroWhitePlus PolyJet Materials Details | RedEye 3D Printing Services, 2015.
- [61] Tango Materials | 3D Modeling 3D Printing Materials, Rubber-Like, 2015.
- [62] ASTM-D1876, Peel Resistance for Adhesives, T-Peel Test American Society for Testing and Materials, West Conshohocken, PA.
- [63] Karac A., Blackman B.R.K., Cooper V., Kinloch A.J., Rodriguez Sanchez S., Teo W.S., et al., Modelling the fracture behaviour of adhesively-bonded joints as a function of test rate, *Engineering Fracture Mechanics*, 78 (2011) 973-89.
- [64] Blackman B., Hadavinia H., Kinloch A., Paraschi M., Williams J., The calculation of adhesive fracture energies in mode I: revisiting the tapered double cantilever beam (TDCB) test, *Engineering Fracture Mechanics*, 70 (2003) 233-48.
- [65] Standard Terminology for Additive Manufacturing—Coordinate Systems and Test Methodologies, ISO / ASTM52921 - 13, West Conshohocken, PA, 2013.
- [66] Sharpe L.H., Some thoughts about the mechanical response of composites, *The Journal of Adhesion*, 6 (1974) 15-21.
- [67] Kinloch A.J., Young R.J., *Fracture behaviour of polymers*, North-Holland, 1983.
- [68] Argon A.S., *The physics of deformation and fracture of polymers*, Cambridge University Press, 2013.
- [69] Dillard D.A., Hinkley J.A., Johnson W.S., Clair T.L.S., Spiral Tunneling Cracks Induced by Environmental Stress Cracking in LaRC™-TPI Adhesives, *The Journal of Adhesion*, 44 (1994) 51-67.
- [70] Goehring L., Nakahara A., Dutta T., Kitsunozaki S., Tarafdar S., *Desiccation Cracks and their Patterns: Formation and Modelling in Science and Nature*, John Wiley & Sons, 2015.

- [71] Chen B., Dillard D.A., The effect of the T-stress on crack path selection in adhesively bonded joints, *International journal of adhesion and adhesives*, 21 (2001) 357-68.
- [72] Chen B., Dillard D.A., Numerical analysis of directionally unstable crack propagation in adhesively bonded joints, *International journal of solids and structures*, 38 (2001) 6907-24.
- [73] Chen B., Dillard D.A., Dillard J.G., Clark Jr R.L., Crack path selection in adhesively bonded joints: the roles of external loads and specimen geometry, *International journal of fracture*, 114 (2002) 167-90.
- [74] Chai H., A note on crack trajectory in an elastic strip bounded by rigid substrates, *International journal of fracture*, 32 (1986) 211-3.
- [75] Fleck N.A., Hutchinson J.W., Zhigang S., Crack path selection in a brittle adhesive layer, *International Journal of Solids and Structures*, 27 (1991) 1683-703.
- [76] Kinloch A., Lau C., Williams J., Modelling the fracture behaviour of adhesive joints, *The Journal of Adhesion*, 59 (1996) 217-24.
- [77] Wessel J.K., *The handbook of advanced materials: enabling new designs*, John Wiley & Sons, 2004.
- [78] Mazumdar S., *Composites manufacturing: materials, product, and process engineering*, CrC press, 2001.
- [79] Furrow A.P.C., Dillard D.A., Clair T.L.S., Hinkley J., Dye Penetrant Induced Micro cracking in High Performance Thermoplastic Polyimide Composites, *Journal of composite materials*, 32 (1998) 31-48.
- [80] Wijskamp S., *Shape distortions in composites forming*, University of Twente, 2005.
- [81] Budinski K.G., *Guide to friction, wear and erosion testing*, ASTM International, 2007.
- [82] Groves D.J., A characterization of shear flow in continuous fibre thermoplastic laminates, *Composites*, 20 (1989) 28-32.
- [83] Harrison P., Thije R., Akkerman R., Long A.C., Characterising and modelling tool-ply friction of viscous textile composites, *World Journal of Engineering*, 7 (2010) 5-22.
- [84] Lin H., Harrison P., Haar v.d.K., Long A., Akkerman R., Clifford M., Investigation of tool-ply friction of viscous textile composites, (2006).
- [85] Lima M., Vasconcelos R., Abreu M.J.A.M., Silva M.E., Comparative study of friction coefficient in nonwovens using friction, fabric friction tester, (2006).
- [86] Allaoui S., Hivet G., Wendling A., Ouagne P., Soulat D., Influence of the dry woven fabrics meso-structure on fabric/fabric contact behaviour, *Journal of Composite Materials*, (2012) 0021998311424627.
- [87] Ajayi J.O., An attachment to the constant rate of elongation tester for estimating surface irregularities of fabrics, *Textile research journal*, 64 (1994) 475-9.
- [88] Ajayi J., Elder H., Fabric friction, handle, and compression, *Journal of the Textile Institute*, 88 (1997) 232-41.
- [89] Ajayi J.O., Fabric smoothness, friction, and handle, *Textile research journal*, 62 (1992) 52-9.
- [90] Mallick P.K., *Fiber-reinforced composites: materials, manufacturing, and design*, CRC press, 2007.
- [91] *Woven Fabrics*, NetComposites, 2015.

- [92] Murtagh A.M., Lennon J.J., Mallon P.J., Surface friction effects related to pressforming of continuous fibre thermoplastic composites, *Composites Manufacturing*, 6 (1995) 169-75.
- [93] Lakrouit H., Sergot P., Creton C., Direct observation of cavitation and fibrillation in a probe tack experiment on model acrylic pressure-sensitive-adhesives, *The Journal of Adhesion*, 69 (1999) 307-59.
- [94] Vanclooster K., Lomov S.V., Verpoest I., Investigation of interply shear in composite forming, *International Journal of Material Forming*, 1 (2008) 957-60.
- [95] Wilks C., Characterization of the Tool/Ply interface during forming, Nottingham: University of Nottingham, (1999).
- [96] Clifford M., Long A., deLuca P., Forming of engineering prepregs and reinforced thermoplastics, TMS annual meeting and exhibition, second global symposium on innovations in materials, processing and manufacturing: sheet materials: composite processing, 2001.
- [97] Chow S., Frictional interaction between blank holder and fabric in stamping of woven thermoplastic composites, 2002.
- [98] Shimazaki A., Viscoelastic changes of epoxy resin–acid anhydride system during curing, *Journal of Applied Polymer Science*, 12 (1968) 2013-21.